A Molecular Beam Apparatus to Search for Time-Variation of Fundamental Constants

Boran Kuzhan

Advisor: Professor David A. Hanneke
January 29, 2021

Submitted to the
Department of Physics & Astronomy of Amherst College
in partial fulfilment of the
requirements for the degree of
Bachelors of Arts with honors

Abstract

The creation of the Standard Model (SM) brought huge amount of success with itself for Atomic, Molecular of Optical Physics (AMO). Nonetheless, there still are failures in SM to explain the nature of Dark Matter/Energy and Gravity, which led to creating theoretical extensions to SM (named "Physics Beyond the Standard Model").

Some of these theories predict changes in fundamental constants such as the proton-to-electron mass ratio μ, denoted $\frac{\dot{\mu}}{\mu}$. Diatomic molecules are sensitive to μ variation due to the motion of the nuclei, specifically due to molecular vibration and rotation. Eventually, we will drive a rovibrational transition $\mid O_2^+\ X^2\Pi_g, \nu = 0\rangle \rightarrow \mid O_2^+\ X^2\Pi_g, \nu > 0\rangle$ to look at tightening the bound on $\frac{\dot{\mu}}{\mu}$. We expect this transition frequency to vary in time if $\frac{\dot{\mu}}{\mu}$ is non-zero. However, O_2^+ does not fluoresce during these transitions. So, we will use a destructive method with a laser pulse dissociating the ions in the final state $\mid O_2^+\ X^2\Pi_g, \nu > 0\rangle$. Looking at the fraction of $\frac{O_2^+}{O^+}$ after disassociation will allow us to measure the transition frequency. A Time-of-Flight Mass Spectrometer (ToF-MS) is needed to make this measurement. A ToF-MS gives a constant kinetic energy to ions with equal charge and looks at their arrival times to differentiate their masses.

In this thesis, I first describe the theory behind rovibrational transitions in diatomic molecules. I also review the existing spectroscopy literature for our molecule to get a baseline for improvement for our transition frequency measurements. Then, I present the design and theory of a Time-of-Flight Mass Spectrometer with flight times insensitive to the initial position of the ions. This apparatus will be used in measuring the transition frequency of our clock transition with more precision than the current literature. An Ion Optics lens (Einzel lens, whose theory is also presented) is included in the design. It spatially focuses ions in the transverse direction without affecting their kinetic energy. We discuss the simulations of the expected behavior, construction techniques and construction of the apparatus. We then present data confirming that the device works as expected. We also demonstrate that the simple theory behind our ToF-MS is not enough to explain the obtained data when an Einzel lens is included in the design, as it alters the expected arrival time. The thesis ends with a road map for the experiment that incorporates our Linear Paul Trap for co-trapping O_2^+ with Be^+. Besides helping us investigate physics beyond SM, these transitions in O_2^+ also have the potential to become the next-generation high precision clocks, replacing the current atomic clocks.

Acknowledgments

First of all, I cannot express my gratitude to Prof. Hanneke enough. Without his constant guide and his endless patience listening to and correcting my nonsensical trying-to-be-physics-related ramblings, this thesis could not have been possible. Even during this time of a once-in-a-hundred-years pandemic, he constantly went out of his way to make sure that my thesis is impacted as little as possible. Furthermore, since I was doing my coursework remotely for the last semester of my thesis, he and Annika Lunstad 21' borne the majority of the work of physically assembling the apparatus and taking the data. Annika also spared time from her own thesis research and optimized the parameters for data taking. So, thank you Professor Hanneke and thank you Annika!

I am also indebted to my friends. Sai (Chauhan), thank you for listening to me every time I came to you to tell you something and ask for help, regardless of whether it was 2 am or pm. Furthermore, you had the best tea around in the Physics & Astronomy Department (which is the only reason I talk to you, honestly(!)). Also, try coffee at some point, please. Ryan (McMillan), you were the one with their feet on the ground in the Boran-Ryan-Sai triangle. This attitude of yours prevented me from collapsing during this college journey. Oh, by the way, reply to your messages for goodness' sake! Claire (Carlin), our study-sessions were some of the most productive moments in my college life. I learned more things from you than I explained to you. I appreciated your honesty, harsh (in a good way) reactions and our backgammon sessions. Additionally,

establishing a communication line with you has been the easiest among my friends in college(!)

Finally, my parents' support to me during my entire life was the reason that made me who I am today. During these stressful years, I could talk to and consult them, regardless of the time zone difference. I lost count of how many times I woke them up at 3am and talked to them for an hour about my problems at the time. I probably shortened their life span by a few years the least. My father was always the strongest person that I could rely on, while my mother was always the most compassionate one in my life. They always pushed me to expand my horizon while never leaving me alone, regardless of my physical location. Therefore, I would like to say: *Alnımızın akıyla bu işten de çıktık. Ellerinizden öperim ve size sonsuza kadar minnettârım anne ve baba.*

This thesis is based upon work supported by the Amherst College Provost and Dean of the Faculty and by the National Science Foundation under grant PHY-1806223 (RUI).

Contents

List of Figures

Chapter 1

Introduction

1.1 What is Time, and What is a Clock:

Before going into our accomplishments in the lab, we should discuss the overarching theme of this thesis: time. For most of us, it is a concept that we take for granted. However, what *exactly* is time? As one delves deeper into this question we realize that–unlike spatial dimensions–we do not have a concrete description of time. We do not even have a convincing bijection between our concept of time and the real world. Let us start trying to formulate an "answer" from the perspective of someone not interested in physics first, and then from the viewpoint of Atomic Physics.

1.1.1 In General?

For someone trying to catch their private yoga class on *time*, time is what the clock points to. Unfortunately, this is a circular argument, because when we ask "What is a clock?" the response would be "The thing that measures time." Therefore, perhaps, time is a proxy we use in daily life for *change* [1]. Suppose for a moment that we "live" in a world where **nothing** changes. For instance, let us think about a photograph. Do we *really need* to define a concept of time to explain this photograph [2]? No!

Therefore, for the general public, time is just something that allows them to keep track of changes in things. However, how do you keep track of these changes? You do that by referencing the changes in that object to changes in another object whose evolution you are familiar with [3, 4]. This is–without any coincidence–what clocks are!

This was the main task of humans when they started building clocks. One of the first familiar things that came to their mind–about 6000 years ago–was the Sun! It seemed to rise and set very regularly. Hence, they "timed" their days according to its position, which later evolved into Sundials. Then, we realized we can make water drop from some orifice at a relatively "constant" rate, which gave rise to Water Clocks. Archaeologists discovered one of its earliest examples in the tomb of Amenhotep I of Egypt [3].

Therefore, keeping track of time necessitated the existence of a regular–preferably repetitive–pattern and a way to keep track of this pattern in equal increments such as the clock-hands [3]. However, what is the concept of time for physicists, then? Surely it should be related to "change," but can we pinpoint the underlying meaning?

1.1.2 What *may* time be for Atomic Physics and Why do We Measure It?

Perhaps one of the most promising candidates for time in the domain of physics is **entropy**, because we know that the entropy of the Universe always increases. Therefore, time may just be the direction in the Universe where the entropy is monotone increasing [2, 5]. So, inadvertently, we might have done a simplification or have been subject to the illusion of our own minds [2, 5]. For instance, Loop Quantum Gravity tries to explain this phenomena. One of its proponents Dr. Carlo Rovelli says that

certain equations of quantum gravity like Wheeler-DeWitt equation can be written without using any variable dependent on *time*. Therefore, perhaps, time arises out of our inability to see the Universe in its entirety [2, 5].

In the end, regardless of its true nature, time is a useful concept in physics and engineering. For instance, the Synchrophasor measurements for the power systems we have require a timing precision of 1 μs or more (IEEE C37.118-2011 *Standard for Synchrophasor Measurements for Power Systems*) [6]. Furthermore, GPS satellites have very accurate clocks on-board for the system to function correctly [4, 7, 8]. The system has to correct for the relativistic time dilation that the high-speed of satellites causes relative to someone on Earth walking, along with correcting for the gravitational blue-shift [4, 7, 8]. If this correction is not made, the time you see on your phone would be off after a few minutes and the error in position would increase at a rate about 10 $\frac{\text{km}}{\text{day}}$) [4, 8]. Hence, it is clear that we would like to get as much precision as we can get for civilian (and military in the case of the GPS, which is its initial *raison d'être* [7]) applications.

Currently, the most precise clocks are Atomic Clocks. As the name suggests, they use atoms as a clock. The vibrational level spacing $\hbar\omega$ indicates an intrinsic oscillation frequency (i.e. dependent on the ω). Therefore, these oscillations can be used in a clock if a method to count the number of oscillations can be found [4, 9]. The existence of precise clocks is also useful in fundamental physics. For example, it allows us to test fundamental laws and look for physics beyond the Standard Model. Certain extensions to the Standard Model and General Relativity–mostly higher-dimensional theories like String Theories, Loop Quantum Gravity, Discrete Quantum Gravity–predict variation of Fundamental Constants [4, 5, 10]. So, detecting a variation in these constants can give us clues about the origin of Dark Energy. Two of the most relevant Fundamental Constants for AMO–that are subject to variation–are the fine-

structure constant α and proton-to-electron mass ratio $\mu = \frac{m_p}{m_e}$ [4, 10]. Looking at the change of these constants generally requires finding a transition in an atom or a molecule whose frequency depends on the constant. Then, you measure the frequency of this transition for a long-time to see how much this frequency changes [4, 10–13]. This is exactly one of the reasons why Atomic Physics needs extremely precise clocks. They allow us to measure these changes more precisely, and these changes allow us to investigate the validity of certain extensions of the Standard Model [4, 10].

In the Hanneke lab, we are trying to measure–or at least tighten the bounds on–the change in μ, denoted $\frac{\dot{\mu}}{\mu}$. To do this we are going to measure the frequency of transition between two quantum states say $|\beta\rangle$ and $|\theta\rangle$ in the $X^2\Pi_g$ state of O_2^+ to see if the frequency of this transition changes over a long period of time. If it does, then we have a change in μ since the frequency of vibration depends on nuclear and electron masses [4, 11–13]. We should now detail *how* we are going to do the measurement.

1.2 Measurement Method and Process

Our clock transition is $|O_2^+\ X^2\Pi_g, \nu = 0\rangle \rightarrow |O_2^+\ X^2\Pi_g, \nu = \gamma\rangle$, where γ is any integer greater than 0. Specifically, our first measurement will use $\gamma = 16$ due to the convenience of the wavelength [4, 11, 12, 14]. To obtain our desired initial state $|O_2^+\ X^2\Pi_g, \nu = 0\rangle$, we will cool our oxygen neutral molecule with free-jet expansion into our vacuum chamber. Next, the gas beam will get ionized by our UV-laser. After obtaining the right initial state, we will drive a transition to obtain our final state $|O_2^+\ X^2\Pi_g, \nu = 16\rangle$ of O_2^+. Our initial goal will be to measure the wavelength of this transition with more precision compared to current literature [4, 12, 14]. After this, we are planning to increase the precision of other transitions within the $X^2\Pi_g$ state of O_2^+ (Current best known values can be found in Appendix C). Since there is no fluorescence in these transitions, we will use a destructive method [11, 12]. We

will fire another laser pulse to disassociate the molecules in the correct final state (i.e. $|O_2^+\ X^2\Pi_g, \nu = 16\rangle$). Then, by looking at the proportion of O^+ to O_2^+, we will construct the graph of the transition [11, 12, 14, 15].

To achieve these goals, we had to first grasp the theory behind these molecular transitions in the context of diatomic molecules (Chapter 2). Then, we learned the theory behind and built our apparatus, which is a specific type of a Time-of-Flight Mass Spectrometer (ToF-MS) [16] (Chapter 3). A ToF-MS accelerates charged particles through the same electric field. This gives them the same kinetic energy if they have the same charge. Then, these charged particles fly through a tube with no electric field [16]. Depending on these particles' masses, they will have different speeds. Thus, their arrival times to the end of the tube depend on their masses. Using these arrival times, we will differentiate ions with different masses (i.e. O^+ and O_2^+) [16]. The electrode configuration of our apparatus is designed to mitigate some of the leading systematic effects in determining the mass of the detected ions [16]. Subsequently, we had to assemble our apparatus in the lab (Chapter 4). After the successful construction of our apparatus, we took data on whether our instrument works as expected (Chapter 5). Having demonstrated the successful operation of the detection system, we concluded with recommended next steps towards the goal of measuring $\frac{\dot{\mu}}{\mu}$ (Chapter 6).

Chapter 2

Spectroscopic Calculations and Review of Prior Experiments

Since the focus of this thesis is to set the path to the precision measurement of two-photon transitions in the $X^2\Pi_g$ state of O_2^+ and to lay the path for our goal of driving the transition $|O_2^+\ X^2\Pi_g, v = 0\rangle \rightarrow |O_2^+\ X^2\Pi_g, v = 16\rangle$ [11, 12], we should first talk about the theory about rovibrational and electronic transitions in homonuclear diatomic molecules. After that, we should look at the most precise existing spectroscopic data for the $X^2\Pi_g$ state of O_2^+ to know our baseline for improvement.

The final theory involves finding eigenvalues/vectors of the Hamiltonian, which we did using the software PGOPHER. It is a computer program for calculating molecular rovibrational-electronic spectra [17–20]. It requires constants for rotational,vibrational and electronic states, then calculates the transition energies. These constants are embedded in the Hamiltonian. To understand these constants, we will start with approximations of the Hamiltonian before presenting it fully [17, 19]. *All of the discussion in this chapter follows from* [13, 21]. *Additional sources used will be cited explicitly.* In [21], the most relevant chapter is Chapter 9, and the most relevant chapters in [13] are Chapters 3, 4, 5.

2.1 Theory of Rovibrational Transitions

Note: In all of the discussion below explaining the theory, we discuss transitions within the same potential (i.e. the same electronic state).

2.1.1 Approximation of the Full Hamiltonian

We will proceed towards the full Hamiltonian with a series of approximations, each giving us a better approximation than the last one. These approximations will allow us to understand the constants used in PGOPHER's calculations. We will start with the rigid rotor and harmonic oscillator approximations. Then, we will introduce centrifugal distortion and anharmonicity. Finally, we will have the spin-orbit coupling and Coriolis effect corrections. After the explanation of the full Hamiltonian, we discuss some of the specificities of our molecule, $X^2\Pi_g$ state of O_2^+ (such as the absence of hyperfine-structure) [4, 11, 12].

Rigid Rotator

The simplest approximation is to think of O_2^+ as two point particles connected with a massless rigid-rod. Remember that classically, the energy of a rigid rotator is given by $E = \frac{1}{2}I\omega^2$. Now, using the classical total angular momentum formula of $P = I\omega$, we can write the total energy as:

$$E = \frac{P^2}{2I}. \tag{2.1}$$

Here, we follow the notation of ref. [13, 21], which differs from typical undergraduate quantum mechanics notation where P is reserved for linear momentum. It can be shown that the moment of inertia is given by:

$$I = \frac{m_1 m_2}{m_1 + m_2} r^2, \tag{2.2}$$

where m_1, m_2 are the two masses and r is the internuclear distance. This implies that the motion can be reduced to the motion of a rotating particle of mass μ, r away from a fixed origin of rotation with:

$$\mu = \frac{m_1 m_2}{m_1 + m_2}, \tag{2.3}$$

which is called the *reduced mass*.

Energy Levels: Therefore, we have to solve the Schrödinger Equation with $m = \mu$ and $V = 0$ to find the energy levels. So, we have:

$$\frac{-\hbar^2}{2\mu}\nabla^2\psi = E\psi, \tag{2.4}$$

with $x^2 + y^2 + z^2 = r^2$ being constant due to the rigid rotator approximation. The solution is:

$$E = \frac{h^2 J(J+1)}{8\pi^2 \mu r^2} = \frac{h^2 J(J+1)}{8\pi^2 I} = BhcJ(J+1), \tag{2.5}$$

where J is an integer with $J \geq 0$ and $B = \frac{h}{8\pi^2 Ic}$.

Harmonic Oscillator

The chemical bond between the atoms is not actually rigid. So, we may also assume that the molecule is a harmonic oscillator. Then, the displacement from the equilibrium position behaves like a harmonic oscillator to a first approximation. We can still reduce this motion to the simple harmonic motion of a single point mass. Remember that in classical harmonic oscillator, we have the vibrational frequency:

$$f_{osc} = \frac{1}{2\pi}\sqrt{\frac{k}{m}}, \tag{2.6}$$

where k is the *force constant*. So, in terms of potential energy, we have:

$$V = \frac{1}{2}kx^2 = 2\pi^2 m {f_{osc}}^2 x^2. \tag{2.7}$$

If we approximate that the forces each atom feels are proportional to the internuclear distance (with atoms having m_1 and m_2), we have the potential energy: [22, 23]

$$V = 2\pi^2 \mu f_{\text{osc}}^2 (r - r_e)^2, \tag{2.8}$$

where r_e is the equilibrium distance between the two atoms and r is the inter-atomic distance (Notice that for the rigid-rotor discussion, we explicitly used r and not r_e to keep it more general. In the case where the atoms are r_e apart, we will simply have $r = r_e$.) Solving the Schrödinger equation, we can see that the vibrational frequency is given by:

$$f_{osc} = \frac{1}{2\pi}\sqrt{\frac{k}{\mu}}. \tag{2.9}$$

Energy Levels: Now, if the potential energy is indeed given by $V = \frac{1}{2}kx^2$, then using the Schrödinger equation we get:

$$\frac{d^2\psi}{dx^2} + \frac{8\pi^2\mu}{h^2}(E - \frac{1}{2}kx^2)\psi = 0. \tag{2.10}$$

The solution to this equation is:

$$E(\nu) = \frac{h}{2\pi}\sqrt{\frac{k}{\mu}}(\nu + \frac{1}{2}) = hf_{osc}(\nu + \frac{1}{2}), \tag{2.11}$$

where we defined a new *vibrational quantum number* ν, an integer with $\nu \geq 0$. As one can tell easily, the energy levels are equidistant. $E(0) = \frac{1}{2}hf_{osc}$ is called the *zero-point*

energy. We can define –what is called term values–G like so:

$$G(\nu) = \frac{E(\nu)}{hc} = \frac{f_{osc}}{c}(\nu + \frac{1}{2}). \tag{2.12}$$

Generally, we have the following convention:

$$\omega = \frac{f_{osc}}{c}. \tag{2.13}$$

Therefore, we have $G(\nu) = \omega(\nu + \frac{1}{2})$. Note that ω is measured in cm^{-1}.

Anharmonic Oscillator

We know that the molecular oxygen is not exactly a harmonic oscillator, since the atoms are no longer in a covalent bond with r^2 distance dependence after a far enough separation [4, 22]. Rather, the potential curve of the molecular oxygen approximates a harmonic oscillator near the equilibrium point. As a first correction, we can add a cubic correction term to the potential to have:

$$U = f(r - r_e)^2 - g(r - r_e)^3, \tag{2.14}$$

where $g(r - r_e) << f$ for r near r_e. We need to add higher power correction terms for better approximations.

Energy Levels: If we substitute our new approximation for the potential energy to the wave equation with $g(r - r_e) << f$ it can be shown–for instance, via time-independent perturbation theory [22, 24]–that the energy levels of the anharmonic oscillator are given by:

$$E_\nu = hc\,\omega_e(\nu + 0.5) - hc\,\omega_e x_e(\nu + \frac{1}{2})^2 + hc\,\omega_e y_e(\nu + \frac{1}{2})^3 + \dots\ , \tag{2.15}$$

with term values: [13, 21]

$$G(\nu) = \omega_e(\nu + \frac{1}{2}) - \omega_e x_e(\nu + \frac{1}{2})^2 + \omega_e y_e(\nu + \frac{1}{2})^3 + \dots \ , \tag{2.16}$$

where $\omega_e x_e << \omega_e$ and $\omega_e y_e << \omega_e x_e$. Note that $\omega_e x_e$ and $\omega_e y_e$ **are symbols** and **not products of** ω_e with x_e and y_e, respectively. Since deviations from the harmonic oscillator tend to bring the levels closer together, there is a convention where g and $\omega_e x_e$ are always positive [4, 13, 21]. The others can be either positive or negative. Again, the zero-point energy is given by: [13, 21]

$$G(0) = \frac{1}{2}\omega_e - \frac{1}{4}\omega_e x_e + \frac{1}{8}\omega_e y_e + \dots \tag{2.17}$$

We can also reference the energy levels to the zero-point energy, in which case we have: [13, 21]

$$G_0(\nu) = \omega_0 \nu - \omega_0 x_0 \nu^2 + \omega_0 y_0 \nu^3 + \dots \ , \tag{2.18}$$

with: [13, 21]

$$\omega_0 = \omega_e - \omega_e x_e + \frac{3}{4}\omega_e y_e + \dots \ , \ \omega_0 x_0 = \omega_e x_e - \frac{3}{2}\omega_e y_e + \dots \omega_0 y_0 = \omega_e y_e + \dots \tag{2.19}$$

Dissociation: We do not have infinitely many vibrational levels in an anharmonic oscillator. After a certain number of vibrational levels, we simply disassociate our oxygen molecule. This point-of-no-return is called the *heat of dissociation* or *disassociation energy*–designated D_0–is given by:

$$D_0 = \sum_{\nu} \Delta G_{\nu+0.5}, \tag{2.20}$$

where we have $\Delta G_{\nu+0.5} = G_{\nu+\frac{3}{2}} - G_{\nu+\frac{1}{2}}$ with ν an integer with $\nu \geq 0$. The energy difference D_e between the potential minimum and the disassociation asymptote is a

bit more:

$$D_e = D_0 + G(0) = D_0 + \frac{1}{2}\omega_e - \frac{1}{4}\omega_e x_e + \frac{1}{8}\omega_e y_e + \dots \tag{2.21}$$

Hence, D_e corresponds to the maxima of $G(\nu)$ (i.e. $D_e = G_{max}(\nu)$). The corresponding vibrational quantum number is given by:

$$\nu_D = \frac{\omega_0}{2\omega_0 x_0}, \tag{2.22}$$

when ΔG is a linear function of ν. Notice that this is an estimate of how many vibrational levels there are. We do not necessarily have a bound state exactly at the asymptote of the potential.

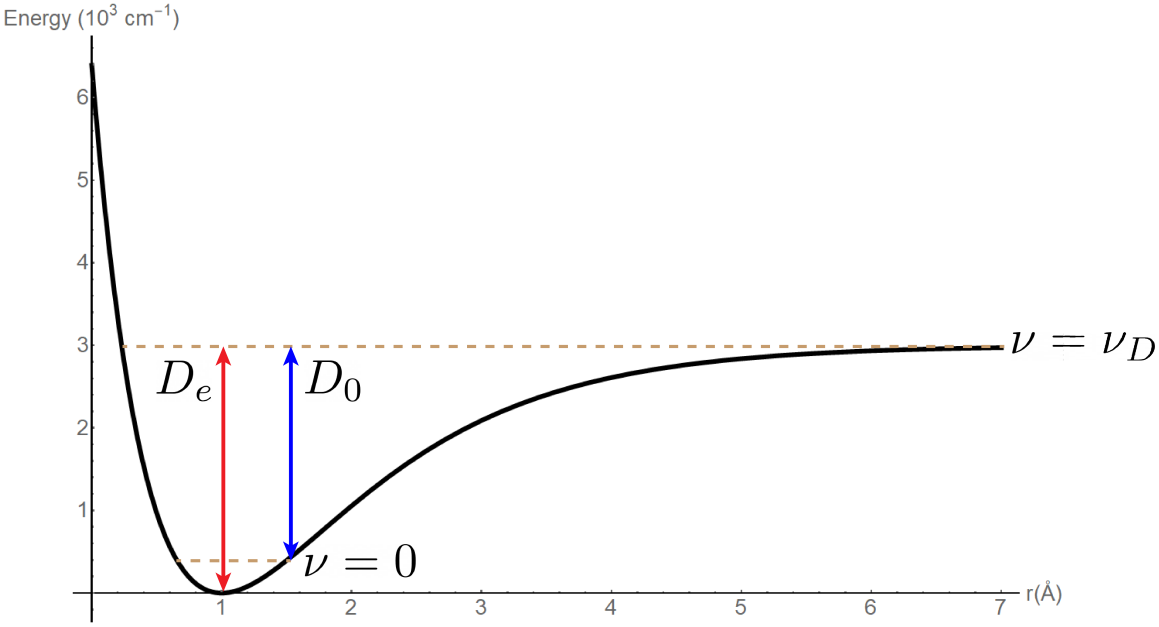

Figure 2.1: Schematic of the *disassociation energy* D_0 and the energy difference D_e between the zero point energy and the disassociation asymptote in a given electronic state for a fictional molecule.

Nonrigid Rotator

After the rigid rotator approximation, let us consider a non-rigid rotator (i.e. the distance between the two atoms may change during revolution). In other words, the two atoms are connected by a massless spring and not by a massless rigid rod.

Detailed evaluations indicate that the terms values are approximated (very well) by:

$$F(J) = \frac{E_r}{hc} = B[1 - uJ(J+1)]J(J+1), \tag{2.23}$$

where B is the same as the case of the rigid rotator with $u << 1$. This equation is often written as $F(J) = BJ(J+1) - DJ^2(J+1)^2$ with $D > 0$. The constant D is related to the vibrational term value ω by:

$$D = \frac{4B^3}{\omega^2}, \tag{2.24}$$

assuming that the vibrations are simple harmonic motion. Since $\omega >> B$, we have $D << B$.

Vibrating Rotator

The nonrigid rotator approximation does not explain the observation of relatively small deviations from its predictions, observed in rotation bands. In this approximation, the nonrigid rotator rotates and vibrates at the same time.

Energy Levels: If there were to be no interaction between the rotation and vibration of the molecule, the total energy would be the sum of the energies of rotation and vibration. However, the internuclear distance changes during vibration, changing the moment of inertia (and thus the constant B). Remember that the molecule completes one vibration much faster than one complete rotation. Also, notice that the mean radius increases with increasing vibrational level, due to the outwards skew of the potential [4, 13, 21]. So, we can use a mean B in our calculations, given by: $B_\nu = \frac{h}{8\pi^2 c\mu}[\frac{1}{r^2}]$. To a first approximation, this constant is $B_\nu = B_e - \alpha_e(\nu + \frac{1}{2})+...$ where B_e is the rotational constant corresponding to the equilibrium separation r_e. As usual, we have $\alpha_e << B_e$. Similarly, we will use a mean D (called D_ν) given by:

$D_\nu = D_e + \beta_e(\nu + \frac{1}{2}) + \ldots$, with again $\beta_e << D_e$. Therefore, the rotational term value for a vibrational level is $F_\nu(J) = B_\nu J(J+1) - D_\nu J^2(J+1)^2 + \ldots$, with $D_\nu << B_\nu$.

Symmetric Top

So far, we neglected the effect of the electrons of our molecule. These electrons make the axial moment of inertia of the molecule more than 0 (though still very small) contrary to our previous implicit assumption. A body is called a symmetric top if two of its moments of inertia with respect to its 3 principal axes are the same. As an approximation, we consider the nuclei surrounded by a rigid electron cloud, which makes it a symmetric top. This is because the moments of inertia through the 2 axes perpendicular to the internuclear axis–passing through the center of gravity–are the same.

Angular Momenta: To find the total angular momentum of a symmetric top, called **P**, we add the angular momentum that is parallel to the internuclear axis with the nonparallel angular momentum. If we neglect the electron spin, the internuclear axis component of the electronic angular momentum has to be an integer multiple of $\frac{h}{2\pi}$. If we call this integer multiple Λ, we have:

$$\mid \Lambda \mid = \Lambda \frac{h}{2\pi}, \tag{2.25}$$

with lambda being the quantum number for the internuclear axis component of the electronic angular momentum. Remember that the total angular momentum is designated **J**. Therefore, we have:

$$J \geq \Lambda, \tag{2.26}$$

So, we can have:

$$J = \Lambda, \Lambda + 1, \Lambda + 2, \Lambda + 3, \ \ldots \tag{2.27}$$

Finally, the angular momenta perpendicular to the internuclear axis is called $\mathbf{N}$, and it is completely determined by $\mathbf{\Lambda}, \mathbf{J}$.

Energy Levels: Solving the wave equation for the symmetric top, we obtain:

$$F(J) = BJ(J+1) + (A-B)\Lambda^2, \tag{2.28}$$

where we have:

$$B = \frac{h}{8\pi^2 c I_B}. \tag{2.29}$$

I_B is the moment of inertia of our homonuclear molecule with respect to any axis that is perpendicular to the internuclear axis. For a given electronic state, there is a constant offset due to electronic angular momentum–denoted with the constant A–which will cancel in our transition energy calculations. We have to have a warning here! In the following sections, we will have a constant A_ν. This A and A_ν are **NOT** the same! This is confusing, yet standard notation...

Also, we clearly do not have any levels where $J < \Lambda$. For the nonrigid symmetric top, we just add $-DJ^2(J+1)^2$ to the term value formula. Finally for the vibrating rotator, we replace B and D with B_ν, D_ν to have:

$$F_\nu(J) = B_\nu J(J+1) + (A - B_\nu)\Lambda^2 - D_\nu J^2(J+1)^2 + \quad \ldots \tag{2.30}$$

Fine-Structure and Spin-Orbit Coupling

To have even better approximations, we have to correct for relativistic effects. There are two types of relativistic corrections under the umbrella term of Fine-Structure Effects: Relativistic Kinetic Energy correction and Spin-Orbit Coupling.

The Kinetic Energy correction arises due to the fact that the kinetic energy of an electron is not really $\frac{p^2}{2m}$ but:

$$T = \sqrt{c^2p^2 + m^2c^4} - mc^2 = \frac{p^2}{2m} - \frac{p^4}{8m^3c^2} + O(p^6 \text{ or } v^6), \tag{2.31}$$

where p is electron's momentum, m is its mass, and $O(p^6$ or $v^6)$ is a higher order correction term(s) [22]. Generally, we treat this addition to the Hamiltonian as a perturbation and then solve it using Time-Independent Perturbation Theory [22]. Notice that there is no mention to electron's spin in this analysis. Therefore–remember that we have spin-$\frac{1}{2}$ in our case–this correction does not change whether our ion has $s = \frac{1}{2}$ or $s = -\frac{1}{2}$ [22]. However, this is the entire scenario if there is only one electron, and we have a lot more. So, this correction happens for each electron, and it gets complicated even further with all the Couloumb interactions we have to take into account for [4].

The Spin-Orbit Coupling effect arises due to the motion of electrons. In the rest frame of an electron, the nuclei's movements create a magnetic field $\mathbf{B}$. So, there is an interaction between electron's magnetic moment and the magnetic field $\mathbf{B}$ [22]. This gives us a perturbative Hamiltonian given by [22]:

$$\mathcal{H}_{\text{s.o}} = A_\nu \left(\mathbf{S} \cdot \mathbf{L}\right). \tag{2.32}$$

The Hamiltonian's dependence on the spin creates $2S + 1$ fine-structure states for a particle with spin S. For instance, two fine-structure states exist with $s = \frac{1}{2}$ and $s = -\frac{1}{2}$ for a spin-$\frac{1}{2}$ electron [22]. The strength of this coupling is encapsulated with the constant A_ν–called the *Spin-Orbit Coupling Constant*–and depends on which Hund's case our system belongs to (Hund's case-a for us.) For our molecule, the spin-$\frac{1}{2}$ combines with the orbital angular momentum to make a doublet with $\Omega = \frac{1}{2}$ and $\frac{3}{2}$

[4, 11–13, 21, 22].

2.1.2 Transition Rules

Now that we know the basic theory, we should look at the transition rules. Here, we follow the same successive approximation steps and discuss the applicable transition rules at each step, for Infrared and Raman/Two-Photon Transitions.

Infrared Transitions

Rigid Rotator: We have two different types of transitions: 1-photon (Infrared) transition and 2-photon transitions. For 1-photon ones, if we have a transition from an upper state with J' and lower state with J'', the transition wavenumber is given by:

$$w = \frac{E'}{hc} - \frac{E''}{hc}. \tag{2.33}$$

We can define $\frac{E}{hc} = F(J)$ called the rotational term (in cm^{-1}). So, we have:

$$F(J) = \frac{E}{hc} = \frac{h}{8\pi^2 cI} J(J+1) = BJ(J+1), \tag{2.34}$$

with the constant B–called the *rotational constant*–given by:

$$B = \frac{h}{8\pi^2 cI}. \tag{2.35}$$

Putting this all together, we can see that the wavenumber is given by: $w = F(J') - F(J'')$. However. there are some selection rules to be considered. For a rigid rotator, it can be shown that an infrared transition happens if and only if:

$$J' = J'' \pm 1, \tag{2.36}$$

(i.e. $\Delta J = \pm 1$) which is the contribution limit of a single photon [12]. Notice that the spectrum is made up of equidistant lines, since we have:

$$w = F(J'' + 1) - F(J'') = 2B(J'' + 1). \tag{2.37}$$

There is no need to discuss the $J'' - 1$ case since we can just rename $J''' = J'' - 1$ to bring us to the same situation.

Harmonic Oscillator: According to quantum theory, the wavenumber of a transition is given by: $\nu = \frac{E(\nu')}{hc} - \frac{E(\nu'')}{hc} = G(\nu') - G(\nu'')$ (Units in cm^{-1}). The corresponding selection rule can be shown to be:

$$\Delta\nu = \nu' - \nu'' = \pm 1. \tag{2.38}$$

Notice that, no matter what the upper level is, we have $G(\nu + 1) - G(\nu) = \omega$. For homonuclear molecules (in this approximation) no infrared transition between vibrational levels occurs since their dipole moment is 0.

Anharmonic Oscillator: In this case, the selection rule $\Delta\nu = \pm 1$ still gives the strongest transitions. However, it can also be shown that we also have transitions with $\Delta\nu = \pm 2, \pm 3, \ldots$ However, the intensity of transitions decreases rapidly with increasing $\mid \Delta\nu \mid$.

Non-Rigid Rotator: The selection rule for the 1-photon transitions is the same as the rigid rotator (i.e. $\Delta J = \pm 1$). Therefore, using the term values we can obtain the wavelengths:

$$\nu = F(J + 1) - F(J) = 2B(J + 1) - 4D(J + 1)^3, \tag{2.39}$$

showing us that the lines are not equidistant compared to the rigid rotator.

Vibrating Rotator: For 1-Photon transitions the same selection rules as the individual rotator/vibrator applies. So, ν can change by any integer with $\Delta\nu = \pm 1$ giving the most intense transitions. As for J we have the selection rule $\Delta J = \pm 1$.

Symmetric Top: If we neglect electronic transitions (i.e. Λ does not change between the initial and final states), for 1-photon transitions we have the selection rules:

$$\Delta J = \pm 1 \text{ for } \Lambda = 0, \tag{2.40}$$

$$\Delta J = 0, \pm 1 \text{ for } \Lambda \neq 0. \tag{2.41}$$

Raman/Two-Photon Transitions

Up until now, we considered 1-photon transitions. That is to say that either a spontaneous emission or absorption of a photon causing a transition. We now treat Two-Photon transitions, a special case of which is called a Raman transition. If we add one photon and subtract one, that is called a Raman transition. If, instead, we add two photons–or subtract two photons–that is called a Two-Photon transition. So, Raman transitions are a subset of Two-Photon transitions [4]. Here, we will give the analysis for Raman transitions for simplicity. However, the analysis is very similar–if not the same–for two-photon transitions with mostly sign changes due to the fact that we *add* two photons instead of one addition and one subtraction [4].

We have an incident light with energy hf' hitting a molecule. There will be 2 cases: elastic scattering and inelastic scattering. In elastic scattering, the frequency of light remains unchanged. In the inelastic case, it either gives energy to or takes energy from the molecule. This energy difference should be equal to the energy difference

between 2 states of the molecule:

$$\Delta E = E' - E''. \tag{2.42}$$

Depending on whether the light quantum absorbs or gives energy to the molecule, its energy after the collision will be:

$$hf' \pm \Delta E. \tag{2.43}$$

Hence, the frequency of the light after collision is: $f' \pm \frac{\Delta E}{h}$. Remember that Raman/Two-Photon transition is NOT fluorescence. In fluorescence, the incident light is completely absorbed and the molecule can decay to several other states after the mean life [4]. The other main difference is that the Raman/Two-Photon transition can happen at all frequencies of light whilst fluorescence can happen at certain frequencies only.

Rigid Rotator Raman/Two-Photon Spectrum: For the rotational Raman/Two-Photon Spectrum, it can be shown that the selection rule is: $\Delta J = 0, \pm 2$. Again, $\Delta J = 0$ is the undisplaced line. Since for the frequency shift calculation ± 2 would give the same result, we only consider $\Delta J = +2$. So, the frequency shift would be: $\mid \Delta\nu \mid = F(J+2) - F(J) = B(J+2)(J+3) - BJ(J+1) = 4BJ + 6B = 4B(J + \frac{3}{2})$. Hence, we have equidistant lines again.

Harmonic Oscillator: An analysis of the polarizability's matrix elements can show that the selection rule for the Raman/Two-Photon transition for a harmonic oscillator is:

$$\Delta\nu = \pm 1. \tag{2.44}$$

Hence, the lines are shifted by $\mid \Delta\nu \mid = G(\nu+1) - G(\nu) = \omega$ to both sides of the original line. Notice that Raman/Two-Photon spectrum depends only on polarizability. Therefore, even in the case of no permanent dipole moment, we can still have a Raman/Two-Photon spectrum.

Anharmonic Oscillator: The strongest transitions for the Raman/Two-Photon Spectrum in the anharmonic oscillator approximation is still for $\Delta\nu = \pm 1$. However, $\Delta\nu = \pm 2, \pm 3, \pm 4, \ldots$ are allowed with decreasing intensity as $\mid \Delta\nu \mid$ increases.

Non-Rigid Rotator: In terms of the Raman/Two-Photon spectrum, a non-rigid rotator still has the same selection rules (i.e. $\Delta J = \pm 0, 2$). Therefore, we have:

$$\mid \Delta\nu \mid = F(J+2) - J(J) = (4B - 6D)(J + \frac{3}{2}) - 8D(J + \frac{3}{2})^3. \tag{2.45}$$

Notice that the rotational constant D indicates the influence of the centrifugal force.

Vibrating Rotator: Vibrating Rotator's Raman/Two-Photon Spectra selection rules are the same as that of the anharmonic oscillator and rotator. Therefore, $\Delta\nu$ can take any integral value with $\Delta\nu = \pm 1$ giving the most intense transitions. For J, we have $\Delta J = 0, \pm 2$.

Symmetric Top: As for the Raman/Two-Photon transitions for a symmetric top, we have the selection rules:

$$\Delta J = 0, \pm 2 \text{ for } \Lambda = 0, \tag{2.46}$$

$$\Delta J = 0, \pm 1, \pm 2 \text{ for } \Lambda \neq 0. \tag{2.47}$$

2.1.3 Symmetry Properties and The Absence of Asymmetric Wave Functions

When a molecular system is subject to an inversion through the origin, depending on the system, the eigenfunctions either change sign or not. We have two linearly independent eigenfunctions for each rotational level in a symmetric top with $\Lambda \neq 0$. We can always choose these functions such that one of them does not change after an inversion and the other does. In another words, we can choose these functions with different parity. For a diatomic molecule, the rotational levels are classified depending on the total eigenfunction's response to an inversion. It is called *positive* if the total eigenfunction does not change and *negative* if the total eigenfunction changes sign with respect to an inversion through the origin. The total eigenfunction is the product of electronic, vibrational and rotational eigenfunctions to a first approximation:

$$\psi = \psi_e \frac{1}{r} \psi_\nu \psi_r. \tag{2.48}$$

The vibrational part $\frac{1}{r}\psi_\nu$ does not change with inversions since it only depends on the internuclear distance. For a symmetric top with $\Lambda \neq 0$, we have one positive and one negative rotational level for each J. Since our experiment involves Raman/Two-Photon transitions, **we can only have transitions between states with the same sign** (i.e. $+ \rightarrow +$ and $- \rightarrow -$).

Homonuclear Molecules

Wavefunctions of homonuclear molecules are even. Such systems are called to be *gerade* (g for short). Systems are called *ungerade* (u for short) if their wavefunctions are odd, with respect to the exchange of their two nuclei. For rovibrational states within an electronic state, all positive levels have the same symmetry that is the opposite of the negative levels (i.e. all positive levels are gerade whilst all negative

levels ungerade or vice versa). Since our nuclei have zero nuclear spin, it can be shown that *transitions between gerade and ungerade states are forbidden.* **We only have gerade wavefunctions** for the $X^2\Pi_g$ state of O_2^+. **Therefore, our analysis looks only at transitions between gerade wavefunctions** [11, 23].

2.1.4 The Full Hamiltonian

These were the relevant approximations that would allow the reader to understand the meaning of the constants used in the calculations done by PGOPHER [17]. The full Hamiltonian incorporating and completing these approximations is the following: [23]

$$\mathcal{H} = \mathcal{H}_{electronic} + \frac{1}{2\mu}\mathbf{P}_R{}^2 + hcB(R)(\mathbf{N}-\mathbf{L})^2 + \frac{1}{2M}\mathbf{P}^2 + \mathcal{H}_{so}{}^{(e)} + \mathcal{H}_{so}{}^{(n)} + \mathcal{H}_{ss}{}^{(scal)} + \mathcal{H}_{ss}{}^{(tens)} + \mathcal{H}_{hfs}. \quad (2.49)$$

First component of the Hamiltonian is the electronic Hamiltonian with Coulomb and electonic-kinetic energies. The following two terms are vibrational and rotational kinetic energies, respectively. The fourth term is the Hamiltonian for the mass polarization correction including the total linear momentum of electrons [23]. Mass polarization is caused due to a shift of the center of mass from the midpoint between the two nuclei, which is caused by the finite mass of the nuclei and electrons [25–27].

The following two terms $\mathcal{H}_{so}^{(e)}$ and $\mathcal{H}_{so}^{(n)}$ are portions of electronic spin-orbit and spin-other-orbit terms involving the electronic and nuclear momenta, respectively. The next two terms are for the electron spin-spin interaction's scalar and tensor parts. Finally, the last term describes the hyperfine effects of the nucleus, including the electric and magnetic interactions such as electric monopole/quadrupole like isomer shift [23, 28].

2.1.5 Specificities of $X^2\Pi_g$ state of O_2^+

Apart from the general theory for all diatomic molecules, there are certain features of our system that we should specify. First of all, the nuclei of the oxygen molecular ion are spin zero. Therefore, it does not have any hyperfine structure. So, we have: [4, 11, 23]

$$\mathcal{H}_{hfs} = 0 \tag{2.50}$$

Our state of interest is $X^2\Pi_g$ of O_2^+, where X means that we are in the electronic ground state and Π_g means we are in a gerade state with $\mid \Lambda \mid = 1$. Furthermore, the 2 is the result of $2S + 1$, hence $S = \frac{1}{2}$. So, there are two fine-structure states associated with the sign of the spin (i.e. $\pm\frac{1}{2}$) [13, 21–23]. Our molecule obeys Hund's case (a) which means that **S** and **L** are coupled via the spin-orbit coupling and **L** is coupled to the internuclear axis. In this case, the good/useful quantum numbers are Ω and J where we have $\Omega = \Lambda + \Sigma$. Here, Λ is the internuclear projection of the total electronic orbital momentum, and Σ is the internuclear projection of the electronic spin [11, 22, 23].

In our case, for each given J, a state can have two different values of omega, namely: [4, 11, 13, 21–23]

$$\text{For a given } J, \text{ we have } \Omega = \frac{1}{2} \text{ or } \frac{3}{2}, \tag{2.51}$$

whose only exception is $J = \frac{1}{2}$, where we only have $\Omega = \frac{1}{2}$.

The two fine-structure states for each J form the basis states for our Hamiltonian. So, we can write the Hamiltonian as a 2×2 matrix and find the eigenvalues/vectors to find the eigenstates. Since our system obeys Hund's case (a), our matrix is more or less diagonal–but not entirely–especially for higher J. We will then multiply this matrix with the ket and then multiply the result with the bra to get the complex

amplitude [11, 17, 19, 22, 23].

Fine Structure: Fine structure corrections to the energy levels arise due to relativistic corrections to the non-relativistic Hamiltonian. Since our system is in Hund's case (a). The biggest correction is the spin-orbit coupling (200 cm^{-1}), whose related constant–used in calculations–is A_ν [11, 22, 23].

Λ **Doubling:** Remember that we are in a Π state, which means that $\mid \Lambda \mid = 1$. Therefore, we have 2 possible states within the same energy level: $\Lambda = 1$ and $\Lambda = -1$, which differentiates the two different orientations of the internuclear axis projection of the orbital angular momentum. It can be shown that this is approximate. The states actually split and have different energies. Furthermore, we only have symmetric wavefunctions. So, we only have one state per energy level. Therefore, Λ-doubling shows up as a vertical shift in the energy of the state [11, 22, 23].

2.2 Constants and Their Choice for Current Best Spectroscopic Estimates

Here we present a quick review/table of all the relevant molecular constants in the Full Hamiltonian used in our PGOPHER calculations, along with where we obtained these constants and our rationale for choosing these constants [23].

2.2.1 Constants Used and Their Explanations

Uncertainties

We need to estimate the uncertainties in transition wavelengths after calculating them. A look at the reported values and constants [29–31] reveals that to a first approximation (2 significant digits) the uncertainty in the transition wavelength is

Constant Name	Explanation
T_ν	ΔE between the current state and another fixed state[1]
A_ν	Spin-Orbit Coupling Constant
B_ν	Rotational Constant
D_ν	Centrifugal Distortion Term for Quartic Correction
H_ν	Centrifugal Distortion Term for Sextic Correction
p_ν	Constant used for Lambda Doubling
q_ν	Constant used for Lambda Doubling
D_{A_ν}	Centrifugal Distortion Correction term for A_ν

Table 2.1: Constants used by PGOPHER to calculate the transition wavelengths. Not all of these constants are used for every level. The ones used for a given vibrational level depends on which ones the authors provided [23, 29–32]. H_ν is the result of additional correction terms to the Anharmonic Oscillator approximation, affecting the Nonrigid rotator approximation [13, 21, 23, 29–32]. Additionally, p_ν, q_ν are constants used to approximate the strength of Lambda Doubling [13, 21, 23, 29–32].

[1]Generally, either the ground state of the neutral molecule, or the ground state of the molecular ion.

given by the uncertainty of T_ν (which is what we used for uncertainty). Note that the spacing between rotational lines may be known to higher precision since T_ν's cancel.

2.2.2 Constant Choice From Literature

The most accurate literature to date, for molecular constants in the $X^2\Pi_g$ state of $O_2{}^+$ can be found in references [29–31].

For the vibrational states $\nu = 13 - 38$, we used the values found in [31] since there was no other reference providing molecular constants for these levels. For the vibrational levels $\nu = 2-12$, we used the values given in [30] since they gave values for more of the constants given in table 2.1. This results in a more accurate calculation of transition wavelengths for these states. Furthermore, the values in [31] and [30] agree within their respective uncertainties. Therefore, we can safely use [30]. Finally, for the levels $\nu = 0, 1$ we could have used both [31] and [29]. However, [31] mentions that the values in [29] are more precise. So, we mainly used the values in [29] and used [31] for parameters that [29] did not report a value for.

Data Obtention Methods of [29–31]: The oldest study in [29–31] is [29], followed by [31] and [30], respectively. [29] is the study of $A \rightarrow X$ emission spectrum where they used a mixture of helium and oxygen, which they pumped through a microwave discharge at 2.45 GHz. They then isolated–using a 1-m spectrometer–the emission at 408.2 nm. They obtained the strongest signal in the pressure ranges of ~ 0.05 Torr using pure oxygen. Subsequently, they passed pure oxygen through a liquid nitrogen cooled molecular seive column with a discharge power of 150 W. They obtained the photographs using a 3.5 m RSV spectrograph [29].

[30] is also an $A \rightarrow X$ emission spectrum study, and they obtained their first data by accident via a tungsten hollow cathode discharge. They used oxygen in a continuous fast flow with pressures of 0.2 Torr and 3.5 Torr neon, using a discharge of 221 mA of current. They then steered the output to a McMath-Pierce Fourier Transform Spectrometer. Their integration time was 54 minutes with a resolution of 0.03 cm^{-1}. Furthermore, they limited their scan region to $15900 - 30200$ cm^{-1}. The existence of neon lines allowed them to calibrate the spectrum [30].

Finally, [31] is a study utilizing the photoionization of the neutral oxygen molecule with one X-ray/vacuum-UV photon. They used a high-resolution photoionization facility of Chemical Dynamics Beamline at ALS. The instrument has "a 10 cm period undulator, a gas harmonic filter, a 6.65 m off-plane Eagle monochromator, and a photoion-photoelectron apparatus." Their harmonic gas filter suppressed undulator harmonics with greater than 24.59 eV photon energies, and they used helium in the gas filter. They then channeled the light to the 6.65 m monochromator with a 4800 lines/mm grating. After that, the light enters the experimental apparatus where they measure the PFI-PE (Pulsed Field Ionization Photoelectron Bands) bands with a resolution of $0.016 - 0.064$ angstroms (Full-Width Half Maximum). They also varied the photon energy step size between $0.1 - 0.25$ meV [31].

We wanted to calculate the transition energies with respect to the vibrational ground state of the $X^2\Pi_g$ state of O_2^+ and not with respect to the ground state of the neutral oxygen molecule. Therefore, we had to translate the T_ν values for the levels $\nu = 0, 1$ given in [29], since they give them with respect to the ground state of the neutral oxygen molecule. The actual values we used for these constants can be found in Appendix B, and the actual table with transition wavelengths can be found in Appendix C. All of the given values are in cm^{-1} unless specified otherwise.

Brief Introduction to PGHOPHER's Calculation Method: For finding the energy levels, PGOPHER expands the wavefunction–call Ψ_i–of a rovibrational level using basis states $|j\rangle$ [19]:

$$\Psi_i = \sum_j c_j^i \, |j\rangle \, . \tag{2.52}$$

In order to calculate c_j^i, the Hamiltonian is written in its matrix form and diagonalized using the basis states $|j\rangle$. In general–though there is a dependence of the basis states and the Hamiltonian to the system–basis states are typically in the form $|\eta s J K M\rangle$ where η designates the electronic and vibrational state (i.e. vibronic state) with the total electron spin. s denotes the rovibronic symmetry, J the total angular momentum, K the projection of J to a molecule-fixed axis, and finally, M the projection of J to a laboratory axis [19]. Furthermore, the basis kets $|\eta s J K M\rangle$ are themselves linear combinations of $|\eta J K M\rangle$. If we do not have any external electric or magnetic fields, the energy level does not depend on M. So, the only relevant basis states will be limited to states with single J and rovibronic symmetry s [19]. For a more detailed explanation of the calculation method along with the treatment of degeneracies and further functionalities of PGOPHER, please see [17–20]. Futhermore, PGOPHER calculates the eigenstates. For instance, we have two basis states (given by $\Omega = \frac{1}{2}, \frac{3}{2}$ for our experiment) and PGOPHER forms the eigenstates using these basis states' superposition [4, 17–20]. We are in Hund's case-(a), so the Hamiltonian

is almost diagonal for low J in case-(a) basis [4, 17–20].

Since our first experiments will try to measure the wavelength of $|O_2^+\ X^2\Pi_g, v = 0\rangle \rightarrow |O_2^+\ X^2\Pi_g, v = 16\rangle$ [11, 12], we also simulated this two-photon spectrum of $X^2\Pi_g$ O_2^+ with the assumption that we only had access to J = $\frac{1}{2}, \frac{3}{5}, \frac{5}{2}, \frac{7}{2}$ in our initial state $|O_2^+\ X^2\Pi_g, v = 0\rangle$, due to our state preparation technique [4, 12]. Our REMPI spectrum should agree with this simulation–given in fig. 2.2–provided that the spherical tensors $T(0,0)$, $T(2,0)$ and $T(2,2)$ have equal weight in calculation [4, 17].

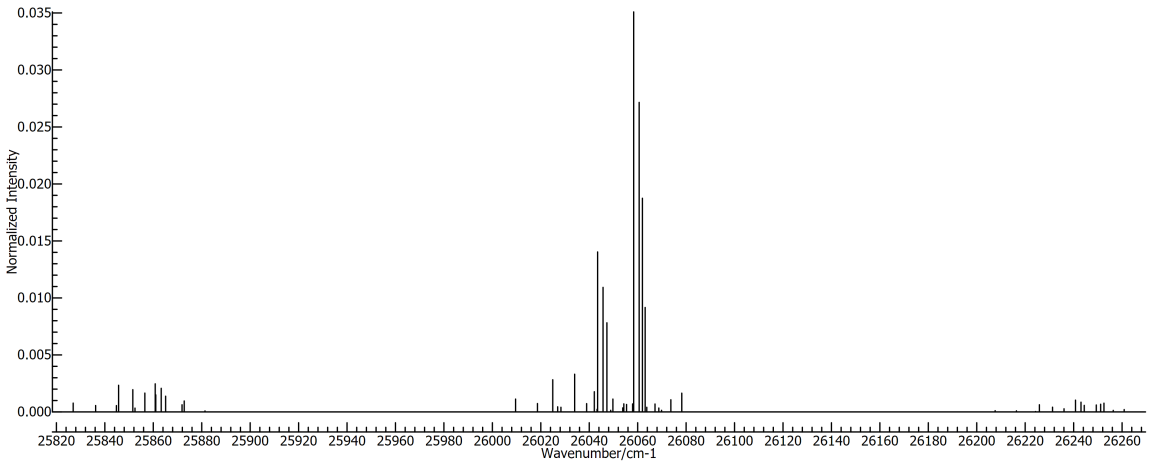

Figure 2.2: Simulation of the REMPI Spectrum we would expect for the transition from $\nu = 0$ to $\nu = 16$ level of $X^2\Pi_g$ O_2^+–using PGOPHER software–provided that the three components that make up the two-photon transition are weighed equally. These are the sperical tensors T(0,0), T(2,0) and T(2,2) where the first index is the rank and the second is the component. We have three clusters as expected. From left to right–respectively–they are $(\Omega_{\text{initial}} = \frac{3}{2}) \rightarrow (\Omega_{\text{final}} = \frac{1}{2})$, $(\Omega_{\text{initial}} = \frac{1}{2}) \rightarrow (\Omega_{\text{final}} = \frac{1}{2})$ with $(\Omega_{\text{initial}} = \frac{3}{2}) \rightarrow (\Omega_{\text{final}} = \frac{3}{2})$, and $(\Omega_{\text{initial}} = \frac{1}{2}) \rightarrow (\Omega_{\text{final}} = \frac{3}{2})$ [4, 17–20].

Chapter 3

Experimental Apparatus

Now that we know what we would like to achieve and the theory behind these transitions, we should design and build an apparatus that we can use to drive and measure the wavelength of these transitions.

3.1 Outline and Motivation

In order to detect oxygen molecular ions in the correct quantum state, we need to create them. We will be using a (2+1) REMPI method with our pulsed YAG laser from Quantel. However, we need molecular ions to be as cold as possible, preferably about 5 K. The coldness of the molecules allows us to spectroscopically choose a particular rotational state of interest. Furthermore, as we approach to 5 K, more of the molecules are in the ground vibrational and rotational states. This is particularly important since we are trying to drive the transition $|X^2\Pi_g, v = 0 > \rightarrow |X^2\Pi_g, v = 16 >$ [4, 11, 12, 14].

We will use free jet expansion to achieve the cooling, since our neutral oxygen molecule is already a gas in room temperature. After obtaining the correct state of the oxygen molecular ion, we need to detect it. Furthermore, our first short-term

goal is to measure the transition frequency of $|O_2^+, X^2\Pi_g, v = 0\rangle \rightarrow |O_2^+, X^2\Pi_g, v = \gamma\rangle$ with $\gamma > 0$ an integer, but this transition does not fluoresce (i.e. no photon emitted via decay). Therefore, we have to use a destructive method to detect the transition. We will use another photon that dissociates the oxygen molecule provided that it is in the right state. After the dissociation, we will look at the remaining molecules/atoms to see the strength of the transition at a given wavelength of laser [4, 11, 12, 14]. To do this, we accelerate ions through a Wiley-McLaren configuration (WML) Time of Flight Mass Spectrometer (ToF-MS), which consists of 3 parallel rectangular plates sourcing uniform electric fields [11, 16]. In ToF-MS, we have different atoms,molecules with the same charge and we give them all the same amount of kinetic energy. This causes them to have different speeds based on their mass. Since the arrival times of oxygen molecule and atom are different (given the same amount of energy), we can tell how much of the initial molecules we dissociated. Thus, the distribution of molecular ion to atomic ion will tell us about the strength of the transition at the wavelength we used to drive it [4, 11, 12, 14, 16].

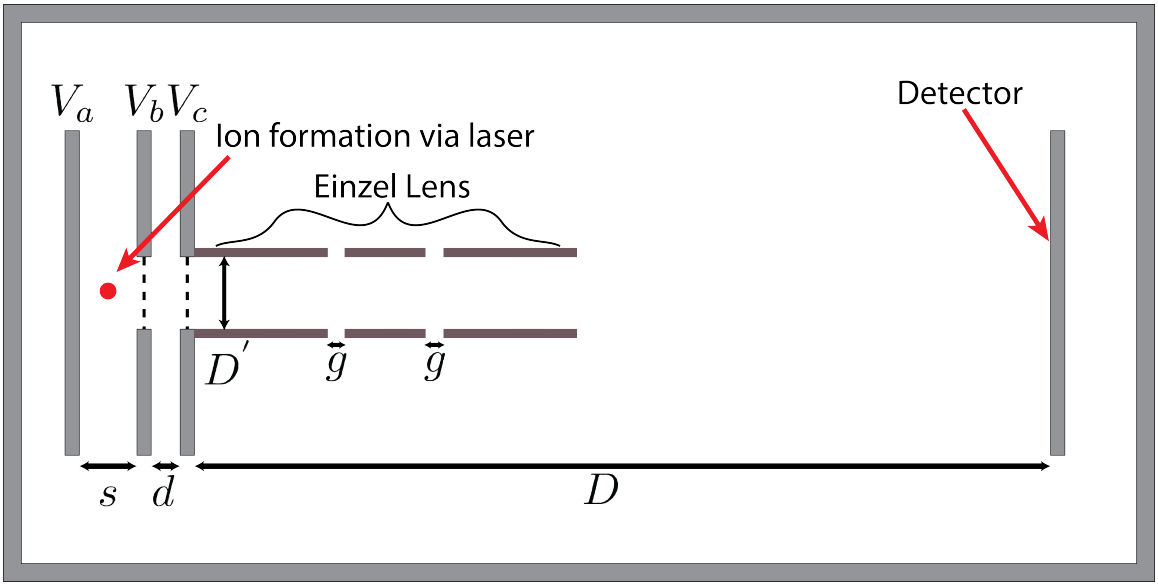

Figure 3.1: Schematics of the ToF-MS with Einzel Lens for optical focusing of the ions. Wiley-McLaren Configuration allows for flexible adjustments of time-spacing and space-focusing of the ions [16]. The ions are created at the red dot in the figure and are accelerated towards the detector from left-to-right thanks to the potential differences $V_b - V_a$ and then $V_c - V_b$ [16]. After exiting the experiment region (i.e. past place with voltage V_c), the ions are optically focused with the Einzel Lens [33–35].

There are two main reasons behind using a WML Configuration rather than just 2 parallel plates. Firstly, we have a ToF-MS which differentiates ions of equal charge based on their time of flight of a fixed distance [16]. Ions are given the same amount of energy in the acceleration section (i.e. the section between the parallel plates with uniform electric field) and then they drift through a field-free region. Compared to a 2 parallel plate scheme, a WML configuration allows us to adjust ions' arrival times so that they do not depend on inital space and velocity distributions of the ions [16].

Our plates do not have infinite surface area, and we cannot really have plate separation to be much smaller than the plate length. So, the plates only approximate parallel plate capacitors. Therefore, the electric field between the plates may not be totally uniform. To remedy for this potential irregularity of the electric field–which

will cause some of the ions to exit at an angle from the last plate–we add an Einzel Lens at the exit of the WML configuration to optically focus the ions to the central axis of the drift tube, as can be seen in figure 3.1. Succinctly, an Einzel Lens is a collection of electrodes with different voltages that alters the trajectory of the ions without changing their kinetic energy [33–35].

At the physical end of the spectrometer, we need a detector to capture the ions for spectroscopy. For that, we are using a Microchannel Plate Detector (MCP) [12]. Finally, for the physical construction of the apparatus, we wanted to have the flexibility to modify the apparatus in the future. Therefore, instead of using totally custom made parts, we used Kimball Physics' eV Parts products which are a collection of hundreds of standardized parts. We customized some of them with cuts and welds. These parts are divided in series B and C. Generally, parts in the same series are compatible with each other which turns assembly into sliding parts in their places. Using these parts makes future modifications to the assembly a matter of obtaining the right parts from series C (which is what we used) and building on top of the old one.

3.2 Apparatus Theory

3.2.1 Wiley-McLaren Configuration Acceleration Stage

A Wiley-McLaren configuration consists of 3 parallel plates separated by distances s and d, as shown in figure 3.2 [16]. We have two circular holes through the electrodes biased with V_b and V_c to make sure that ions can exit the acceleration stage after being formed by REMPI. These holes are covered with a metal mesh that creates an equipotential while still allowing ions to exit. The mesh is from the company TWP. It has 50 wires/inch with 0.0012" wire diameter. The wires are made of 316 stainless

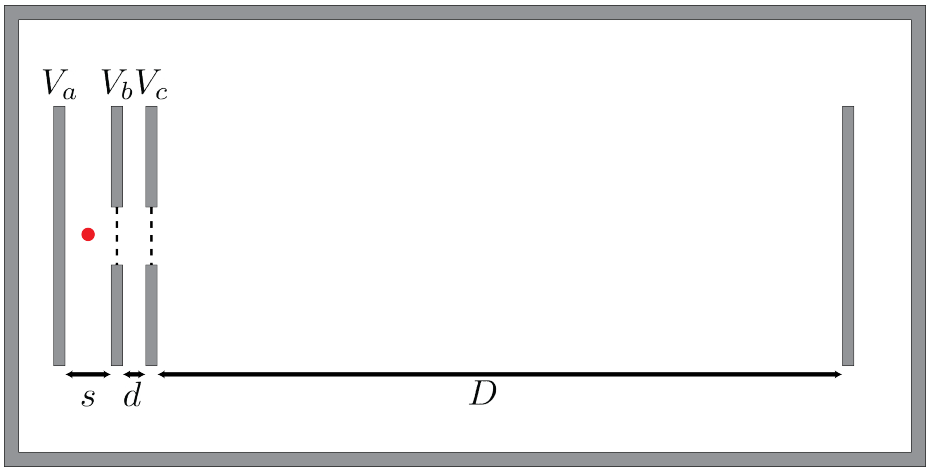

Figure 3.2: Schematics of the Wiley-McLaren Configuration for Ion Extraction, ions are created roughly in the middle of region s and accelerated to the detector D away from the last electrode [16].

steel, and the mesh has a transparency of 88%. Using this configuration, we would like this mass spectrometer to have 2 properties:

1. Ions with different masses should arrive at different times to the detector (i.e. $O_2^+$and O^+) [16].

2. The different ion distributions in time should not overlap with each other [16].

Assuming a Gaussian distribution of the arrival times of ions, these concepts are illustrated in 3.3:

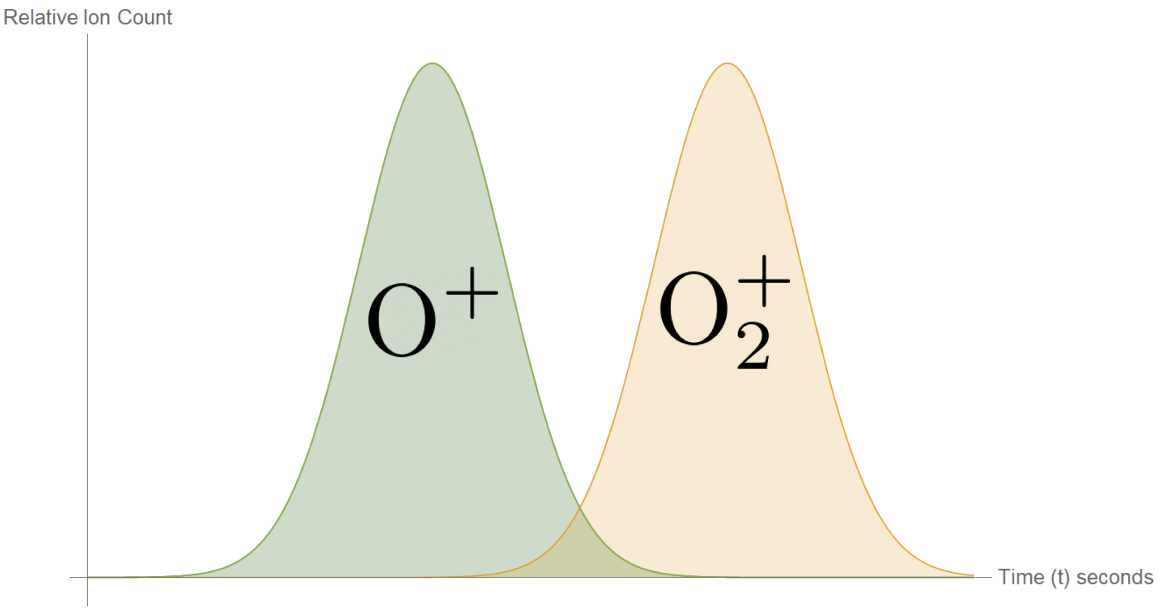

Figure 3.3: A descriptive (not drawn to scale [i.e. not $\sqrt{2}$ apart]) oscilloscope trace if the temporal overlap of different ions is not considered in the design. Here, we cannot distinguish the ions in the middle region which renders doing statistical analysis harder.

To eliminate this overlap and to make sure that we have temporal separation of ions of different masses, there are 2 factors to consider, the first one is called **space focusing** and the second one is called **time spacing** [16].

Space focusing is the following: suppose ions are created at position p in the middle of electrodes A and B. Since we cannot create all of the ions at the same position, there will be an error Δp in the distances of our ions to the exit [16]. In our case, this error will come from the diameter of our oxygen gas beam that we are ionizing and from the diameter of our laser beam [4]. So ions will be created at $p \pm \frac{1}{2}\Delta p$. The ions created nearer electrode A will receive more energy and will go faster, but they have farther to travel. Space focusing makes sure that the arrival time difference $\Delta T_{\Delta p}$ these spatially separated ions is as small as possible [16]. Furthermore, an additional source of positional error will happen due to the fact that we are ionizing for some length along the beam [4]. Here, the ions are assumed to have the same

initial velocity. The extreme case where they have anti-parallel velocities is handled by time spacing [16]. The setup for space focusing is illustrated in figure 3.4:

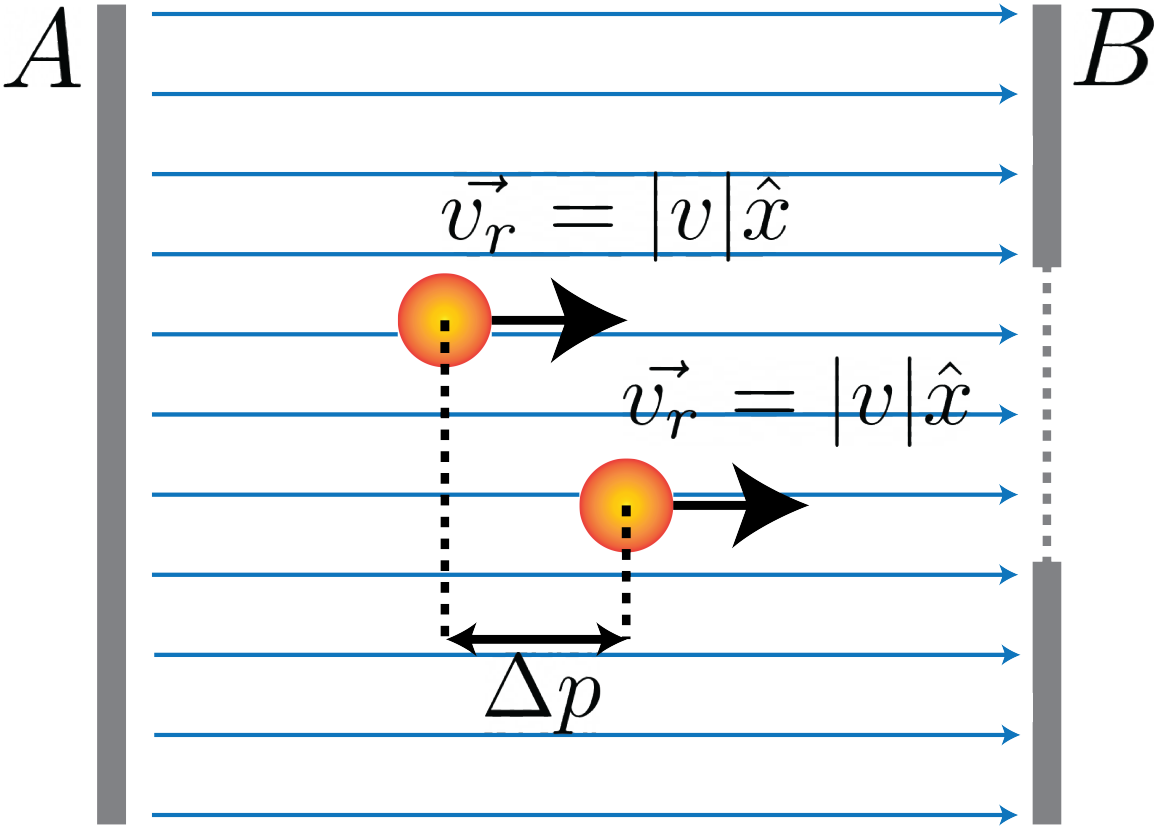

Figure 3.4: Setup for space focusing of ions illustrated. Space focusing makes sure that ions of the same type that get different energies–due to traveling through different lengths of accelerating electric field–arrive to the detector at the same time [16].

Time spacing is the following: suppose 2 ions are created at position p, but one is moving directly towards electrode B and the other is moving directly towards electrode A. Notice that in this case, the ion with an initial velocity towards the left (in figure 3.5) first needs to come to a halt, and then reverses direction [16]. Consequently, it gets a time delay compared to the ion with initial velocity towards the right. (In fact, when this ion reaches the position of the one with the initial velocity towards the right, it will have the same velocity as the other at that position.) [4, 16] Call this delay $\Delta T_{\rightleftharpoons}$. Time spacing tries to minimize the impact of this constant time delay

[16].

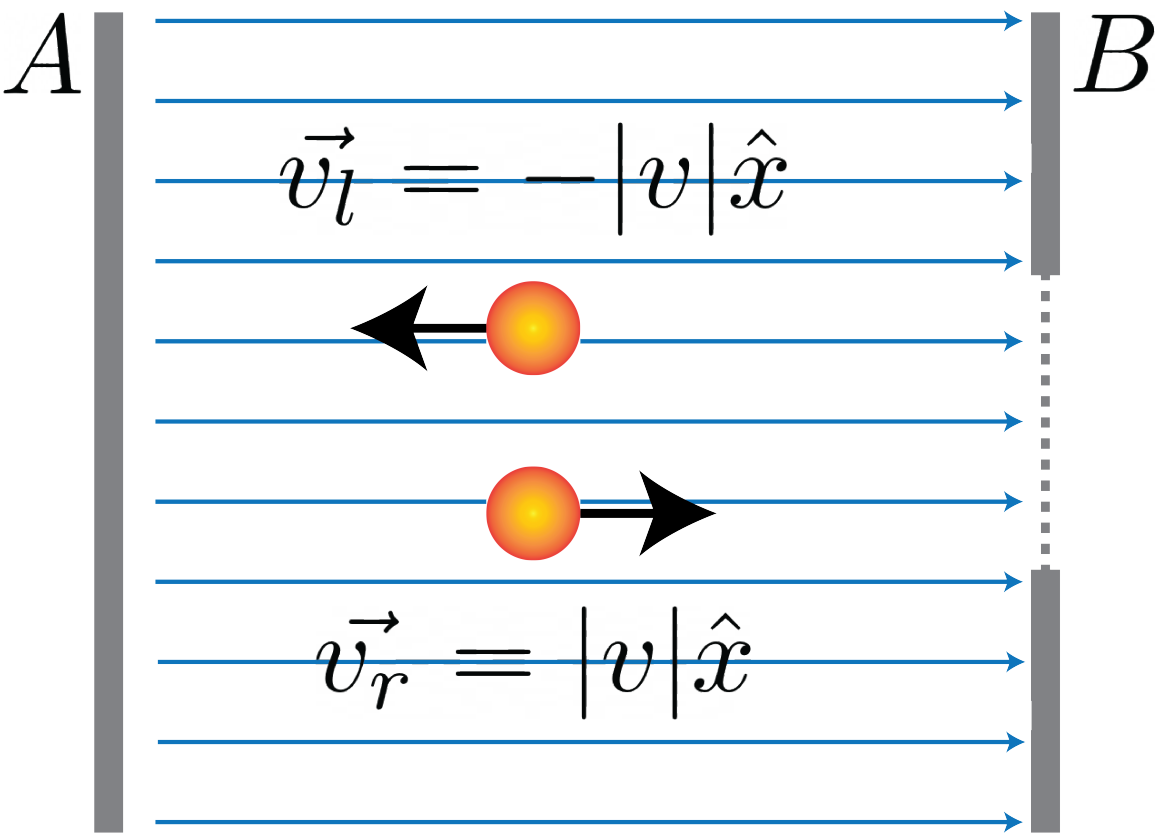

Figure 3.5: Setup for time spacing of the ions, illustrated. Time spacing makes sure that the constant time delay between ions created at the same position but with anti-parallel initial velocities do not prevent us distinguishing ions with different masses [4, 16].

Before a quantitative analysis of the WML configuration, we need to clarify that neither space-focusing nor time-spacing has anything to do with the optical focusing of the ions. These procedures focus the ions in time [16]. The optical focusing may not be needed in an ideal case with perfect parallel plates and ions created at a single point at the center of the cuboid formed by the two electrodes between which our ions are formed. In that case, the ions would be accelerated exactly in a straight line coinciding with the location of our detector. On the other hand, if the approximation does not hold, the optical focusing will be achieved with an Einzel Lens placed at the end of WML setup. Optical focusing may still be needed even when the parallel plate

approximation holds, since we create the ions along the whole laser and that region might be bigger than the diameter of the MCP [4, 33–35].

3.2.2 Quantitative Analysis of WML

The ions are created roughly in the middle of the region s, between the electrodes A and B. They travel through a region s_0 and the entire region d. So, we have $s_0 \approx \frac{s}{2}$. Therefore, if they have an initial kinetic energy of U_0, the ions will have a final energy of [16]

$$U = U_0 + qs_0E_s + qdE_d, \tag{3.1}$$

where E_s, E_d are the electric fields of regions s and d. They are assumed to be constant due to parallel plate capacitor approximation. Then, the time of flight is just the sum of time it takes the ions to fly through regions s, d and D. In the case of a field-free region D, they are given by [16]

$$T_s = \frac{\sqrt{2m}}{qE_s}(\sqrt{U_0 + qs_0E_s} \pm \sqrt{U_0}), \tag{3.2}$$

$$T_d = \frac{\sqrt{2m}}{qE_d}(\sqrt{U} - \sqrt{U_0 + qs_0E_s}), \tag{3.3}$$

$$T_D = \frac{\sqrt{2m}D}{2\sqrt{U}}. \tag{3.4}$$

In T_s, the plus-minus sign differentiates between the ions–at the time of creation–with velocities away from or towards the exit [16]. Now, if we accelerate the ions through a big enough electric field such that the initial energy U_0 is negligible, the entire time-of-flight formula simplifies to [16]

$$T_{tot} = \sqrt{\frac{m}{2U_{tot}}}\left(2\sqrt{k_0}s_0 + \frac{2\sqrt{k_0}d}{1+\sqrt{k_0}} + D\right), \tag{3.5}$$

where we have k_0 and U_{tot} defined as [16]

$$k_0 = \frac{s_0 E_s + dE_d}{s_0 E_s}, \tag{3.6}$$

$$U_{tot} = qs_0 E_s + qdE_d. \tag{3.7}$$

As a reminder, here k_0 is a simple unitless constant (for a given voltage configuration) substitution to write the total travel time more compactly [16].

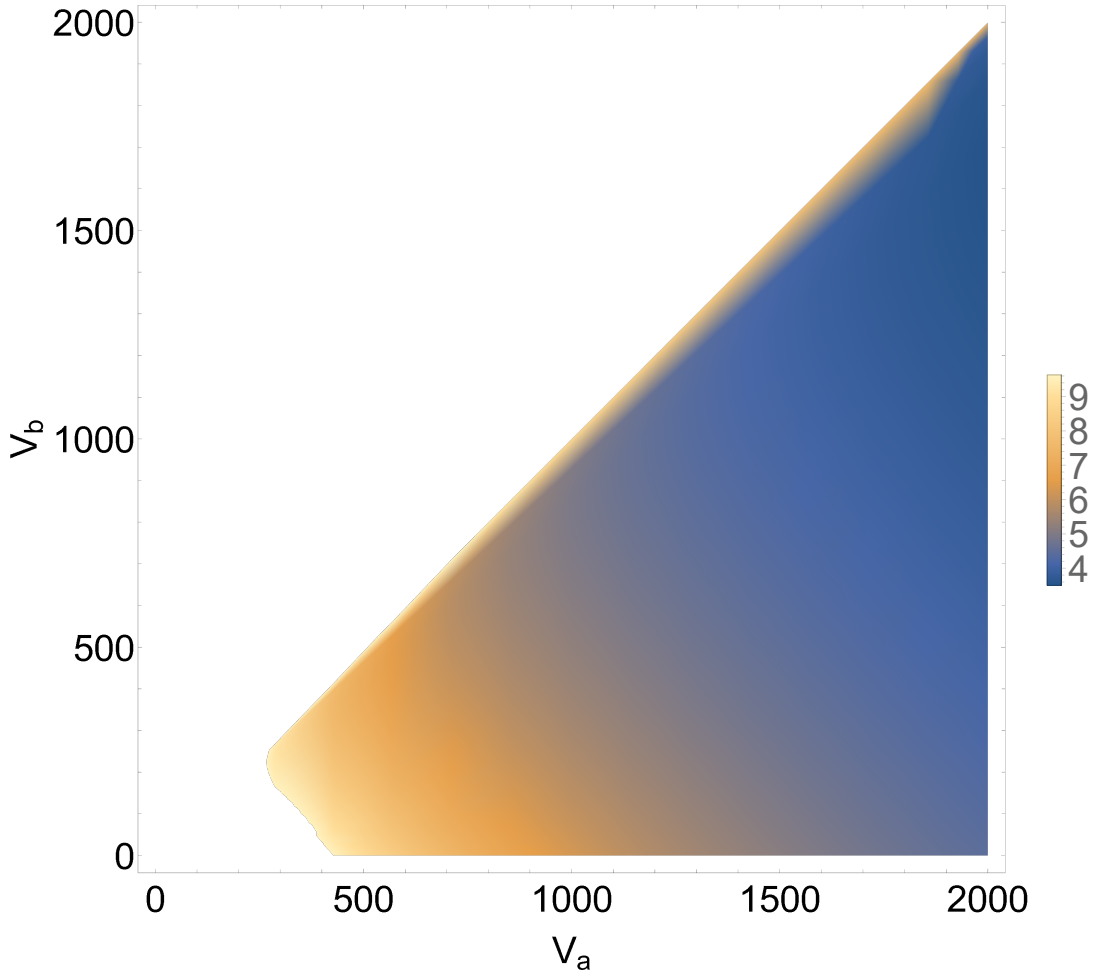

Figure 3.6: Travel time of oxygen molecular ion (32 amu) depending on the back and middle plate voltages. For the atomic ion, there should just be an additional factor of $\frac{1}{\sqrt{2}}$. This plot assumes that ions go through half of the entire region s (i.e. $s_0 = \frac{s}{2}$) and d. The contours' unit is microseconds (μs).

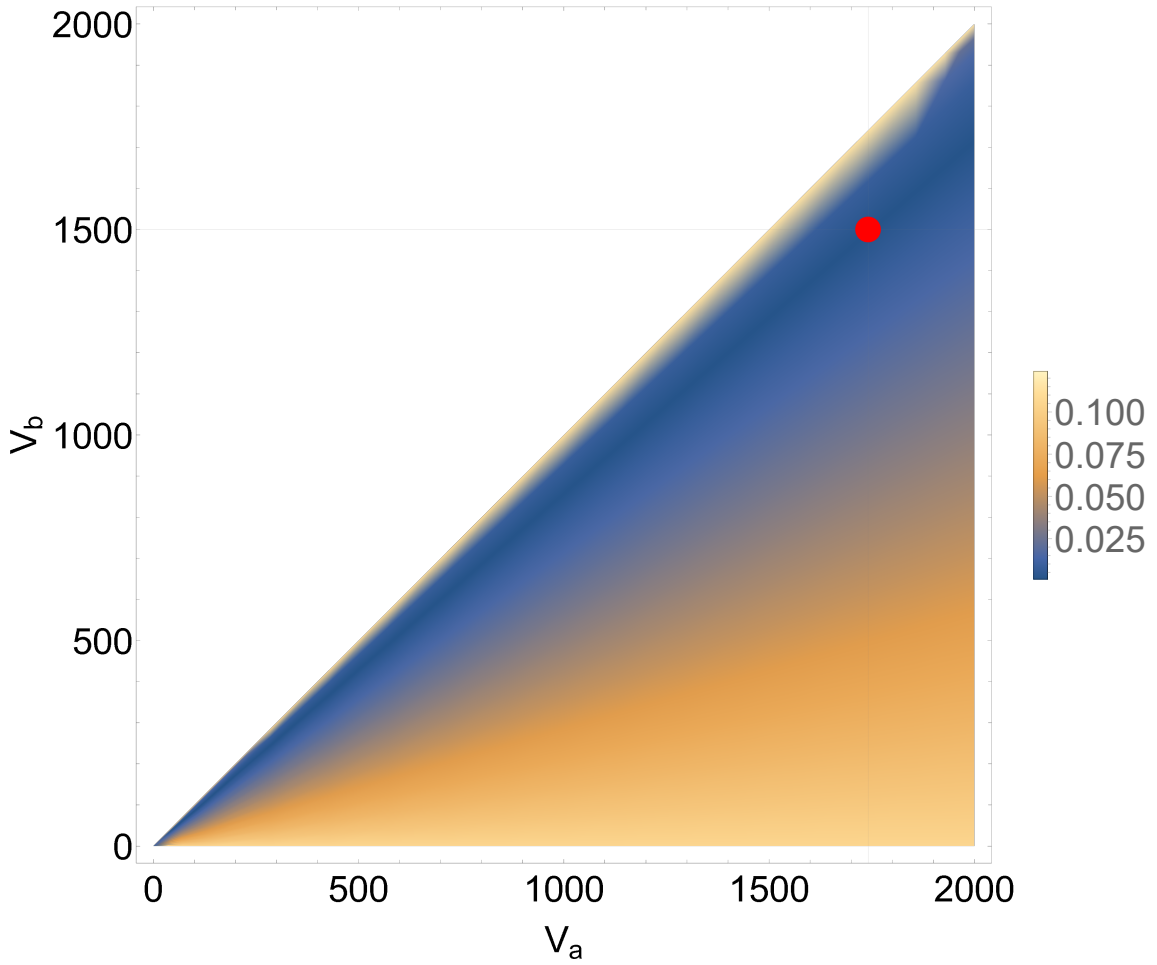

Figure 3.7: Normalized absolute value of the travel time difference of two oxygen molecular ions (32 amu, one at position $\frac{s}{2}$, the other at $\frac{s}{2} + \Delta s$ where $\Delta s = 0.001$ meters) depending on the back and middle plate voltages. For the atomic ion, there should just be an additional factor of $\frac{1}{\sqrt{2}}$. Notice that you can clearly see the space focusing effect on the differential time of arrival. We also see that our voltage configuration is in the most optimal band (denoted by the red dot on figure). The contours are unitless.

First, remember that we have $s_0 \approx \frac{s}{2}$. Now, for space-focusing we would like to make sure that ions created at $s_0 + \Delta s_0$ and $s_0 - \Delta s_0$ reach the MCP at the same time. So, we should have [16]

$$\left(\frac{dT_{tot}}{ds}\right)_{s_0} = 0, \tag{3.8}$$

since this will make sure that $T_{tot}(s)$ is roughly constant around s_0. Using this and

isolating D, we get [16]

$$D = 2s_0\sqrt{k_0^3}\Big(1 - \frac{d}{[k_0 + \sqrt{k_0}]s_0}\Big). \tag{3.9}$$

Notice then that we have 4 independent variables $D, s, d, \frac{E_d}{E_s}$. Therefore, we can set any 3 of them and the last one will be completely determined [16]. In our case, the easiest one we can adjust is $\frac{E_d}{E_s}$ since that only involves voltage adjustments. Furthermore, we would like to have parallel plate capacitor approximation to hold true, which restricts our flexibility on s, d. Therefore, we will fix s, d, D. Now, notice that equation 2.8 implies that we either have a maxima, minima or an inflection point at s_0. Generally with the most suitable parameters we choose to have the maximum mass resolution, we have a maximum at s_0 [16]. This gives us another requirement, which is [16]

$$\frac{d}{s_0} < \frac{(k_0 - 3)D}{2s_0k_0}. \tag{3.10}$$

The mass resolution of a mass spectrometer is defined as the highest amu m such that the spectrometer can distinguish ions of mass m and $m-1$ amu [16]. Therefore, we would like to have a mass resolution of at least 32 amus (O_2^+), but ideally, we would like to have as big a mass resolution as we can get. Hence, we will use equation 3.10 in calculation of parameters. As we will see in the following paragraphs, mass resolution increases with increasing k_0. So, we would like to have k_0 as big as possible. (This is the main reason why we have a maxima at s_0 since we also have $D >> d$) [16]. Notice that if $k_0 \leq 3$ then we always have a minima. So, we have an additional constraint that is [16]

$$k_0 > 3. \tag{3.11}$$

Now, we should treat time-spacing. Suppose two ions are created at the same position p but with anti-parallel velocities. One of them (call Alice) has a velocity directly towards the exit, and other (call David) has a velocity directly away from the the exit.

Alice will get accelerated immediately towards the detector, whilst David first will get decelerated by the electric field and then change direction, come to the starting position, and then follow the trajectory Alice started a time $\Delta T_{turnaround}$ ago [16]. This time lag is called the "turn-around" time, which can be shown to be [16]

$$\Delta T_{turnaround} = \frac{2v_0 m}{qE_s} = \frac{2\sqrt{2mU_0}}{qE_s}. \tag{3.12}$$

In time-spacing, we try to make sure that the arrival time distribution of adjacent masses (i.e. masses of k and $k-1$ amu) are separated by more than this $\Delta T_{turnaround}$. The first mass k at which the arrival time distributions of adjacent masses is equal to the turn-around time determines our time-spacing mass resolution M_{ts} [16]. This is the resolution we would get if the only factor on mass resolution were to be time-spacing. Notice that the naming can be a bit deceiving here, since unlike space-focusing, there is no actual temporal modifications to ions' arrival times in time-spacing [16]. Again, it is a constant delay that we are trying to minimize the effect of [16]. Using equations $2.5, 2.14$ with masses $m, m+1$. M_{ts} can be shown to be [16]

$$M_{ts} = \frac{1}{4}\sqrt{\frac{U_{tot}}{U_0}}\Big(\frac{k_0+1}{\sqrt{k_0}} - \frac{(\sqrt{k_0}-1)d}{(k_0+\sqrt{k_0})s_0}\Big). \tag{3.13}$$

Now, let us calculate the mass resolution M_{sf} due to space-focusing alone. First, series expand $T(s)$ of equation 2.5 around s_0. Then, use the expansion to take the difference of $T(s)$ and $T(s+\delta s)$ to obtain the arrival time difference of [16]

$$\Delta T_{sf} = \sum_{n=1}^{\infty} \frac{1}{n!}\Big(\frac{d^n T}{ds^n}\Big)_{s_0} (\delta s)^n. \tag{3.14}$$

Now we define the space-focusing mass resolution M_{sf} to be the largest number of amu's k such that [16]

$$\Delta T_{sf} < T_{k+1} - T_k, \tag{3.15}$$

where $T_{k+1} - T_k$ can be found by using equation 2.5 to be [16]

$$T_{k+1} - T_k = \Big(\sqrt{1 + \frac{1}{m}} - 1\Big)T_k \simeq \frac{T_k}{2m}. \tag{3.16}$$

So, we would like to find the mass k such that $\Delta T_{sf} = T_{k+1} - T_k \simeq \frac{T_k}{2m}$ to find our space-focusing mass resolution. Unfortunately, ΔT_{sf} is an infinite series, however, if we make some approximations we can simplify the expression [16]. First note that, in evaluating ΔT_{sf} we should use $\Delta s^{'} = \frac{\Delta s}{2}$ since the deviation from s_0 is $\pm\frac{\Delta s}{2}$. Furthermore, we will only use the first non-zero term in the series. Since, we have a maximum at s_0, the first term is zero [16]. Therefore, we use the $n = 2$ term. Differentiating equation 2.5 twice, and making the assumptions $k_0 >> 1$, $k_0 >> \frac{d}{s_0}$ we can find the space-focusing mass resolution to be [16]

$$M_{sf} \approx \frac{16 k_0 s_0^2}{\Delta s^2}. \tag{3.17}$$

Now, we need to determine what is the overall resolution of our ToF-MS device. Giving a precise number is hard to accomplish. However, we can easily find a lower bound and higher to our resolution. First of all, it is clear that we cannot have a higher mass resolution than M_{sf}, or M_{ts} [16]. On the other hand, if we suppose that the total time variation in arrival times of a given type of ion is the sum of the time differences found for space-focusing and time-spacing, we can make an error propagation like analysis and say that the overall resolution will be bigger than or equal to M_{lb}, which is given by [16]

$$M_{lb} = \Big(\frac{1}{M_{sf}} + \frac{1}{M_{ts}}\Big)^{-1}. \tag{3.18}$$

Notice that the time-spacing portion of our analysis becomes less relevant in the determination of our overall resolution with the approximation $U_0 \approx 0J$. If we look

at equation 2.15 and replace $U_0 \approx 0J$, we get an effective time-spacing resolution of $M_{ts} \approx \infty$. Therefore, the overall resolution further simplifies to [16]

$$M_{lb} \approx M_{sf}. \tag{3.19}$$

As a rule of thumb for design parameters, it is preferable to have sE_s be much smaller than dE_d, i.e. we first extract the ions away from the gas path and then we apply the major accelerating field. This rule may not hold true, if the ions' velocity–parallel to the exit-hole plane–is high enough to make them miss the exit with such a small sE_s. In other words, if U_0 is sufficiently higher than 0 the rule may not hold [4, 16].

3.2.3 Einzel Lenses

Before discussing Einzel lenses we should introduce Electrostatic lenses, to which Einzel lens belong to. Electrostatic lenses are any collection of electrodes with specified voltages that can be used to change the trajectory of ions in a desired manner. As an analogy to optical lenses, one can think of the ions as the light beam and electrostatic lenses as the optical lens [33–35]. Electrostatic lenses can be formed by two/three concentric cylindrical electrodes separated by a distance, two/three concentric arrangement 4 plate electrodes arranged in a square/rectangle, and in many other possible combinations [33–35]. Here, we will focus on the explanation of cylinder lenses. However, a similar analysis applies to rectangular lenses. We chose to use cylindrical lenses, since it is easier to construct and to mount in place in our vacuum chamber. Furthermore, we used reference [35] in choosing a lens with suitable focal lengths for our experiment. The authors there give results for three-cylinder lenses.

In cylindrical lenses, we let ions travel through the center of the cylinders. These cylinders have a constant voltage applied to them. Since the electrode is cylindrically

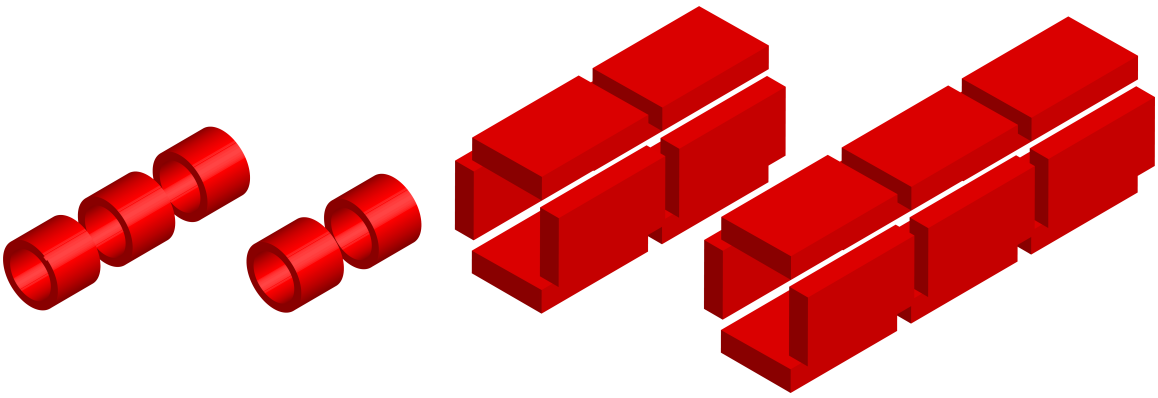

Figure 3.8: Here we illustrate 4 different approaches to making electrostatic lenses using stacks of 2 and 3 of the same base electrode combination. The first two use cylindrical electrodes while the last two use rectangular plates. Ions are focused due to the curvature of the electric field between the stacks [33–35].

symmetric, there is no net electric field inside the cylinder if the cylinders are infinitely long [33–35]. Therefore, the ions do not feel a force when they are traveling through a given cylinder. Since we have only finite cylinders, there will be a net electric field within the cylinder. So, if we put the neighboring electrode at a different voltage than the one that the ion just traveled through, there will be fringing fields between these two cylindrical electrodes. This fringing field will alter the trajectory of the ion, bringing it to a focus or defocus [33–35]. This phenomenon is illustrated in 3.9:

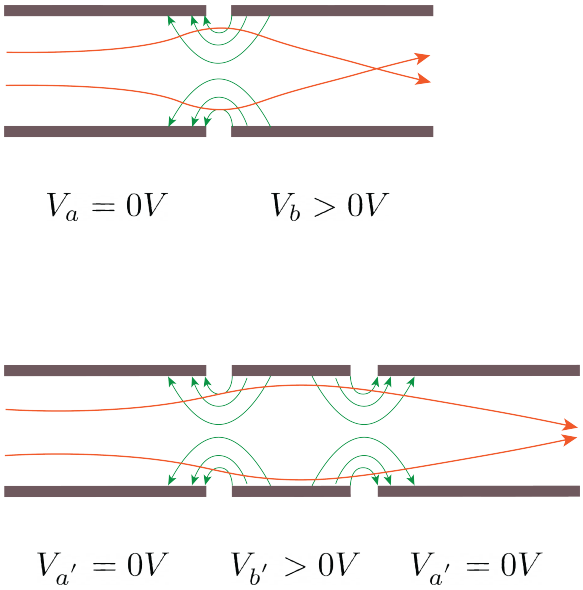

Figure 3.9: Sample ion trajectories for two-cylinder and three-cylinder lenses. Both trajectories (orange line) are for a positive ion. The outer electrodes are held at ground–for the three-cylinder setup–to avoid any leaking fields into the drift tube.

In our case, we will have positive ions and we want to have a converging lens to hit a comparatively small circular detector with a 17.78 mm diameter. We will also use a 3 cylinder lens with outer two cylinders at ground and the middle cylinder above ground, which is called an "Einzel" or Unipotential Lens [33–35]. Contrary to the two cylinder lens in fig. 3.8, Einzel lenses focus ions without changing their overall kinetic energy. This is desirable since we are differentiating our ions based on their free flight-times (given a constant kinetic energy) [33–35].

Einzel lenses are thick lenses. This implies that the thickness of the lens is close to its focal lengths [33–35]. Thick lenses are illustrated in figure 3.10:

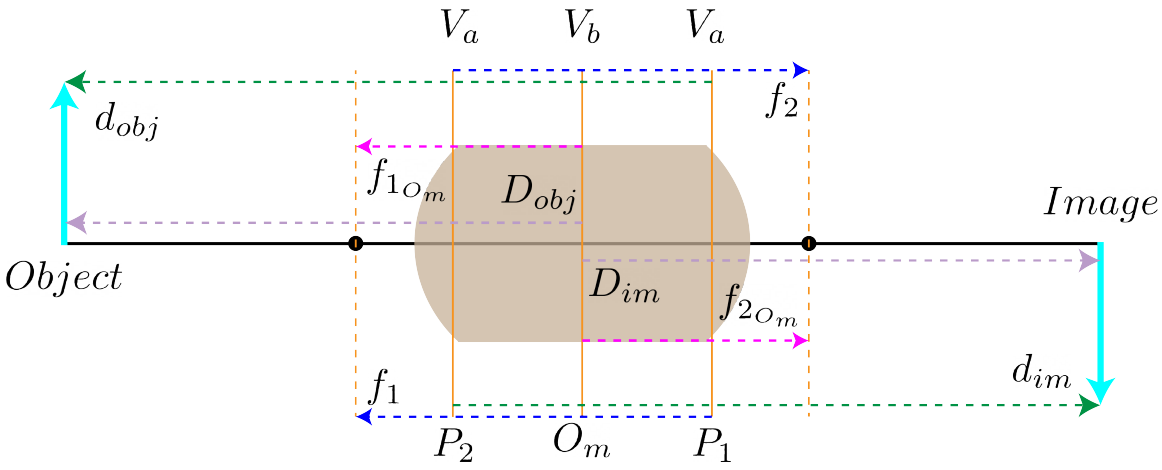

Figure 3.10: Optical diagram of an Einzel lens. Since it is a thick lens, we have to have 2 focii and 2 principal planes. Notice that principal planes P_1 and P_2 are always crossed on the opposite sides of the lens, relative to their focii [33–35].

Contrary to thin lenses, thick lenses have 2 principal planes P_1, P_2 and 2 associated focal points f_1 and f_2. In 3.10, $f_{1_{O_m}}$ and $f_{2_{O_m}}$ denote the focal lengths measured from the midplane O_m. Principal planes P_1, P_2 are always crossed in lenses used in ion optics [33–35]. In the case of 2 element lenses, the principal planes are always located in the low voltage side of the lens. In our case of a 3 element Einzel lens with outer electrodes at the same voltage, principal planes are still crossed. So, the principal plane associated with the left side of the lens is closer to the right side of the lens and vice versa. However, they are equidistant to the midplane O_m [33–35]. Again due to the voltage symmetry, we have $f_{1_{O_m}} = f_{2_{O_m}} = f_{O_m}$ and $f_1 = f_2 = f$. Furthermore, if the lens is not too strong, the principal planes P_1 and P_2 are very close to the midplane O_m of the lens. Therefore, we can approximate $d_{obj} \approx D_{obj}$ and $d_{im} \approx D_{im}$ [33]. Some quick relationships for generalized electrostatic lenses can be derived using classical geometric optics. First of all, angular and linear magnifications M_{ang}, M_{lin} are given by [33]

$$M_{ling} = \frac{f_2 - d_{im}}{f_2} = \frac{f_1}{f_1 - d_{obj}}, \tag{3.20}$$

$$M_{ang} = \frac{f_1 - d_{obj}}{f_2} = \frac{f_1}{f_2 - d_{im}}. \tag{3.21}$$

Using Newton's law and Newton's formula–respectively– we obtain [33]

$$(d_{obj} - f_1)(d_{im} - f_2) = (D_{obj} - f_{1_{Om}})(D_{im} - f_{2_{Om}}) = f_1 f_2, \tag{3.22}$$

$$\frac{f_1}{d_{obj}} + \frac{f_2}{d_{im}} = 1. \tag{3.23}$$

Since we are using an Einzel lens that has symmetry with respect to the mid-plane O_m with $f_1 = f_2 = f$, this expression simplifies to [33]

$$\frac{f_1}{d_{obj}} + \frac{f_2}{d_{im}} = \frac{f}{d_{obj}} + \frac{f}{d_{im}} = 1 \approx \frac{f}{D_{obj}} + \frac{f}{D_{im}}, \tag{3.24}$$

which–when rearranged–turns into the standard formula used for thin lenses [33]

$$\frac{1}{f} \approx \frac{1}{D_{obj}} + \frac{1}{D_{im}}. \tag{3.25}$$

The main challenge is to actually find this focal length f given an Einzel lens configuration with voltages V_b, $V_a = 0V$ applied to inner electrode and outer electrodes–respectively–with diameter $D^{'}$ and electrode separation g as can be seen in figures 3.1,3.9,3.10. To achieve this, we define an axial potential $\Phi(z)$ where the z-axis is chosen as shown in figure 3.10. Notice that the axial potential does not depend on x,y coordinates within the lens, because–ideally–the electric field inside the lens is identically zero due to cylindrical symmetry. Now, if we know this axial potential, we can find the focal length f by integrating the ray equation [33, 34]

$$\frac{d^2\varrho}{dz^2} + \frac{3}{16}\Big(\frac{\Phi^{'}}{\Phi}\Big)^2 \varrho = 0. \tag{3.26}$$

where $\varrho = r\sqrt[4]{\Phi}$ and r is the distance of the ray to the z-axis. The tuple (r, z) is also called the ray vector [33]. Generally, $\Phi(z)$ is found numerically, and therefore, the integration of equation 2.29 is also done numerically. One procedure to find $\Phi(z)$ for our lens starts with dividing the cylindrical elements into small annuli and calculating the charge densities each annuli has. Remember that if we do not have any dielectrics, the potential $\Phi(z)$ is completely determined by free surface charges of the conductors. After finding these charge densities, one uses them to compute the axial potential [34].

Before we start the quantitative analysis, we need to make a few assumptions to simplify our calculations. First, we assume that the thickness of the hollow cylinders– from which we constructed the lens assembly– is much smaller than their radius. This allows us to consider the charge densities on the outside and inside surfaces of a given annuli as a single charge sheet [34, 35]. We may do this since only the sum of these two charge sheets determine the potential of places not close to the hollow cylinder. Therefore, if the thickness of the cylinder is much smaller than its radius, we may regard points around the z axis to be far away from the inner/outer surfaces [34].

So, we have annuli $\mathcal{C}_i$ with voltages V_i and vector $\mathbf{r_i}$ from the origin to the surface of annulus $\mathcal{C}_i$. If the total charge density on the annulus i is $\sigma_i(\mathbf{r_i})$ with no additional charges, then potential at $\mathbf{r}$ is [34]

$$U(\mathbf{r}) = \frac{1}{4\pi\epsilon_0} \sum_i \int_{A_i} \frac{\sigma_i(\mathbf{r_i}) dA_i}{|\mathbf{r} - \mathbf{r_i}|}, \tag{3.27}$$

where A_i is the surface of the annulus $\mathcal{C}_\rangle$. Notice that every A_i is equipotential. Therefore, [34]

$$U(\mathbf{r_j}) = V_j = \frac{1}{4\pi\epsilon_0} \sum_i \int_{A_i} \frac{\sigma_i(\mathbf{r_i}) dA_i}{|\mathbf{r_j} - \mathbf{r_i}|}, \tag{3.28}$$

where $\mathbf{r_j}$ is on A_j. The process for finding these charge densities has 6 steps: [34]

1. Divide the cylinders into annuli each of which having uniform surface charge density σ_i.

2. Make an initial guess σ_i^0 for these charge densities.

3. Find the resulting potential U_i^0 on the surface of each annuli i resulting from the guessed charge densities, using equation 2.31.

4. Find the error ($\Delta U = U_i^0 - V_i$) between the applied potential and the one found from the guesses

5. Use these errors to refine your guesses for the charge densities, and repeat 2,3,4 until you get the precision you would prefer.

6. Calculate potential $U(\mathbf{r})$ everywhere using equation 2.30.

Now that we are more familiar with the theory behind Einzel lenses, let us discuss why we might need one in our experiment before discussing how we obtain our cold molecular beam. Remember that the main premise of our ToF-MS is the existence of a uniform electric field between our accelerating plates. In reality, this is only approximate since the length of our plates and their separation are comparable. Furthermore, our ions have initial velocities of several hundreds of meters per second at moment of creation [4]. Therefore, in practice, the ions will not travel in an exactly straight trajectory towards our detector. So, depending on whether we have enough signal, we will use the Einzel lens to push the ions going off-track towards our detector to increase our signal. Finally, for the actual designed lens in the next section, we will use the already calculated values from [35].

3.2.4 Free Jet Expansion

In the outline section, we motivated for the use of free jet expansion, now we glance at the underlying physics of it. For a detailed explanation of the physics, see [12, 15].

Remember that we would like our gas to be around 5K for the ease of state preparation of the molecular oxygen ion, especially to have the molecules in the ground rotational level [4, 11, 12]. Therefore, simply leaking gas into the chamber is not desirable, since that would result in a gas temperature of 300 K. Furthermore, our Microchannel Plate Detector (MCP)–for ion detection–is very sensitive to pressure and humidity, therefore, a constant gas leak might easily cause shorts within the detector, thereby ruining it [4, 12]. Consequently, we will be pulsing the oxygen gas into the chamber to reduce the gas load, and use free jet expansion to rotationally, translationally and vibrationally cool the gas [12, 15].

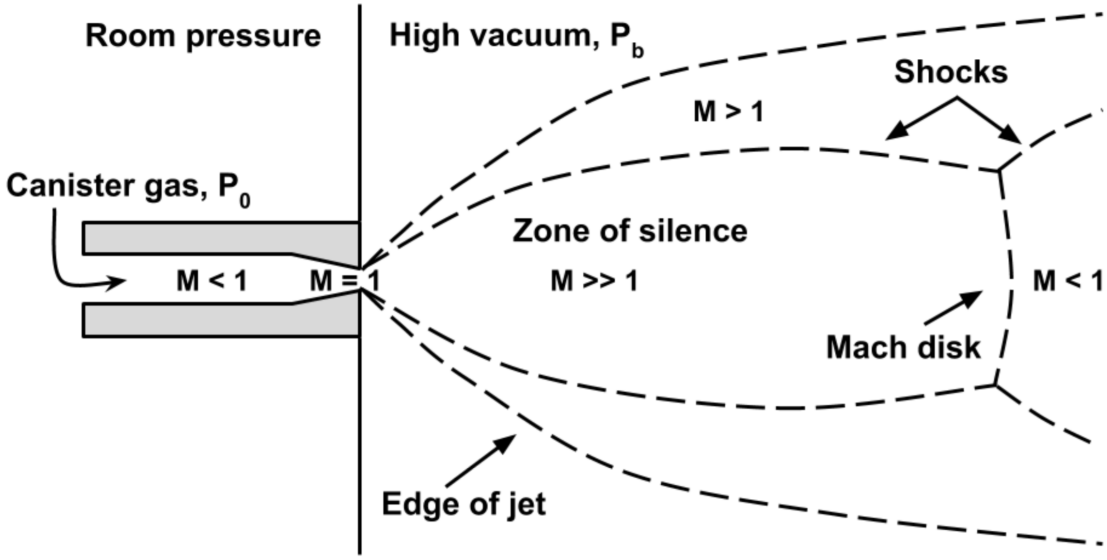

Figure 3.11: A schematic of the free jet expansion. M denotes the speed of the gas in terms of Mach. Our experimental region should be within the zone of silence after the quitting surface, which can be seen in figure 3.12. After the quitting surface, we have free molecular flow with supersonic speed until the Mach disk [12, 15]. Figure taken from [12], under Creative Commons Attribution (CC BY) license

In the free jet expansion, our gas starts in the canister with pressure P_0 and temperature T_0. After we open the canister to the high vacuum chamber with background pressure P_b, the pressure difference $P_0 - P_b$ accelerates our gas, since the radius of the opening to the chamber decreases as the gas comes closer to the exit as can be seen

from figure 3.11 [12, 15]. If the pressure proportion $\frac{P_0}{P_b}$ is higher than $G = (\frac{\gamma+1}{2})^{\frac{\gamma}{\gamma-1}}$, our gas reaches a mean velocity in the supersonic range. For all gases we have, $G < 2.1$. If we have $\frac{P_0}{P_b} < G$, then our gas will flow subsonically and the exit pressure of the gas will be $\approx P_b$. For values where $\frac{P_0}{P_b} > G$, the pressure at the exit approaches $\frac{P_0}{G}$ [12, 15]. Notice since our exit pressure is higher than the background pressure, the gas has to further expand due to the boundary conditions created by the background pressure P_b. Therefore, gas in this condition is called to be "underexpanded" [12, 15].

There are a few important traits of the supersonic flow that are of particular relevance to us. First of all, the gas velocity (in units of Mach) is denoted M, which increases with a coupled increase in the flow area [12, 15]. Therefore, we have $M > 1$ after the exit. Also, since the information travels at the speed of sound inside the gas, $M > 1$ implies that the upstream gas has no knowledge about any of the shocks that occur [12, 15]. Therefore, the dynamics of our gas is simple for our analysis. However, the gas still has to adjust even though it does not know about the boundary conditions. This apparent paradox gives rise to shock waves which have large pressure, density and temperature [12, 15]. These shock regions–which can be seen in figure 3.11–are nonisentropic. Initially, our gas expands isentropically with M increasing, and it overexpands since it has no knowledge about P_b. Then the shock waves appear which recompress our gas so that it obeys the boundary conditions [12, 15]. The shock waves at the sides of the expansion are called "Barrel Shock." We also have another shock wave normal to the propagation direction, called the "Mach Disk." It is named such because the gas very quickly decelerates and goes back to flowing subsonically after it [12, 15]. This is–of course– for a general case. The dimensions of our experimental setup are small enough to never have a Mach Disk within the apparatus [12, 15].

The location of the Mach disk is given by [12, 15]

$$(\frac{x_M}{d}) = 0.67\sqrt{(\frac{P_0}{P_b})}, \tag{3.29}$$

where d is the nozzle diameter. The middle portion between the two barrel shocks and the Mach Disk in figure 3.11 is called the *zone of silence* where the expansion is isentropic with properties independent of P_b due to supersonic flow. Therefore, since the dynamics of the gas are simpler there, our molecules to experiment on will be taken from here by using a skimmer to just have the very center of the beam in our experiment [12, 15]. There is one additional criteria that we need to take into consideration. The flow in the zone of silence starts as a continuum flow. However, as the gas expands, the number of collisions decrease and after some point the number of collisions is not enough to keep the continuum flow. So, the gas transitions into free molecular flow [12, 15]. Therefore, our experimental region should be located at this free flow region of the zone of silence. The transition from continuum flow to free molecular flow is marked as the "Quitting Surface" [12, 15].

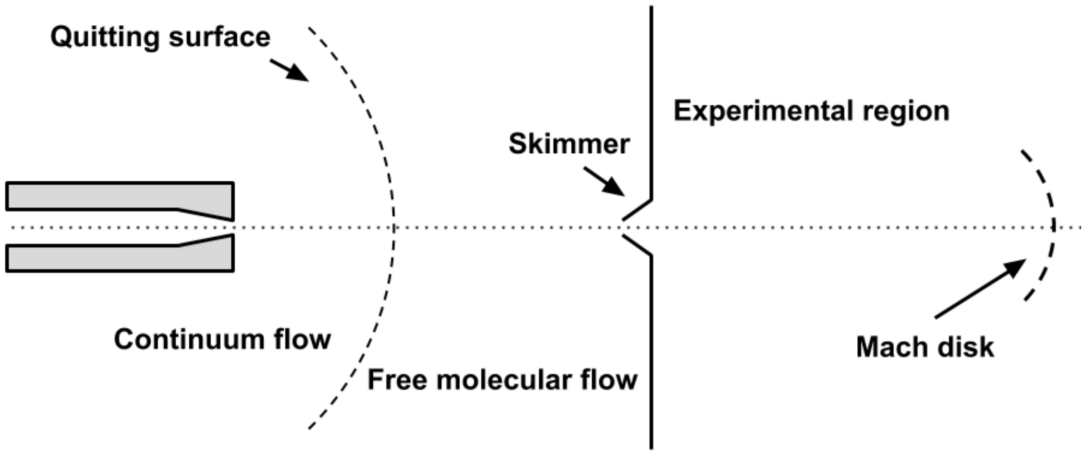

Figure 3.12: A schematic of the free jet expansion with location of the quitting surface. The skimmer should be placed after the quitting surface but before the Mach Disk to allow us to have free flowing and non-interacting molecular beam [12, 15]. Figure taken from [12], under Creative Commons Attribution (CC BY) license.

The location of the quitting surface for diatomic gases is estimated by [12, 15]

$$x_{QS} \approx d\Big(\frac{S_\infty}{3.606}\sqrt{\frac{2}{\gamma}}\Big)^{\frac{1}{\gamma-1}}, \tag{3.30}$$

where S_∞ is the terminal velocity ratio of our gas. It is approximated to 10% by [12, 15]

$$S_\infty = 5.4(P_0 d)^{0.32}. \tag{3.31}$$

In both the equation 3.30 and 3.31, P_0 is in torr and d is in cm.

The existence of shock waves within our apparatus might be worrisome, as they can easily affect the dynamics of our gas. However, the width of the Barrel shock and the Mach disk are given to $\pm 25\%$ respectively by $0.75x_m$, $0.5x_M$ where x_m is the mean free path of the gas and x_M is the location of the Mach Disk [12, 15]. To see why we should not worry about Barrel shocks, let us use our own apparatus. We have a system with $P_b \approx 10^{-6}$ torr and $P_0 \approx 1034$ torr (20 psi absolute). So, the mean free path upstream the Mach disk is about $x_m \approx 10.94$ meters (Calculation can be found in Appendix A). Therefore, if we have a small enough apparatus, there simply is not enough volume for a shock wave, therefore, we have smooth transitions without Barrel shocks [12, 15]. One final point of worry might be the shock waves created by the molecules that bounce off from the skimmer. However, using the same reasoning as above with low gas density and high shock wave thickness we can also ignore the presence of "skimmer shock waves" provided that our experimental setup is compact enough [12, 15]. The actual design parameters can be found in the following chapter when we discuss the construction of the apparatus.

Finally, with the design parameters we have and using [15] we find that at the skimmer we should have a temperature of 2.8 K and 1.24 K in the ionization region. (which are at a distance of 0.052 and 0.142 meters from the valve, respectively.)

Chapter 4

Construction of the Apparatus

4.1 Overview of the Entire Apparatus

We will examine the apparatus in four sections mostly following the path of our gas in the setup: Gas Injection and Skimmer, Ionization and WML Acceleration Stage, and Einzel Lens and Drift Tube/MCP. Finally, we will show our simulations showing that the apparatus should function as intended with time spacing, space/optical focusing in mind. The full apparatus is shown in figure 4.1:

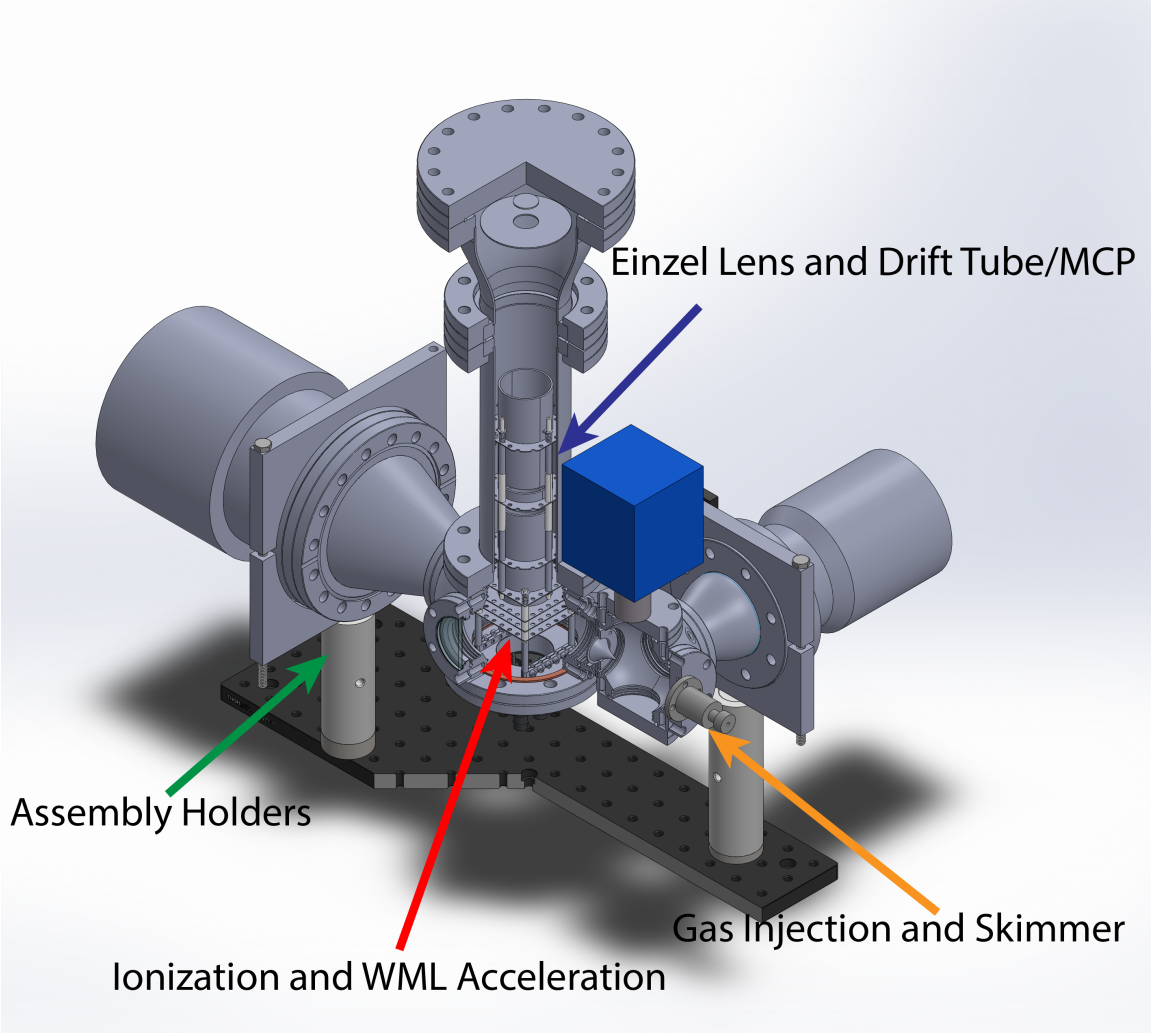

Figure 4.1: CAD drawing of the experimental setup. This is how the assembly looks when all the parts are assembled. Additional detailed sections can be found in the exposition in subsections below. As a scale indicator, the large flange on the top is 6" in diameter.

4.1.1 Gas Injection and Skimmer

Neutral oxygen gas at room temperature is pulsed to the UHV via our pulsed valve. It is a Parker Miniature High Speed High Vacuum Dispense solenoid valve with a 0.02" aperture and conical nozzle. It is mounted on a 2 3/4" CF flange which itself is mounted on a Kimball Physics 2.75" Spherical Cube. For the actual pulsing, a circuit by Ye group at CU Boulder is used [12].

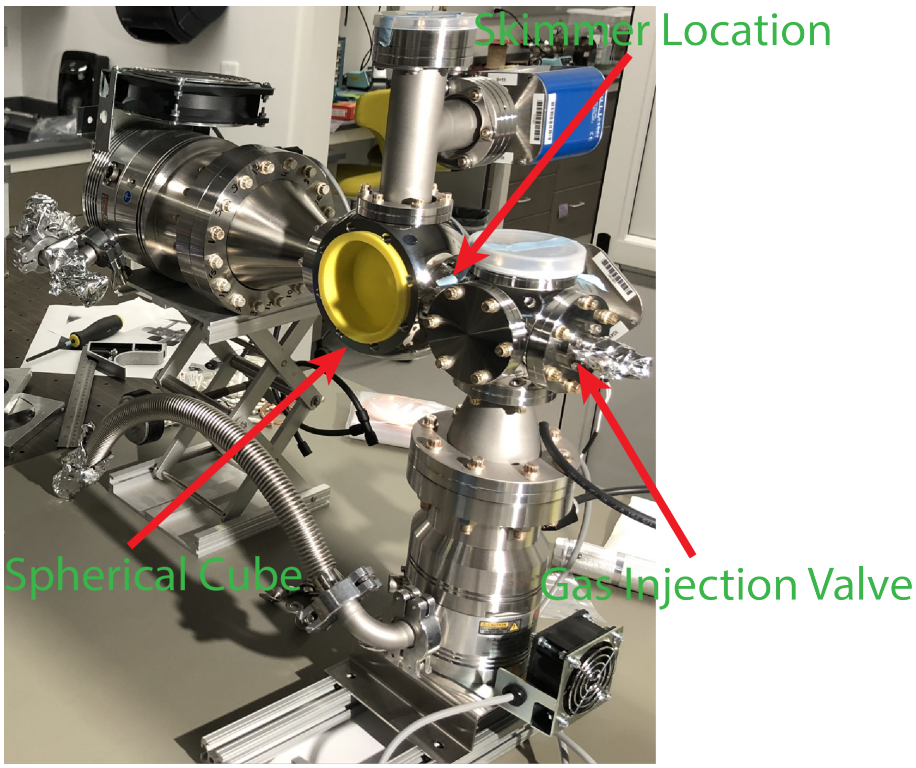

Figure 4.2: Picture of the gas injection and skimmer portion of the apparatus. Spherical cube is used to maximize volume whilst minimizing the surface area of the chamber [36].

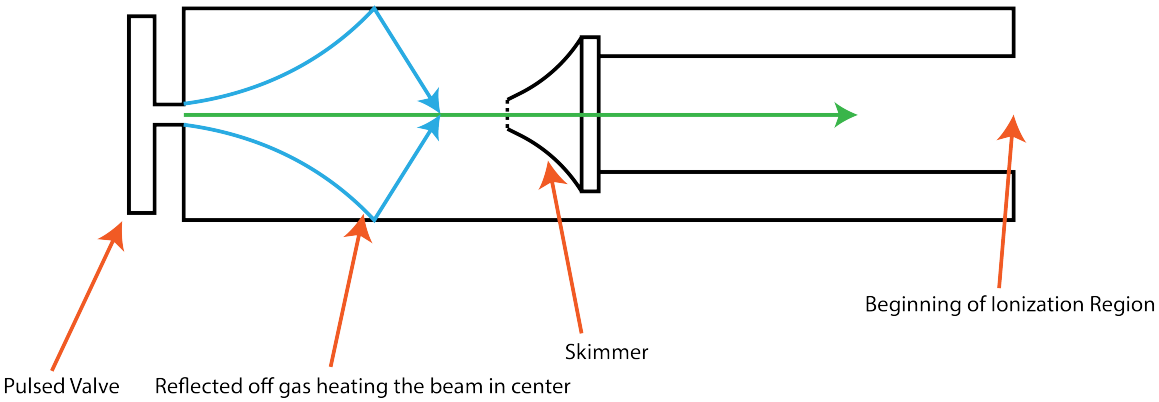

Figure 4.3: Cross-section schematic of the old gas injection and skimmer assembly [12]. The very close presence of the walls to the central line of the gas can lead to the gas bouncing back off the wall and heating the center of the beam [4].

In a previous iteration of the experiment, instead of a spherical cube, we had a 4-way reducing cross with 6.0/2.75" ODs and our pulsed valve was mounted on the 2.75" side. The skimmer was mounted on the 2.75" CF flange on the other side and

stretched out to the side of the pulsed valve [12]. This is illustrated in figure 4.3.

Initially, we were getting ions roughly at room temperature with this setup. Therefore, this caused us to worry about a potential gas reflection interfering with the center of the beam, thereby heating it. To prevent this, we changed to the 2.75" Spherical cube whose walls are much further away from the center of the gas beam [36]. However, this required us to devise a new method to hold the skimmer. We inserted a copper gasket with holes for skimmer placement, and clamped the skimmer on it using screws. The entire skimmer assembly is attached to the seal to the next chamber in place of a gasket. This is illustrated in figure 4.4:

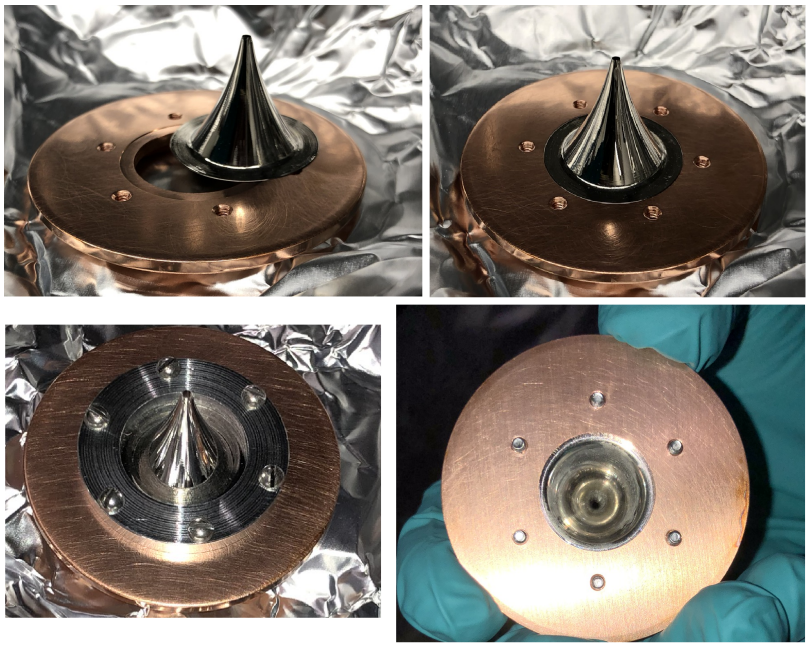

Figure 4.4: Assembly pictures of the new skimmer holder. The placement grooves for the skimmer to slide into can be seen in the top left. Skimmer in place without clamping can be seen in top right. The finished assembly can be seen in bottom left (front face) and bottom right (back face). The depth of the lip in the copper piece is 0.1 millimeters. The diameter of the copper piece is 0.05 meters.

Finally, the overall cross section of this portion of the apparatus can be seen in figure 4.5:

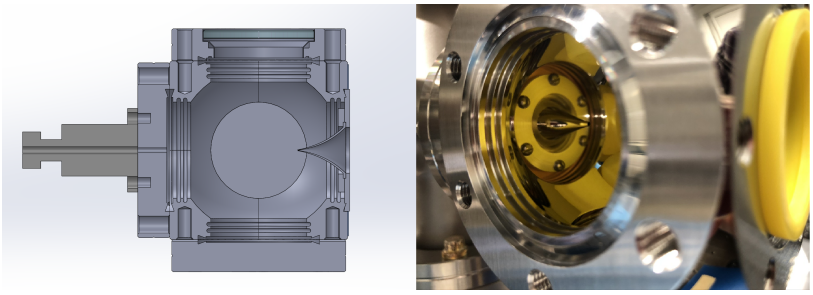

Figure 4.5: CAD model cross section of the gas injection portion of the assembly and a real-life assembly picture. The pulsed valve is assembled at the place of the yellow plastic cover.

4.1.2 Ionization and WML Acceleration Stage

The gas beam enters the main experimental chamber after the skimmer. We used Kimball Physics' 4.50" Spherical Square for the actual chamber. It has 6 CF Flange mounting holes four of which are 2.75" and the other two are 4.50". We already had a HV Electrical Connector from Kurt J Lesker with 2.75" diameter from our previous setup. The electrical feedthroughs are SHV connectors. Hence, we can safely apply up to 5 kV to our electrodes. In this iteration of the experiment, the electrical connections are made through the bottom using an in-vacuum insulated wire with 30 kV rating (Accu-Glass 112716). We have a 4.5" CF mounting hole in the bottom. Therefore, we added a 4.5" to 2.75" zero length reducer from Kurt J Lesker.

The gas beam arrives at the point of ionization–roughly mid distance between the first two plates of WML configuration–with a diameter of ≈ 1.4 mm. The distance between the skimmer and the ionization point is ≈ 142 mm. Furthermore, this is most likely after the Quitting Surface and definitely before the Mach Disk since the Quitting Surface is at a distance between 18 and 2 cm but towards 2 cm. Also, the Mach Disk is at ≈ 294 cm [12]. These estimations can be found in appendix D.

For the parallel plates, we decided to use Kimball Physics' 7x7 C Series Stainless Steel rectangular blank plates for the bottom plate of the WML configuration, and 7x7 C Series Stainless Steel rectangular plate with 1" diameter hole for the middle and top plates. The distance between these plates are determined mainly by our need to have a good uniform electric field and the diameter of the gas beam reaching the middle of the chamber. Therefore, by putting an error margin to our estimations of the gas beam diameter and due to the readily available ceramic spacers' size, we decided to have a space separation of 0.76 cm (0.3 inches). As we will see shortly, we can still find solutions to the time spacing and space focusing equations while setting the plate-to-plate distance to 0.76 cm [16].

The main support structure holding the plates and the einzel lens in place are C series alumina tubings from Kimball Physics eV Parts. These are friction fitted into appropriate sized holes drilled on the 4.5" to 2.5" zero length reducer. We also drilled 4 tapped holes to which we insert additional stainless steel pins that we designed. Then, to hold the entire assembly in place (i.e. to prevent the alumina tubings to slip out of their friction fit), the tubings are clamped to the stainless steel pins using Kimball Physics' evParts Screw Clamp Assemblies size 7.

We used C series alumina and stainless steel spacers to properly position the parts in place. They just slip onto the alumina tubings. After the WML stage, we put four springs (Kimball Physics evParts C Series Compression Springs), one on each tubing, compressed them and put lock rings on top to ensure that the parts are held in place tightly.

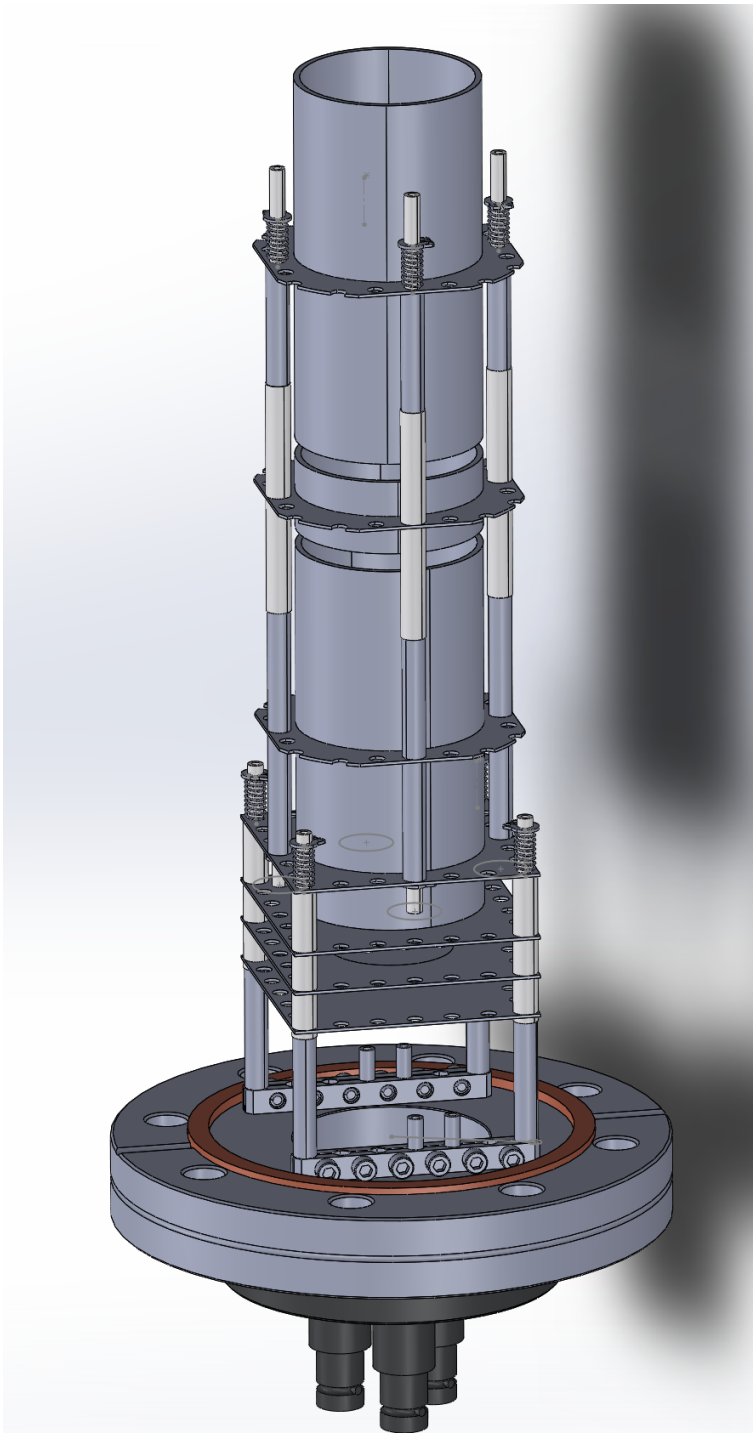

Figure 4.6: CAD Drawing of the electrode assembly. The assembly is held in place using C series alumina tubing, and part positioning is achieved by using alumina and stainless steel C series spacers of various lengths. As a length scale, long Einzel lens electrodes' height is 7.62 cm.

Finding Electrode Voltages

Again, we would like to make the approximation from the Sec. 3.2.2 that $U_0 \approx 0$ J. Therefore, we need to accelerate the ions through a big enough electric field that their initial thermal energies are comparatively small [16]. Our labs previous calculations about the transverse beam speed has the upper bound of ≈ 739 m/s which corresponds to a kinetic energy of $U_0 \approx 0.01$ eV, using the classical equation for kinetic energy [4, 12]. Therefore, if we accelerate the ions through $1 - 2$ kV, we should be able to reasonably apply $U_0 \approx 0$J. Our current electronics can handle up to 2kV, which is why we cannot go above it.

With this approximation and assuming that our parallel plates act as parallel plate capacitors, we have (following from equations 2.6, 2.9 and with the replacement of $s_0 = \frac{s}{2}$) [16]:

$$k_0 = \frac{V_a + V_b}{V_a - V_b}, \tag{4.1}$$

$$D = s k_0^{\frac{3}{2}} \left[1 - \left(\frac{2}{k_0 + \sqrt{k_0}} \right) \right]. \tag{4.2}$$

In our apparatus, we have $D = 33.1$ cm (13.03 inches), which is the distance between the MCP and the last plate of the WML configuration. Solving for k_0 in equation (4.2), we get (with $s = 0.76$ cm) $k_0 \approx 13.422$ which satisfies the maximality condition of equation 2.11. Therefore, using equation (4.1) and setting $V_b = 1500$ V, we get $V_a \approx 1741$ V satisfying our $U_0 \approx 0$J approximation. The final plate in the WML configuration is set to $V_c = 0$ V to have a field free drift tube [16].

4.1.3 Einzel Lens and Drift Tube/MCP

After the ionization and WML region, the ions enter the drift tube from Kurt J Lesker that has a 4.5" diameter . One end of the tube is attached to the ionization

Table 4.1: Dimensions of WML along with Einzel Lens in inches and centimeters.

s(Wiley-McLaren)	0.3 inches	0.76 cm
d(Wiley-McLaren)	0.3 inches	0.76 cm
D(Wiley-McLaren)	13.03 inches	33.1 cm
g(Einzel Lens)	0.15 inches	0.4 cm
D′(Einzel Lens)	1.5 inches	3.8 cm
Einzel Lens Middle Electrode Height	0.6 inches	1.52 cm
Einzel Lens Outer Electrode Height	3.0 inches	7.62 cm

Table 4.2: Recommended voltage setting for the apparatus (pre-experiment), including the back,middle,front plates of Wiley-McLaren configuration and middle, outer electrodes of the Einzel Lens.

Back Plate(Wiley-McLaren)	1741 V
Middle Plate(Wiley-McLaren)	1500 V
Front Plate(Wiley-McLaren)	0 V
Middle Electrode(Einzel Lens)	1040 V
Outer Electrodes(Einzel Lens)	0 V

region and the other end is attached to a 6.00" to 4.5" conical reducer from Kurt J Lesker. Finally, the MCP is attached to the conical reducer, which seals the apparatus. The Einzel lens can be seen in figure 4.6. The main cylindrical electrodes are made using Stainless Steel Cylinders with 1.5" diameter from Kimball Physics. The outer two electrodes measure 7.62 cm (3 inches) in length whilst the inner electrode measures 1.52 cm (0.6 inches).

In order to hold the electrodes in place, we use 3 Kimball Physics C Series 7x7 Rectangular plates with 1.5" diameter cut-out. The electrodes just slide in and then are spot welded to the plates with the help of Kimball Physics' eV Parts Wire Rings. To achieve the correct spacing between the electrodes, we had to spot weld at the correct position. Therefore, we designed and used an alignment jig (see fig. 4.8):

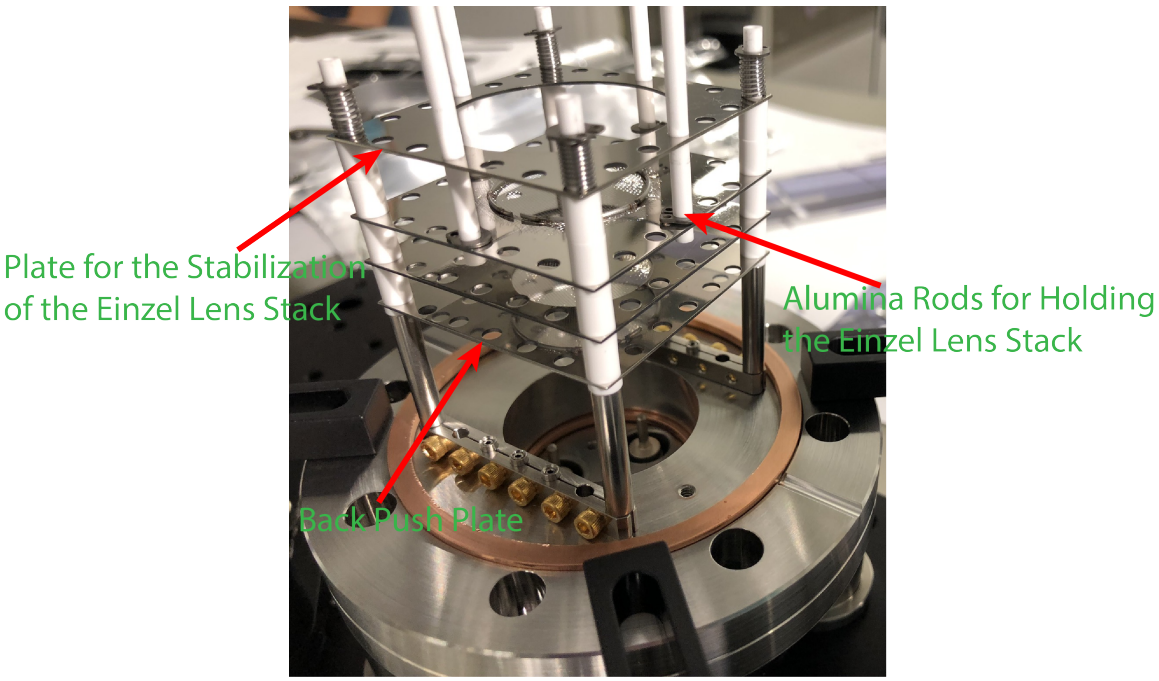

Figure 4.7: Picture of the assembly of the WML Configuration portion of the experimental apparatus, before the attachment of the Einzel lens portion to its top.

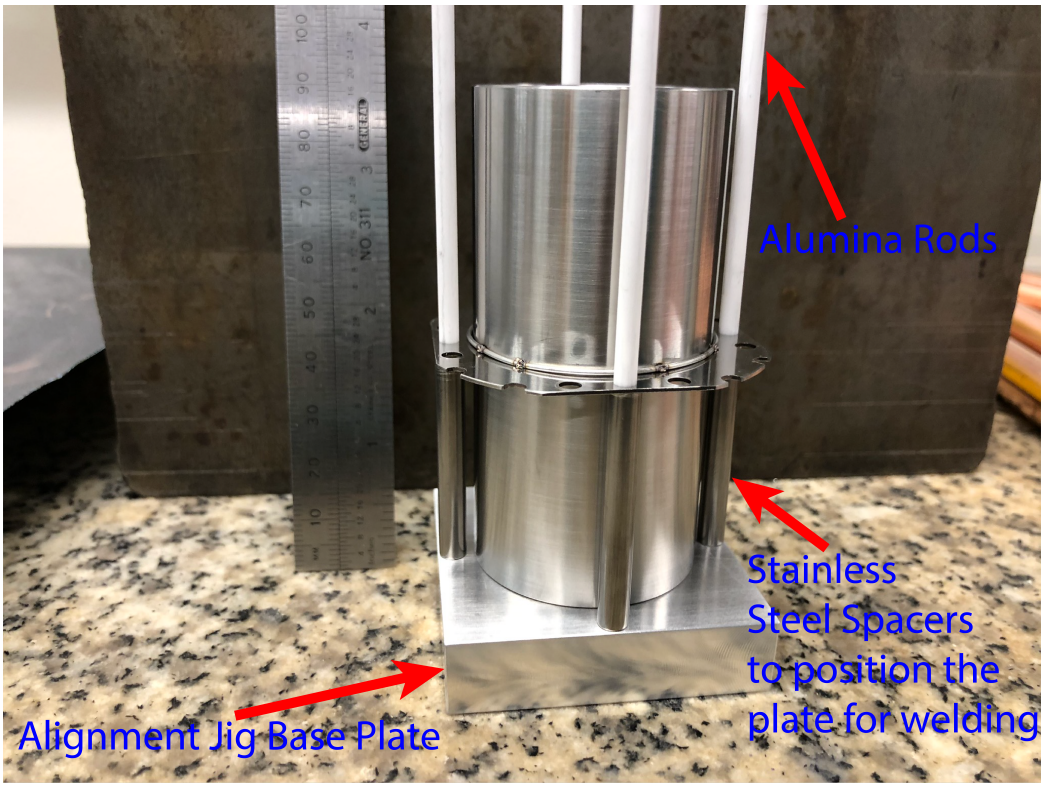

Figure 4.8: Picture of the assembly of the Einzel lens alignment jig with one of the outer Einzel lens electrode inserted into the jig. There are 4 holes in jig's base plate to allow the insertion of four alumina rods.

These plates are given a radius by cutting their corners, to allow them to fit inside the tube that forms the vacuum chamber, which has an inner diameter of $\approx$ 6 cm (2.5 inches) from Kurt J Lesker. Then, we use four C series alumina tubings to hold them in place, as can be seen from figure 4.6. These alumina tubings are attached to another C series 7x7 rectangular plate with 3.8 cm (1.5 inches) cutout. That final plate is attached to the same assembly that holds the WML configuration in place. The distance between the einzel lens electrodes–which is 0.38 cm–is achieved by using Stainless Steel and Alumina C series spacers (from Kimball Physics eV Parts) cut to appropriate lengths. Finally, to make sure that the assembly is held in place tightly, we put another compression spring and lockring after the last einzel lens electrode towards the MCP. We also put a lockring before the bottom einzel lens electrode. These make sure that the alumina tubings do not slide out, and that they hold the lens tightly.

Finding Einzel Lens Dimensions and Electrode Voltages

In order to find the Einzel Lens' dimensions and voltages, we are going to use the parameters already calculated in [35]. We will be constructing our einzel lens with $\frac{g}{D'} = 0.1$ as this is a typical parameter for lenses given by [33–35]. Here, g is the distance between the lens electrodes and D' is the diameter of the electrodes (see fig. 3.1). Therefore, since we have $D' = 3.81$ cm (1.5 inches), our lens separation should be $g = 0.38$ cm (0.15 inches). Now, remember that if our lens is not too strong, we can define a focal length f which satisfies the classical lens equation (2.29) where D_{obj} is the object distance and D_{im} is the image distance [33–35]. In our case, we measure $D_{obj} \approx 10.2$ cm (4 inches) and $D_{im} \approx 24.1$ cm (9.5 inches) where D_{obj} is the distance from the end of WML to the middle of the middle electrode and Q is the distance between MCP and the middle of the middle electrode. Therefore, we need $f \approx 7.2$ cm (2.82 inches). So, we need $\frac{f}{D'} \approx 1.877$. Also, using $\frac{A}{D'} = 0.5$ where A is the distance

between the midpoint of the spaces between outer and inner electrodes, we find that the length of our middle electrode needs to be $D'_{middle} = 1.52$ cm (0.6 inches) [35]. Therefore, looking at the table in [35], we would like $\frac{V_{inner\ electrode}}{V_{outer\ electrode}}$ to be between 5 and 6.

However, remember that we want the outer electrodes to be at ground, to have a field-free drift tube. Therefore, we will estimate first by guessing a suitable middle electrode voltage (i.e. high enough to give the ions an ample "kick" towards the center), which determines the outer electrode voltages. Then, we will shift both voltages until the outer ones' voltages are at ground.

4.2 Simulations of the Apparatus

We used the computer program SimION to simulate the ToF-MS. SimION is a charged particle trajectory simulation program. It works by dividing the given volume of interest into small cubes, and then solves the Laplace's equation iteratively by treating the cubes either as an electrode or as a non-electrode point decided by the user [37]. We will be simulating our setup using cubes of side length 0.5 mm. The data for each cube is stored in RAM during simulation. Therefore, a decrease of 2 in side length causes an increase of 8 fold in RAM usage. It also significantly increases the amount of computations needed to perform the simulation [37]. Therefore, we had to find a side length that optimized simulation time and accuracy.

4.2.1 Time Spacing and Space Focusing Simulations

First, let us simulate the setup only using the WML configuration (i.e. all Einzel lens electrodes are at ground) to see if oxygen molecular ions and oxygen atomic ions are separated in time. Again, the WML electrodes have the following voltage

configuration: back electrode at 1741 V, the middle electrode at 1500 V and the front electrode at 0 V. Fig. 4.9 is a SimION picture of a simulation with 60,000 ions half of which is oxygen molecular ion and the other half is oxygen atomic ion.

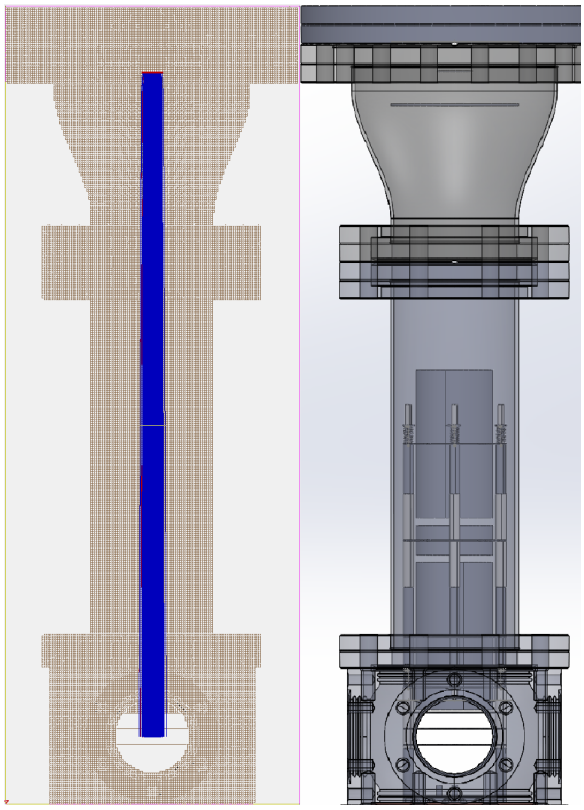

Figure 4.9: Simulation of ion trajectories with Einzel lens electrodes at ground. We see that all the ions hit the MCP (detector). The CAD image is given to the right to show the placement of electrodes and the detector.

In fig. 4.9, the ions are created in the middle of the first two electrodes. Furthermore, they are given the highest standard deviation (in creation position) in the direction that laser comes from and smaller standard deviations in position in the other directions. They are given a velocity of 739 m/s. We first collected data for ions' arrival times to the detector assuming that all ions travel directly to the right of the figure 4.9 at the time of ionization. When we plot the data in a histogram, we get:

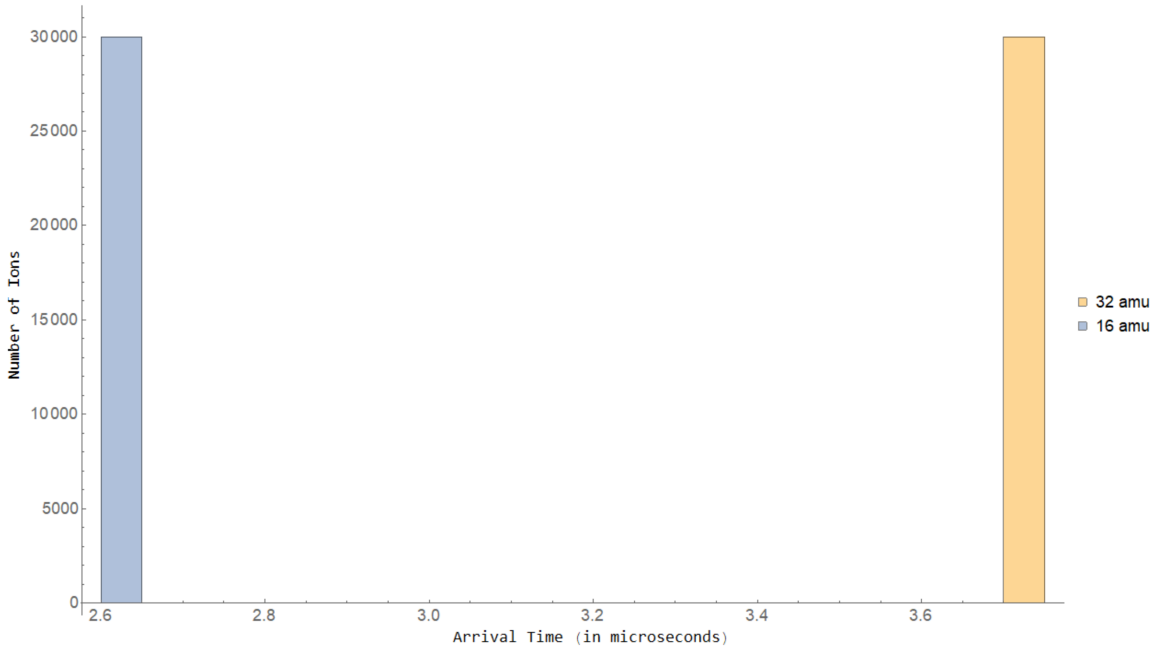

Figure 4.10: Histogram of the arrival times of our ions, using the voltages in table 4.2 with middle Einzel lens electrode grounded. We clearly see that the molecular and atomic ions are very well separated in time.

Notice that this configuration covers the space focusing case since the ions are given a standard deviation about the approximate midpoint of the first two electrodes [16]. Now, for the time spacing portion, let us simulate the worst case where the oxygen molecular ion is moving straight towards the MCP and the oxygen atomic ion is moving straight away from the MCP. The simulation yields the histogram in fig. 4.11:

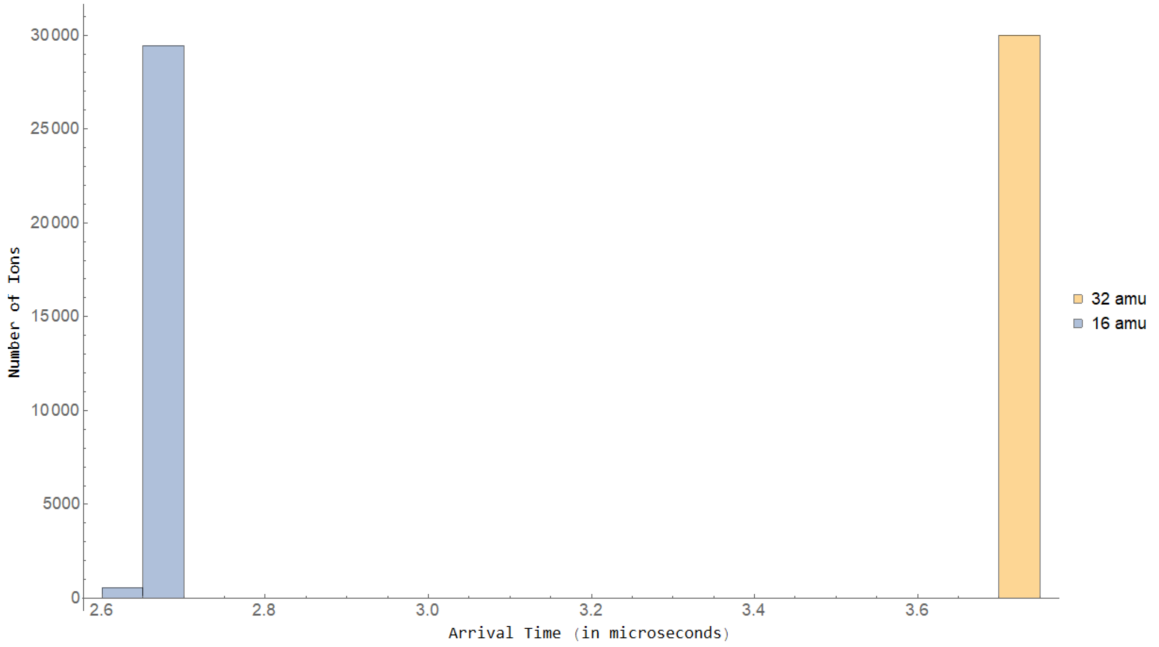

Figure 4.11: Histogram of the arrival times of our ions when the molecular ion moves directly towards the detector and the atomic ion moves directly away from it. We clearly see that the molecular and atomic ions are very well separated in time. The voltages used are given in table 4.2. However, the Einzel lens is grounded for this simulation.

Therefore, time spacing is also achieved, at least in simulation. Finally, we simulate the setup using the Einzel lens to see whether we can focus ions geometrically. We start our estimates by assigning the middle Einzel lens a voltage of $V_{\text{inner electrode}} = 850$ V which is not as strong compared to the acceleration stage, hence our standard lens equation should still apply. Assuming we have $\frac{V_{\text{inner electrode}}}{V_{\text{outer electrode}}} \approx 5.5$, we have $V_{\text{outer electrode}} \approx 155$ V. Shifting both, we get $V_{\text{inner electrode}} = 695$ V and $V_{\text{outer electrode}} = 0$ V. To achieve the maximal focusing, we simulated the setup with many different values for $V_{\text{inner electrode}}$. The most focusing was achieved with $V_{\text{inner electrode}} \approx 1040$ V. Finally, to make sure that the Einzel lens indeed worked as an analogue to a converging lens, we simulated the setup with $V_{\text{inner electrode}} = 1500$ V. The results of these simulations can be seen in figure 4.12:

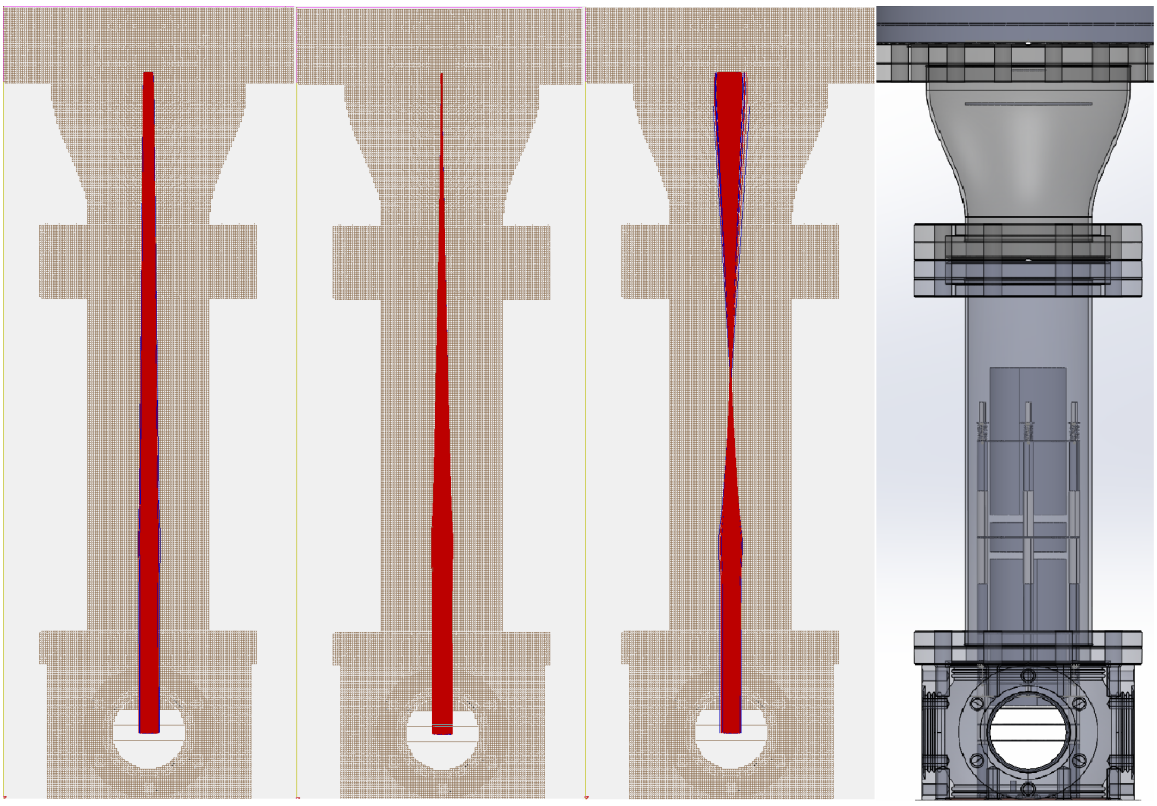

Figure 4.12: SimION simulations of our apparatus with WML electrodes' configuration given in table 4.2. In all three simulations, the outer Einzel lens electrodes are grounded. The inner Einzel lens electrode is at 695 V, 1040 V and 1500 V from left to right, respectively. Indeed, our lens acts as a converging lens in the simulations. These simulations also take into account the Coulomb repulsion effects.

With all the simulations giving positive results, we now proceed to the analysis of our experimental data.

Chapter 5

Apparatus Data and Discussion

Before moving on to using our apparatus in our experiments, we wanted to make sure that it works as expected. Therefore, we conducted a few mini-experiments focusing on one key component of the apparatus in each one: Einzel Lens Optical Focusing of the Ions, Scaling of the Time-of-Flight with Grid Voltage given a constant Grid/Push Voltage Ratio, and Space-Focusing.

5.1 Does the Einzel Lens Focus?

5.1.1 Data and Acquisition Method

Our first task following the assembly of the apparatus was to see whether we could get any ions in the first place. After detecting some ions, we went on to test whether we could get our Einzel Lens to optically-focus our ions. So, we sat at 1744 V for the push plate, 1510 V for the grid plate and we gradually varied the Einzel Lens voltage while firing the laser 250 times at each data point to see how many of the shots had ions. If the Einzel Lens could spatially focus the ions, we expected to see low ion count when the lens is at ground which would increase up to some voltage and decrease after that. The data we obtained demonstrated our point almost perfectly

and is given in fig. 5.1:

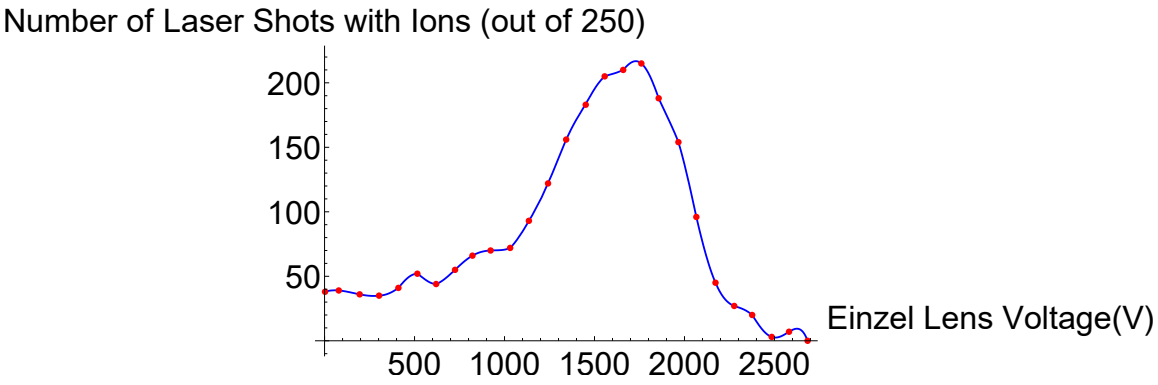

Figure 5.1: Optical Focusing Demonstration Graph of the Einzel Lens with Push Plate at 1744 V calibrated and Grid Plate at 1510 V calibrated. The blue line is the interpolation (4^{th} order) of the data points. At each data point, we fired the laser 250 times and kept track of how many shots had ions detected at the MCP.

5.1.2 Discussion of Einzel Lens Focusing Data

Overall, the data shows that we can focus the ions spatially and the Einzel Lens behaves as expected, at least qualitatively. The main disagreement between our simulations and the experiment was the optimal voltage of the Einzel Lens for maximum focusing. In the simulations, we had an optimal voltage around 1040 V, whilst the data shows an optimality around $1600 - 1700$ V. There may be–at least–three reasons for this. First, we might have underestimated the gas' speed at the point of ionization. If the gas had a higher initial speed, we would need more of a "kick" given by the Einzel Lens to alter the trajectory of the ions. Second, the ions may not be exiting the acceleration region parallel to the MCP-Push Plate axis. More descriptively, the ions may be exiting the acceleration region in a cone whose apex is the point of ionization. So, perhaps, the parallel plate approximation does not hold very well. Since–in our simulations where we determined the optimal Einzel lens voltage–the approximation seemed to hold, it would make sense that the value found in simulations does not agree with experimental results.

Finally, we created the ions–in the simulations–in the middle of the region between the push and grid plates (in all 3 axes), because the middle should be the point where the parallel plate approximation holds the most. We will see in section 5.2.2 that changing the ionization position in the MCP-Push plate axis does not affect our ability to get ions that much. Therefore, we might have created the ions not exactly in the middle of the plane defined by the Push plate which would weaken the parallel plate approximation. In the end, further investigation is needed since we may also have any combination of these three effects or more, such as assembly tolerances. Fortunately, it seems to be working. So, we are going to run at $1600 - 1700$ V rather than track down the discrepancy, for the time being.

5.2 Does the Flight Time Scale as Expected?

5.2.1 TOF vs. Grid Voltage with Constant Voltage Ratio

After finding the optimal voltage for the voltage configuration with 1744 V push plate and 1510 V grid plate, we sat at 1659 V for the Einzel lens. We then varied the grid voltage while keeping grid-to-push-plate voltage ratio the same. We wanted to see whether the time-of-arrival scales as expected by the Wiley-McLaren theory given by eq. 3.5. The main reason to keep the grid-to-push-plate voltage ratio the same is to have a Wiley-McLaren theory *curve*, which will be given by eq. 3.5. Another way to see eq. 3.5 is as a function of $(s, d, D, E_s, E_d, m_{O_2})$ with s, d, D, m_{O_2} being constant. So, if we use random data points without the same ratio (i.e. without writing E_d in terms of a constant multiple of E_s or vice versa), we would have discrete Wiley-McLaren theory *points*–to be precise, we would have a 3D graph–instead of a curve.

Before taking any data, we had to calibrate all the electrical time delays in our experiment to record the actual time-of-flight. The main delay was the time between the triggering of our oscilloscope and the laser actually firing. To measure this delay, we ran a mini-experiment where we clipped the laser on the push electrode without pulsing oxygen. Then, we took data when all the electrodes were on. We saw a big signal in the oscilloscope trace which were hydrogen ions that we ionized with our laser since the plate outgasses hydrogen [4]. Finally, we grounded all of the electrodes and looked whether we had any signal. We expected to still see a big signal in the oscilloscope since the scattered light from the push plate would most likely saturate the MCP. Indeed, we saw a signal at $\approx$ 380 ns which gave our constant time offset for all the data points. The oscilloscope trace for this experiment is given in fig. 5.2:

Figure 5.2: The oscilloscope trace corresponding to our experiment to determine the time interval between the triggering of our oscilloscope and our laser actually firing. The yellow trace shows the MCP signal accumulated from several laser shots. The first distribution is from scattered UV light, which indicates the time the ions would be created. The second distribution is due to actual hydrogen ions ionized due to outgassing of our plate [4].

The results of our experiment after this delay correction are given in fig. 5.3:

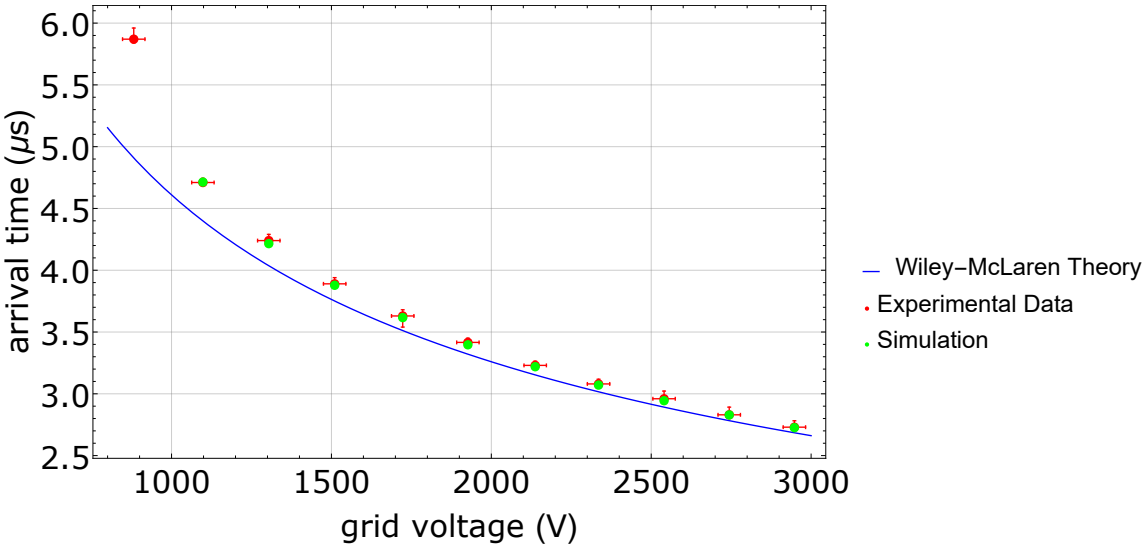

Figure 5.3: Time-of-Flight data's scaling depending on the grid voltage with the same grid/push voltage ratio of ≈ 0.867. The blue curve is the Wiley-McLaren theory of eq. 3.5 without accounting for the Einzel lens' effect on the Time-of-Flight. We have near perfect agreement with the SIMION simulation–green dots on the figure–where the Einzel lens is included in the simulation, except for the first data point. This is expected since the Einzel lens contribution constitutes the largest portion in the overall arrival time for this data-point. So, we do not expect an agreement with the basic Wiley-McLaren theory [4]. Furthermore, the simulation did not even record an ion arriving at the detector for the first data point.

Discussion:

First of all, the uncertainties on the horizontal axis are our estimates on how precise our voltage sources can be. The vertical uncertainties are obtained by looking at the ends of our ion distributions in the oscilloscope traces. Our data did not agree with the Wiley-McLaren theory. However, this is expected due to the Einzel lens [4].

Even though the Einzel lens does not change the overall kinetic energy of the ions before and after passing through the lens, their kinetic energy is still different (i.e. slower) inside the lens [4, 33–35]. Furthermore, in our case, the ions slow down for the first half of their traversal through the Einzel Lens and they get accelerated again

for the second half. Therefore, the ions will take longer to reach the detector when the Einzel Lens is not grounded, compared to when it is grounded [4, 33–35].

To correct for this time difference, we simulated each experiment with Einzel lens on, using SimION. After this, we compared the simulation results with the experimental data, which generally gave good agreement. For instance, one of our simulations for the 1744 V Push plate, 1510 V grid gave a time-of-flight of ≈ 3.74 μs for when Einzel lens was grounded and ≈ 3.90 μs when the Einzel Lens was at 1659 V. This shows that we have to take all the electric fields into consideration. The Wiley-McLaren theory cannot predict the correct result exactly, because it does not know about the existence of other fields in our experiment [4].

After this correction, we had near perfect agreement–with the simulation–for all data points except the very first from left. Our laser UV power was a bit lower for this data point than usual. Furthermore, the arrival time for this point has a very large contribution from the Einzel lens such that we do not really expect the basic Wiley-McLaren theory to match it [4]. Also, if we look at the oscilloscope trace for this data point, we can hardly say that we have a distribution at all. Therefore, we do not think it is a reliable data point.

5.2.2 TOF vs. Vertical Position of Ionization

As a final experiment to run, we decided to measure the time-of-arrival of our ions based on the vertical position of ionization (i.e. We moved the laser up and down in the MCP-Push plate axis). If we had implemented our apparatus correctly, we should have space-focusing. So, our data points for this experiment should agree with the Wiley-McLaren theory–in terms of scaling, since Wiley-McLaren ignores the Einzel lens–given by eq. 3.5. We should also have $k_0 > 3$ as given in eq. 3.11. So, we sat at 1659 V for the Einzel Lens (calibrated), 1744 V for the Push Plate (calibrated)

and 1510 V for the grid (calibrated). After this first experiment, we ran it again with 2019 V for the Push Plate while keeping the grid and Einzel Lens voltage the same, to see if space-focusing gets worse with a non-optimal voltage configuration. Lastly, we changed the push plate voltage to 1611 V (calibrated) and ran the experiment one last time.

These data include calibrations of the actual voltages relative to the dial reading on our voltage supplies (see Appendix E); we also believe we can reproducibly set the voltages to within 1%. The results are given in figs. 5.4, 5.5 and 5.6, respectively.

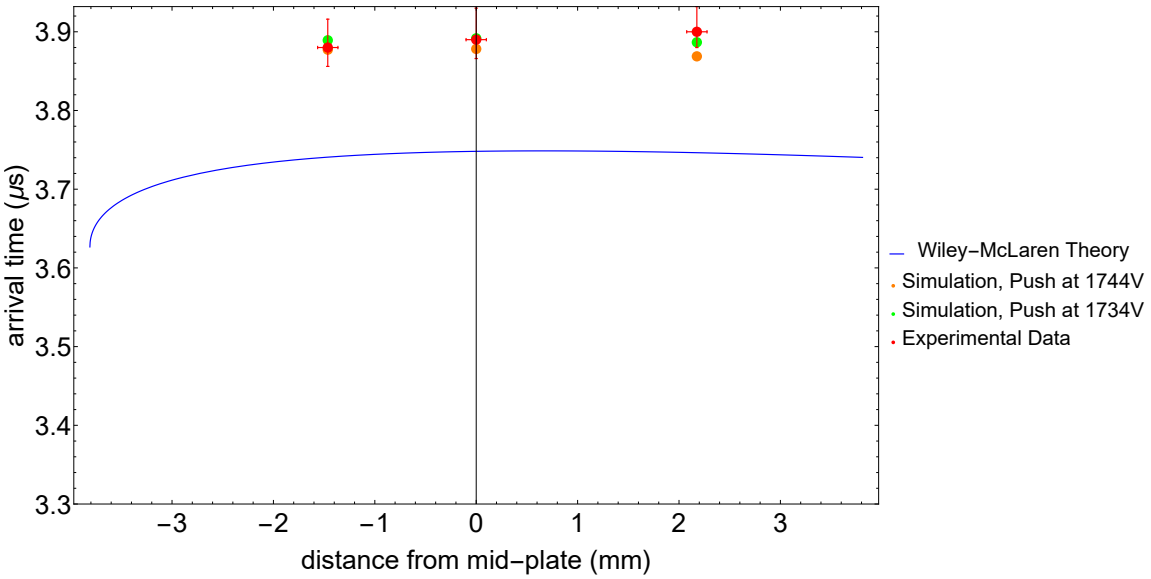

Figure 5.4: Time-of-Flight data's scaling depending on the vertical position of the laser (i.e. in the MCP-Push Plate axis) with push plate at 1744 V and grid at 1510 V. Our data points do not agree with the Wiley-McLaren theory, which does not account for the effect of the Einzel lens. However, we have great agreement with the simulation where the push plate is at 1734 V. Considering that the nominal value on the dial was 1730 V and we did the voltage calibration after the experiment, it seems reasonable that the precision of our voltage source is not infinite ($\approx 1\%$ precision). The Einzel lens is at 1659 V. Positive distances are closer to push plate; negative are closer to grid plate. Zero point is the middle between the two plates.

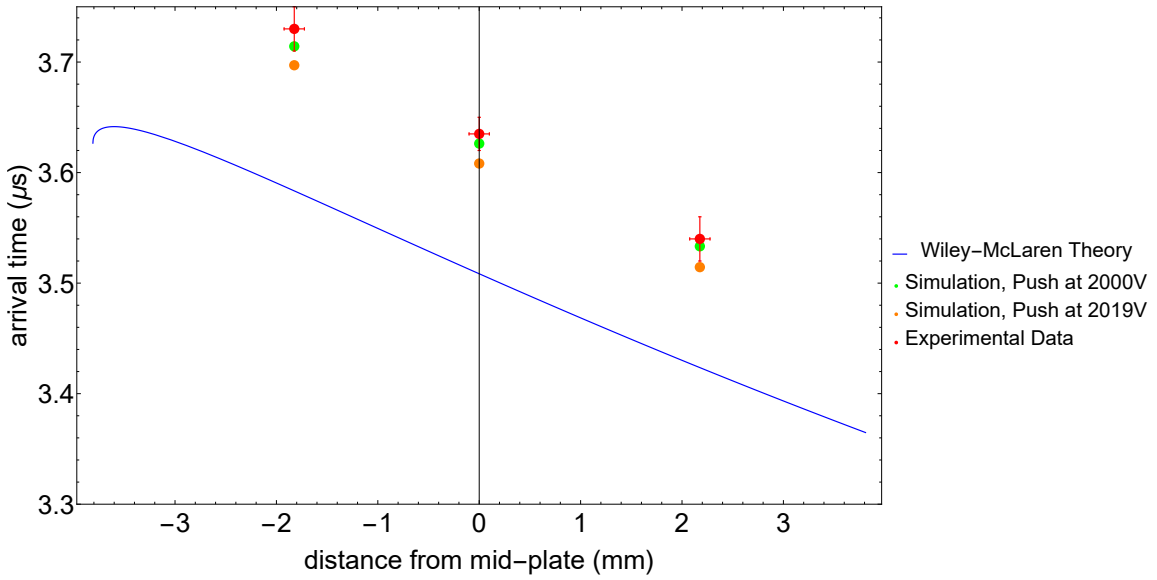

Figure 5.5: Time-of-Flight data's scaling depending on the vertical position of the laser (i.e. in the MCP-Push Plate axis) with push plate at 2019 V and grid at 1510 V. Our data points do not agree with the Wiley-McLaren theory, which does not account for the effect of the Einzel lens. However, we have great agreement with the simulation where the push plate is at 2000 V. Considering that the nominal value on the dial was 2000 V and we did the voltage calibration after the experiment, it seems reasonable that the precision of our voltage source is not infinite ($\approx 1\%$ precision). The Einzel lens is at 1659 V. Positive distances are closer to push plate; negative are closer to grid plate. Zero point is the middle between the two plates.

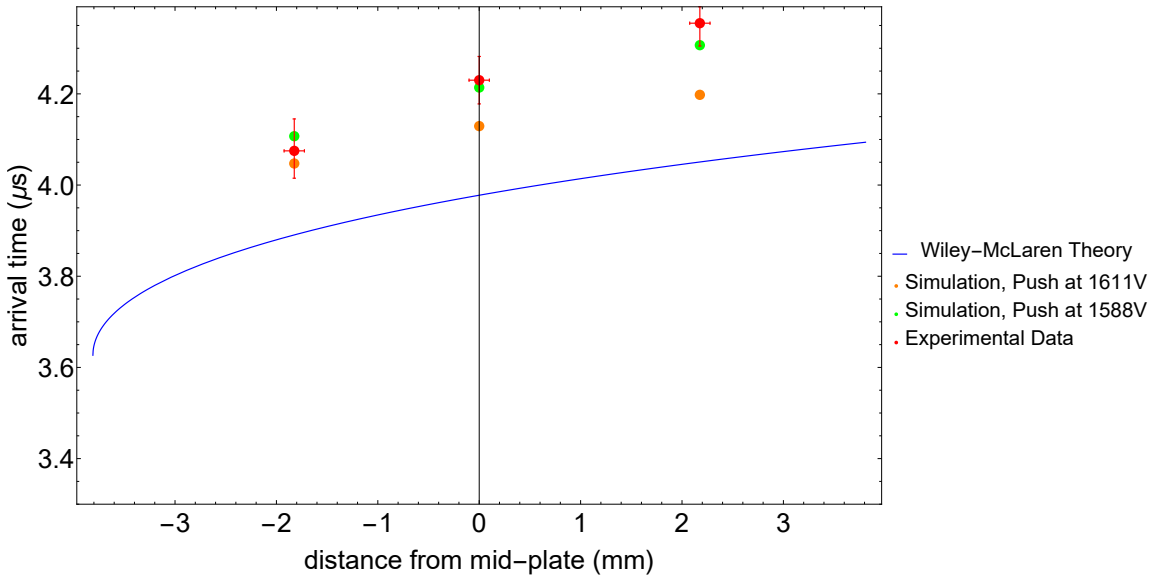

Figure 5.6: Time-of-Flight data's scaling depending on the vertical position of the laser (i.e. in the MCP-Push Plate axis) with push plate at 1611 V and grid at 1510 V. Our data points do not agree with the Wiley-McLaren theory, which does not account for the effect of the Einzel lens. However, we have great agreement with the simulation where the push plate is at 1588 V. Considering that the nominal value on the dial was 1600 V and we did the voltage calibration after the experiment, it seems reasonable that the precision of our voltage source is not infinite ($\approx 1\%$ precision). The Einzel Lens is at 1659 V. Positive distances are closer to push plate; negative are closer to grid plate. Zero point is the middle between the two plates.

Discussion

None of the data points in our experiments in sec. 5.2.2 agree with the Wiley-McLaren theory within the given uncertainties. This is expected since Wiley-McLaren theory does not take the Einzel lens into account. We believe that the reason for these disagreements might be the fact that the Push and Grid voltages were not exactly what we thought they were. We had done the calibration of the electrode voltages after conducting all these experiments. Even though we should be close to the calibration voltages given in table E.1, our voltage sources are not infinitely precise ($\approx 1\%$ precision). For instance, if at the time we did the experiment the push plate were -12 V below the nominal value (1600 V) instead of $+11$ V for the experiment in fig. 5.6, our data would be in agreement with our SimION simulations with Einzel

lens included. For the experiment in fig. 5.4 a similar situation applies, where we would be in agreement with our simulations if we were +4 V above the nominal value (1730 V) of the push plate instead of +14 V. Finally, for the experiment in fig. 5.5 we would be in agreement with our simulations if we were actually right at the nominal value (2000 V) of the push plate instead of our calibration value of 2019 V.

All of these corrections are within 1% of the nominal values of the push plate voltage at the time. Therefore, we think that the actual calibrated voltages at the time of the experiment were indeed different–due to the finite precision ($\approx 1\%$) of our voltage source–than when we made the calibration, resolving the problem. Calibration voltage samples can be found in table E.1.

Comparison

As a last remark before discussing future directions for our experiment, notice that Wiley-McLaren theory curve, SIMION simulations and actual data all show that the vertical position of ionization almost does not matter for the configuration we chose for our experiment (see fig. 5.4). Lastly, we can clearly see that space-focusing gets worse for the other configurations in fig. 5.5 and fig. 5.6, as expected. Therefore, the Wiley-McLaren theory correctly predicts the voltage ratio needed for space-focusing, and we have chosen the correct voltage ratio for our experiment. The time offset from the Einzel lens is a minor issue that needs to be considered to make sense of the absolute arrival times. Fortunately, it does not affect the essential part of the Wiley-McLaren theory for us, the voltage ratio needed for optimal space-focusing [4].

Chapter 6

Future Directions

As we are near the end of the thesis, we should think about how our work will integrate into our short-term goal of measuring the transition frequencies in the $X^2\Pi_g$ state of O_2^+ with greater precision, and into our long-term goal of increasing the precision in the measurement of $\frac{\dot{\mu}}{\mu}$ (the change-in-time of proton-to-electron mass ratio μ). We will first discuss the short-term improvements needed in the apparatus and then the longer-term goals and improvements necessary.

6.1 Short-Term Goals

Our main short-term goal is to measure the transition energies in the $X^2\Pi_g$ state of O_2^+ with better precision than the current values. To achieve this, we have at least five steps we need to take. Our UV power has occasional drops, which will affect our signal-to-noise in the best case and ruin a measurement if the power drops during an experiment, in the worst case. Therefore, *laser power stabilization* is important. Another issue is the duration of the gas pulse. We will not have many ions if we keep the gas pulse very short, which affects our signal-to-noise. If on the other hand, we have a very long gas pulse, then the interactions between particles in the experimental region heat the gas. So, we should find *an optimal gas pulse duration*.

Additionally, we should find an *optimal delay between the firing of the gas and firing of our laser*. If we shoot our laser too early, we miss the gas beam entirely. If on the other hand we fire the laser too late, we either miss the beam and ionize room-temperature background gas or we only catch the "tail" of the gas, which is hotter than its "head". Additionally, in the previous sections we saw that the Einzel Lens' optimal focusing voltage was higher than the one we found in our SimION simulations. We had postulated that an initial speed higher than our estimate might cause this disagreement. Therefore, we should re-estimate the gas speed and find a method to verify it. Furthermore, we should verify that the gas beam intersects the line through the intersection of the two diagonals of our push plate and of our grid plate. If the beam is not passing through that line, then we are not ionizing the gas exactly in the middle of the finite plane defined by the push plate, which worsens our parallel plate approximation. In turn, this might contribute to the discrepancy between the experimental and simulated optimal voltage for the Einzel lens. These works are already underway in the lab.

Finally, we should map out the REMPI spectrum, which we have done recently. Then, before starting our experiment, we choose a peak of this REMPI spectrum (i.e. we choose a rotational state in the neutral molecular Rydberg d state) [4, 11, 12, 14]. One of our REMPI spectra mappings is given in fig. 6.1.

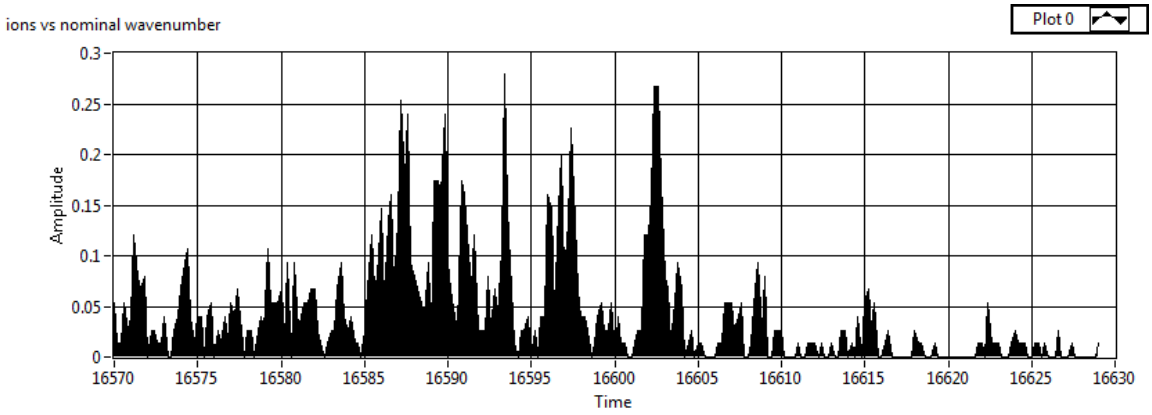

Figure 6.1: One of the latest REMPI spectra of our oxygen gas. We will choose a rotational states in the neutral molecular Rydberg d state by choosing a peak in the REMPI spectrum [11, 12, 14]. We stopped the scan around 16629 cm^{-1} due to power drop-outs of our UV laser.

Our ion count should increase considerably to give us much better signal-to-noise after these improvements [4]. Therefore, for our last short-term improvement, we should *measure some of the transition frequencies* in the $X^2\Pi_g$ state of O_2^+ to see if we can improve their precision. As a first measurement, we will start with $|O_2^+\ X^2\Pi_g, \nu = 0\rangle \rightarrow |O_2^+\ X^2\Pi_g, \nu = 16\rangle$. We can move on to measuring other rovibrational transitions from the electronic ground state if we can successfully measure this transition frequency and improve its precision.

6.2 Longer-Term Goals

The ultimate goal of increasing the precision of $\frac{\dot{\mu}}{\mu}$ is far enough that every estimate we make now will be void due to the emergence of unforeseen experimental/theoretical problems. Generally speaking, we need a trap to trap our ions after creation to have longer probe times. Longer probe times will give us narrower Fourier linewidths, which increase the precision in our measurements [4, 11, 12, 14]. We will also integrate the trap with our ToF-MS since we can use the trap electrodes for ejection too [4, 12, 14]. When we want to eject the ions from the trap, we first turn off the

trap, then very quickly turn on the push/grid electrodes. This sends our ions in a radially outwards trajectory towards the ToF-MS. We can even use the same voltage configuration as is the case in this thesis [11, 12, 14]. Furthermore, we will change from a pulsed two-photon laser to a CW laser, in order to have longer probe times [11, 12, 14]. In the most optimal case, we would like our linewidth to be the same as our probe pulse's Fourier Transform [4, 11, 12, 14].

To specify, here is–roughly–how we will integrate our two setups: the ToF-MS and the Linear Paul Trap (since we need the ToF-MS to measure $\frac{\dot{\mu}}{\mu}$, along with the Linear Paul Trap). The gas pulse valve is in our current experiment, thus, taking the Linear Paul Trap and putting it in our current setup is more feasible than doing the reverse. Furthermore, after optimizing our parameters in our current setup, if we put the ToF-MS in the Linear Paul Trap's vacuum chamber, we will have to do all of them again. This is because the path length of the gas would change. Additionally, the sizes of the flanges in the current Linear Paul Trap setup is different than most of the ones we have in the ToF-MS. The size of the actual Linear Paul Trap is small enough to fit in our ToF-MS setup [38]. So, it is a better choice to change the base of our ToF-MS setup–where we currently have the push and grid plates–to accommodate the Linear Paul Trap.

The support structure for the trap would likely involve either ≈ 4 new support rods or more added length to our existing setup, which will require us to increase the length of our drift tube. Furthermore, this may affect the optimal voltage needed in the Einzel lens for maximal focusing. One additional problem will be the new electrical connections we would need for supplying the potentials to the trap. Currently, all of our high voltage SHV connections are occupied by the ToF-MS electrodes. Therefore, we will have to buy a new high voltage SHV connector from Kurt J. Lesker (with more connections on a single flange). Finally, since the existing ToF-MS setup will

be farther away from the SHV connections than their original positions, we will have to rewire the current electrodes.

For the closing remarks, we should think about the possible impact of our research once completed. Perhaps our new measurement of $\frac{\dot{\mu}}{\mu}$ will be one of the keys to understand physics beyond the Standard Model, and it will open a new door to molecular clocks whose precision outmatches the current standard. On the negative side, we may also only end up tightening the bound on $\frac{\dot{\mu}}{\mu}$, which would mean even more precise methods for measurement might be needed. In that case, perhaps, this new molecular clock may be used in these more precise measurements of $\frac{\dot{\mu}}{\mu}$. Fortunately, tightening the limit can also allow us to discredit certain extensions to the Standard Model and to shrink the parameter space for new physics, which will ease future physicists' trouble for extending our understanding of the Universe [4].

Appendix A

Barrel Shock Width Calculations

Here, we show that the mean free path around the Mach disk is $\lambda_M \approx 10.94$ meters. Since the width of the Barrel Shock is proportional to λ_M, this shows that we will not have any shock waves with a small enough apparatus. All of the equations in this appendix are taken from [12, 15].

A.1 Calculation

In our apparatus, we have $P_0 \approx 1034$ torr (20 psi absolute) and $P_b \approx 10^{-6}$ torr. Remember that the location of the Mach disk is given by:

$$\frac{x_M}{d} \sim 0.67\sqrt{\frac{P_0}{P_b}}. \tag{A.1}$$

We have $d = 0.02$ inches. Therefore, $x_M = 0.67 \times 0.02 \times 0.0254 \times \sqrt{\frac{1034}{10^{-6}}} \approx 10.944$ meters. Since we have O_2, our gamma (assuming it is constant through the relevant range) is $\gamma = \frac{7}{5} = 1.40$. Now, the Mach number at position x is given by:

$$A(\frac{x - x_0}{d})^{\gamma-1} - \frac{\frac{1}{2}(\frac{\gamma+1}{\gamma-1})}{A(\frac{x-x_0}{d})^{\gamma-1}}. \tag{A.2}$$

In our case, we have $\frac{x_0}{d} = 0.40$. Therefore, we have $x_0 = 0.40 \times 0.02 \times 0.0254 \approx 0.0002$ meters. So, our Mach number at the Mach disk location is $M(x_M) \approx 3.65(\frac{10.944-0.0002}{0.02\times0.0254})^{\frac{2}{5}} - \frac{3}{3.65\times3.65(\frac{10.944-0.0002}{0.02\times0.0254})}^{\frac{2}{5}} \approx 197.510$. Additionally, remember that we have:

$$\Big(\frac{T}{T_0}\Big) = \frac{1}{1 + \frac{\gamma-1}{2}M^2}. \tag{A.3}$$

Therefore, at the location of Mach disk, we have: $(\frac{T}{T_0})_M \approx (1 + \frac{(197.510)^2}{5})^{-1} \approx 0.000128$. Remembering the equality of:

$$\Big(\frac{n}{n_0}\Big) = \Big(\frac{T}{T_0}\Big)^{\frac{1}{\gamma-1}}, \tag{A.4}$$

we have $(\frac{n}{n_0})_M \approx (0.000128)^{\frac{5}{2}} \approx 1.859\times10^{-10}$. Using the standard equation $P = nRT$ (with P_0,n_0,T_0) with $T_0 \approx 300$ K, we find $n_0 \approx 3.329 \times 10^{25}\ m^{-3}$. The source mean free path is given by:

$$\lambda_0 \sim \Big[5.3 n_0 \Big(\frac{C_6}{kT_0}\Big)^{\frac{1}{3}}\Big]^{-1}, \tag{A.5}$$

with $\frac{C_6}{k} = 8.31 \times 10^{-55}$ K.m^6 for O_2. Therefore, the source mean free path is $\lambda_0 \sim \frac{1}{5.3\times3.329\times10^{25}\Big(\frac{8.31\times10^{-55}}{300}\Big)^{\frac{1}{3}}} \approx 4.035 \times 10^{-8}$ meters. Finally, the Mach disk mean free path is given by:

$$\lambda_M = \lambda_0 \Big(\frac{n_0}{n}\Big)_M \sqrt[3]{\Big(\frac{T}{T_0}\Big)_M}. \tag{A.6}$$

So, we have $\lambda_M \approx 4.035 \times 10^{-8} \times (1.859 \times 10^{-10})^{-1} \times \sqrt[3]{0.000128} \approx 10.9$ meters. Consequently, since the Barrel Shock wave width is proportional to λ_M, our apparatus with a length scale on the order of 1 meter cannot contain any barrel shock waves [12, 15].

Appendix B

Values of Molecular Constants Used For Spectroscopic Data

All of the spectroscopic constants used in the table B.1 are taken from [29–31]. The T_ν in levels $\nu = 0, 1$ are translated (by 97441 cm^{-1} given in [31]) so that the transition wavelengths are referenced with respect to the ground vibrational state of O_2^+. Constants for $\nu = 0, 1$ are from [29, 31], $\nu = 2 - 12$ are from [30] and $\nu = 13 - 38$ are from [31].

Unless otherwise mentioned, all of the units in table B.1 are cm^{-1}.

ν	T_ν	A_ν	B_ν	D_ν	H_ν	p_ν	q_ν	D_{A_ν}
0	0	200.289	1.67996	5.22E-6	-	0.0153	0.00023	-
1	1884	199.700	1.66072	5.36E-6	-	0.0153	-3E-5	-
2	4662.33	199.0191	1.641295	5.41E-6	-	0.01756	0.000382	-
3	6469.7027	198.3736	1.622004	5.604E-6	-	0.01754	0.000214	-5.3E-5
4	8244.5209	197.6496	1.602269	5.495E-6	-	0.01724	0.000161	-2.06E-5
5	9986.7681	196.9182	1.582689	5.541E-6	-	0.01658	0.000101	-6.42E-5
6	11696.2739	196.1548	1.562978	5.5628E-6	-	0.01651	6.9E-5	-9.56E-5
7	13373.3399	195.3294	1.5431883	5.6296E-6	-	0.017186	0.0001295	-0.0001077
8	15017.8424	194.4656	1.5232907	5.6768E-6	5.5E-12	0.017028	0.0001196	-0.0001149
9	16629.7677	193.5646	1.5033193	5.7455E-6	1.11E-11	0.017053	0.0001325	-0.0001472
10	18209.0913	192.6152	1.4832262	5.8032E-6	1.141E-11	0.016968	0.0001264	-0.0001791
11	19755.7614	191.6055	1.463001	5.8588E-6	1.09E-11	0.016942	0.0001248	-0.0002049
12	21269.7034	190.5455	1.442621	5.8915E-6	-	0.01704	0.0001217	-0.0002408
13	21810	189.4	1.42	-	-	-	-	-
14	23258	188	1.4	-	-	-	-	-
15	24673	187	1.38	-	-	-	-	-
16	26056	185	1.36	-	-	-	-	-
17	27403	183.5	1.34	-	-	-	-	-
18	28715	183	1.32	-	-	-	-	-
19	29997	179.3	1.3	-	-	-	-	-
20	31245	182	1.28	-	-	-	-	-
21	32461	177	1.25	-	-	-	-	-
22	33634	174	1.25	-	-	-	-	-
23	34777	173	1.22	-	-	-	-	-
24	35885	169	1.19	-	-	-	-	-
25	36959	168	1.17	-	-	-	-	-
26	37995	165	1.17	-	-	-	-	-
27	38999	163	1.15	-	-	-	-	-
28	39964	161	1.13	-	-	-	-	-
29	40909	159	1.11	-	-	-	-	-
30	41815	155	1.1	-	-	-	-	-
31	42677	155	1.07	-	-	-	-	-
32	43505	150	1.04	-	-	-	-	-
33	44315	147	1.02	-	-	-	-	-
34	45055	146	1	-	-	-	-	-
35	45779	144	1.01	-	-	-	-	-
36	46480	141	0.98	-	-	-	-	-
37	47150	142	1	-	-	-	-	-
38	47779	141	0.95	-	-	-	-	-

Table B.1: Constants used by PGOPHER to calculate the transition wavelengths. Notice that not all of these constants are used for every level. The ones used for a given vibrational level depend on which ones the authors provided [29–31]. The ones not available are notated with "-."

Appendix C

Current Best Spectroscopic Estimates For Rovibrational Transitions in $X^2\Pi_g$ state of O_2^+

$J_{initial}$	$\Omega_{initial}$	J_{final}	Ω_{final}	ΔE (cm^{-1})	$\delta_{\Delta E}$ (cm^{-1})
0.5	0.5	1.5	1.5	25860.9927	$\approx 5-6$
0.5	0.5	1.5	1.5	26057.9921	$\approx 5-6$
0.5	0.5	0.5	0.5	26063.0125	$\approx 5-6$
0.5	0.5	2.5	0.5	26049.7036	$\approx 5-6$
0.5	0.5	2.5	0.5	25852.5217	$\approx 5-6$
1.5	1.5	0.5	0.5	26067.0621	$\approx 5-6$
1.5	1.5	0.5	0.5	26249.4029	$\approx 5-6$
1.5	1.5	1.5	1.5	26062.0417	$\approx 5-6$
1.5	1.5	1.5	1.5	25865.0423	$\approx 5-6$
1.5	1.5	1.5	1.5	26244.3825	$\approx 5-6$
1.5	1.5	1.5	1.5	26047.3831	$\approx 5-6$

1.5	1.5	2.5	0.5	26053.7532	$\approx 5-6$
1.5	1.5	2.5	0.5	25856.5713	$\approx 5-6$
1.5	1.5	2.5	0.5	26236.094	$\approx 5-6$
1.5	1.5	2.5	0.5	26038.9121	$\approx 5-6$
1.5	1.5	3.5	1.5	26042.0397	$\approx 5-6$
1.5	1.5	3.5	1.5	25844.7121	$\approx 5-6$
1.5	1.5	3.5	1.5	26224.3805	$\approx 5-6$
1.5	1.5	3.5	1.5	26027.0529	$\approx 5-6$
2.5	0.5	0.5	0.5	26073.8114	$\approx 5-6$
2.5	0.5	0.5	0.5	26256.2536	$\approx 5-6$
2.5	0.5	1.5	1.5	26068.791	$\approx 5-6$
2.5	0.5	1.5	1.5	25871.7916	$\approx 5-6$
2.5	0.5	1.5	1.5	26251.2332	$\approx 5-6$
2.5	0.5	1.5	1.5	26054.2338	$\approx 5-6$
2.5	0.5	2.5	0.5	26060.5025	$\approx 5-6$
2.5	0.5	2.5	0.5	25863.3206	$\approx 5-6$
2.5	0.5	2.5	0.5	26242.9447	$\approx 5-6$
2.5	0.5	2.5	0.5	26045.7628	$\approx 5-6$
2.5	0.5	3.5	1.5	26048.789	$\approx 5-6$
2.5	0.5	3.5	1.5	25851.4614	$\approx 5-6$
2.5	0.5	3.5	1.5	26231.2312	$\approx 5-6$
2.5	0.5	3.5	1.5	26033.9036	$\approx 5-6$
2.5	0.5	4.5	0.5	26033.8704	$\approx 5-6$
2.5	0.5	4.5	0.5	25836.2155	$\approx 5-6$
2.5	0.5	4.5	0.5	26216.3126	$\approx 5-6$
2.5	0.5	4.5	0.5	26018.6577	$\approx 5-6$

3.5	1.5	1.5	1.5	26078.24	$\approx 5-6$
3.5	1.5	1.5	1.5	25881.2406	$\approx 5-6$
3.5	1.5	1.5	1.5	26260.8242	$\approx 5-6$
3.5	1.5	1.5	1.5	26063.8248	$\approx 5-6$
3.5	1.5	2.5	0.5	26069.9515	$\approx 5-6$
3.5	1.5	2.5	0.5	25872.7696	$\approx 5-6$
3.5	1.5	2.5	0.5	26252.5357	$\approx 5-6$
3.5	1.5	2.5	0.5	26055.3538	$\approx 5-6$
3.5	1.5	3.5	1.5	26058.238	$\approx 5-6$
3.5	1.5	3.5	1.5	25860.9104	$\approx 5-6$
3.5	1.5	3.5	1.5	26240.8222	$\approx 5-6$
3.5	1.5	3.5	1.5	26043.4946	$\approx 5-6$
3.5	1.5	4.5	0.5	26043.3194	$\approx 5-6$
3.5	1.5	4.5	0.5	25845.6645	$\approx 5-6$
3.5	1.5	4.5	0.5	26225.9036	$\approx 5-6$
3.5	1.5	4.5	0.5	26028.2487	$\approx 5-6$
3.5	1.5	5.5	1.5	26024.9146	$\approx 5-6$
3.5	1.5	5.5	1.5	25827.0307	$\approx 5-6$
3.5	1.5	5.5	1.5	26207.4988	$\approx 5-6$
3.5	1.5	5.5	1.5	26009.6149	$\approx 5-6$

Table C.1: Best current estimates for rovibrational transition energies of our clock transition $|X^2\Pi_g\ \mathrm{O}_2^+, \nu = 0\rangle \rightarrow |X^2\Pi_g\ \mathrm{O}_2^+, \nu = 16\rangle$. In this table, we limited the initial $\mathrm{J}_{\mathrm{initial}}$ to be between $\frac{1}{2}$ and $\frac{7}{2}$, inclusive. The uncertainties are estimated using T_ν [11, 17–20, 29–31]. We have the same uncertainty in all of these data since the uncertainty is correlated in the sense that the relative positions are very precise. It is simply an overall offset that is not well known [11, 12, 14, 29–31]. The units of ΔE and $\delta_{\Delta E}$ are cm^{-1}. The other constants are unitless. These calculations are done using PGOPHER with constants reported in Appendix B [17–20, 29–31].

Appendix D

Gas Beam Diameter, Quitting Surface and Mach Disk Estimations

In the previous iteration of the experiment, we had treated the gas source as a point source expanding in a conical fashion with the edges determined by the skimmer to estimate the diameter of the gas beam. Then, using similar triangles we had estimated the beam diameter to be $\approx$ 1mm. We had measured this by shining a light through valve hole and using a ruler roughly in the middle of the chamber. The results were in agreement with our estimations. So, we used the same method for beam size estimation in this iteration. Illustration of the calculation is given in fig. D.1:

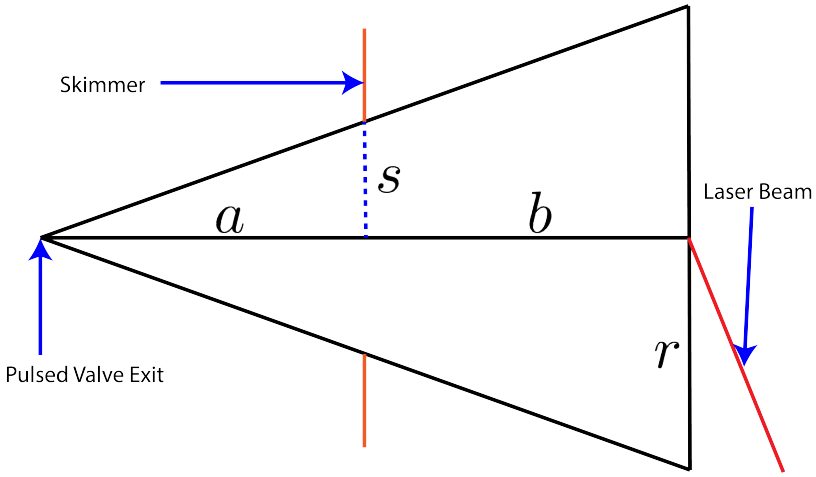

Figure D.1: Schematic of the method to estimate the beam diameter at the center of the chamber. Beam diameter is $2r$ where $r = \frac{s}{a}(a+b)$

In our case, we have $a = 51.816$ mm (2.04 inches), $b = 90.424$ mm (3.56 inches) and $s = 0.254$ mm (0.01 inches). Therefore, we estimate the beam diameter to be $2r = \frac{0.01 \times 5.6 \times 2}{2.04}$ inches ≈ 1.4 mm.

Before we talk about the main support structure, we should check that $a+b$ is indeed between the Quitting Surface and the Mach Disk. First, our pressure levels inside the chamber are on the order of $P_b \sim 10^{-5}$ torr and lower. With a very low assumption of $P_0 = 1$ bar≈ 750 torr, we have $x_M = 0.67 \times d \times \sqrt{75 \times 10^6} \approx 5802 \times d \times 2.54 \approx 116 \times 2.54 = 294.6$ cm (116 inches) with $d = 0.5$ mm (0.02 inches). Therefore, we are definitely ionizing before the Mach Disk. As for the quitting surface, it is between 18 cm and 2 cm, but towards the 2 cm range. Therefore, most likely, the position of ionization is after the Quitting Surface [12].

Appendix E

Nominal and Calibrated Voltages of our Electrodes

Push Plate Voltage (Nominal)	Push Plate Voltage (C)	Grid Plate Voltage (Nominal)	Grid Plate Voltage (C)	Einzel Lens Voltage (Nominal)	Einzel Lens Voltage (C)
1040	1025	700	673	0	2.7
1270	1271	900	881	400	410
1500	1510	1100	1098	600	619
1600	1611	1300	1304	800	821
1730	1744	1500	1510	1000	1031
1960	1979	1700	1722	1200	1241
2190	2222	1900	1926	1400	1451
2420	2458	2100	2137	1600	1659
2650	2689	2300	2335	1800	1856
2880	2916	2500	2540	2000	2065
3110	3149	2700	2743	2200	2276
3340	3383	2900	2947	2400	2484

Table E.1: Nominal and Calibrated Voltage samples of our electrodes. Nominal voltages are based on the dials of our voltage source, whilst calibrated voltages are based on our multimeter measurements. "(C)" denotes calibrated voltages. The voltages that we did not take an exact data for are approximated with a basic proportionality calculation with the closest available data point.

Bibliography

[1] N. Markosian, "Time (Stanford Encyclopedia of Philosophy)," (2002), URL https://plato.stanford.edu/entries/time/.

[2] C. Rovelli, "The Physics and Philosophy of Time," (2018), URL https://www.youtube.com/watch?v=-6rWqJhDv7M.

[3] K. Higgins, D. Miner, C. N. Smith, and D. B. Sullivan, "A Walk Through Time (version 1.2.1)," (2004), URL http://physics.nist.gov/time.

[4] D. A. Hanneke, Private communication.

[5] A. Jaffe, "The Illusion of Time," Nature **556**, 304 (2018), URL https://www.nature.com/articles/d41586-018-04558-7.

[6] J. Allnutt, D. Anand, D. Arnold, A. Goldstein, Y.-S. Li-Baboud, A. Martin, C. Nguyen, R. Noseworthy, R. Subramaniam, and M. Weiss, "Timing Challenges in the Smart Grid," (2017), URL https://nvlpubs.nist.gov/nistpubs/SpecialPublications/NIST.SP.1500-08.pdf.

[7] T. Mai, "Global Positioning System History," (2011), URL https://www.nasa.gov/directorates/heo/scan/communications/policy/GPS_History.html.

[8] R. W. Pogge, "GPS and Relativity," (2017), URL http://www.astronomy.ohio-state.edu/~pogge/Ast162/Unit5/gps.html.

[9] J. Nelson, "What Is an Atomic Clock?" (2019), URL https://www.nasa.gov/feature/jpl/what-is-an-atomic-clock.

[10] M. Safronova, D. Budker, D. DeMille, D. F. J. Kimball, A. Derevianko, and C. W. Clark, "Search for New Physics with Atoms and Molecules," Reviews of Modern Physics **90** (2018).

[11] R. Carollo, A. Frenett, and D. Hanneke, "Two-Photon Vibrational Transitions in $^{16}O_2^+$ as Probes of Variation of the Proton-to-Electron Mass Ratio," Atoms **7**, 1 (2018).

[12] A. Frenett, *State-Selective Production of Oxygen Molecular Ions for New Physics Searches*, Undergraduate thesis, Amherst College (2018), URL https://dhanneke.people.amherst.edu/reprints/theses/frenettThesis2018.pdf.

[13] G. Herzberg, *Molecular Spectra and Molecular Structure* (Van Nostrand, 1950).

[14] J. K. Pfatteicher, *Developing Rapid Quenching Electronics for Coupling an Ion Trap to a Mass Spectrometer*, Undergraduate thesis, Amherst College (2019), URL https://dhanneke.people.amherst.edu/reprints/theses/pfatteicherThesis2019.pdf.

[15] G. Scoles, D. Bassi, U. Buck, D. Laine, and U. Valbusa, *Atomic and Molecular Beam Methods* (Oxford University Press, 1992).

[16] W. C. Wiley and I. H. McLaren, "Time-of-Flight Mass Spectrometer with Improved Resolution," Review of Scientific Instruments **26**, 1150 (1955).

[17] "PGOPHER," URL http://pgopher.chm.bris.ac.uk/index.html.

[18] C. M. Western and B. E. Billinghurst, "Automatic Assignment and Fitting of Spectra with PGOPHER," Physical Chemistry Chemical Physics **19**, 10222 (2017).

[19] C. M. Western, "PGOPHER: A Program for Simulating Rotational, Vibrational and Electronic Spectra," Journal of Quantitative Spectroscopy and Radiative Transfer **186**, 221 (2017).

[20] C. M. Western and B. E. Billinghurst, "Automatic and Semi-Automatic Assignment and Fitting of Spectra with PGOPHER," Physical Chemistry Chemical Physics **21**, 13986 (2019).

[21] W. Demtröder, *Atoms, Molecules and Photons An Introduction to Atomic-, Molecular- and Quantum Physics* (Berlin, Heidelberg Springer Berlin Heidelberg, 2018).

[22] R. Shankar, *Principles of Quantum Mechanics* (Springer, 2014).

[23] J. M. Brown and A. Carrington, *Rotational Spectroscopy of Diatomic Molecules* (Cambridge Cambridge Univ. Press, 2003).

[24] S. Winitzki, "Perturbation Theory for Anharmonic Oscillations Lecture Notes by Sergei Winitzki," (2006), URL `https://www.physik.uni-muenchen.de/lehre/vorlesungen/sose_11/T1_Theoretische_Mechanik/vorlesung/anharmonic-perturbation.pdf`.

[25] N. Yamanaka, "Calculations of Specific Mass Shifts in Be II ($1s^2 2s^2 S, 1s^2 2p^2 P$)," Physics Letters A **243**, 132 (1998).

[26] N. Yamanaka, "Calculation of Mass Polarization for the ($1s^2 2s^2 S$) and ($1s^2 2p^2 P$) States in Li-like Ions," Journal of Physics B: Atomic, Molecular and Optical Physics **32**, 1597 (1999).

[27] N. Yamanaka, "Mass Polarization Effect in He-like Ions," Journal of Physics B: Atomic, Molecular and Optical Physics **34**, 4271 (2001).

[28] F. Tran, A. Khoo, R. Laskowski, and P. Blaha, "Nuclear Hyperfine Interactions," (2018), URL https://www.bc.edu/content/dam/bc1/schools/mcas/physics/pdf/wien2k/Hyperfine_NMR.pdf.

[29] J. Coxon and M. Haley, "Rotational Analysis of the $A^2\Pi_u \rightarrow X^2\Pi_g$ Second Negative Band System of $^{16}O_2^+$," Journal of Molecular Spectroscopy **108**, 119 (1984).

[30] B. C. V. V. Prasad, D. Lacombe, K. Walker, W. Kong, P. Bernath, and J. Hepburn, "Fourier Transform Emission Spectroscopy of the Second Negative ($A^2\Pi_u$ - $X^2\Pi_g$) System of the O_2^+ Ion," Molecular Physics **91**, 1059 (1997).

[31] Y. Song, M. Evans, C. Y. Ng, C.-W. Hsu, and G. K. Jarvis, "Rotationally Resolved Pulsed Field Ionization Photoelectron Bands of O_2^+ ($X^2\Pi_{(1/2,3/2)g}$, v+=0-38) in the Energy Range of 12.05-18.15 eV," The Journal of Chemical Physics **111**, 1905 (1999).

[32] F. Wolf, J. C. Heip, M. J. Zawierucha, C. Shi, S. Ospelkaus, and P. O. Schmidt, "Prospect for Precision Quantum Logic Spectroscopy of Vibrational Overtone Transitions in Molecular Oxygen Ions," arXiv:2002.05584 [physics, physics:quant-ph] (2020), URL https://arxiv.org/abs/2002.05584.

[33] J. H. Moore, C. C. Davis, and M. A. Coplan, *Building Scientific Apparatus : A Practical Guide to Design and Construction* (Cambridge University Press, 2009).

[34] F. H. Read, A. Adams, and J. R. Soto-Montiel, "Electrostatic Cylinder Lenses I: Two Element Lenses," Journal of Physics E: Scientific Instruments **4**, 625 (1971).

[35] A. Adams and F. H. Read, "Electrostatic Cylinder Lenses II: Three Element Einzel Lenses," Journal of Physics E: Scientific Instruments **5**, 150 (1972).

[36] P. Jansen, D. W. Chandler, and K. E. Strecker, "A Compact Molecular Beam Machine," Review of Scientific Instruments **80**, 083105 (2009).

[37] D. J. Manura and D. A. Dahl, *SIMION 8.0/8.1 User Manual Covering SIMION Version 8.1.0.31* (Bechtel, Idaho Scientific Instrument Services, Inc. On Behalf Of Idaho National Labs, 2011).

[38] S. Qiao, *Constructing a Linear Paul Trap System for Measuring Time-Variation of the Electron-Proton Mass Ratio*, Undergraduate thesis, Amherst College (2013), URL `https://dhanneke.people.amherst.edu/reprints/theses/qiaoThesis2013.pdf`.